Extending the Leverage of Air-Bridge Thermophotovoltaic Architecture: Design, Modeling, and Experimental Demonstration

by

Jihun Lim

A dissertation submitted in partial fulfillment
of the requirements for the degree of
Doctor of Philosophy
(Electrical and Computer Engineering)
in the University of Michigan
2023

Doctoral Committee:

Professor Stephen R. Forrest, Chair
Professor Elaheh Ahmadi
Professor Zetian Mi
Professor Pramod Sangi Reddy

Jihun Lim

jihunlim@umich.edu

ORCID iD: 0000-0003-4074-9617

Compared to the age of the universe,

even if life is shorter than a fleeting moment,

there is no reason not to enjoy it.

Acknowledgements

This short and long journey started the 1st of February 2016. Till present, I always have thanked many people and their supports. Without your encouragement and support, the journey would have been more tough and severe. I would like to take this opportunity to say thank you.

First, I would like to convey my sincere and indescribable gratitude to my advisor, Professor Stephen Forrest. I joined the OCM (Optoelectronic Components and Materials) group in the fall of 2019 and consider the time a watershed moment in my life. The environment of every weekly group meeting reflects his color, his affection for students, and his passion for scientific research. He never loses a moment, not even one second, during the whole three hours. Students are initially put under a lot of pressure. As time goes by, you will someday find that you are enjoying the time. His untouchable insight, vast and deep knowledge in various fields, and steadfast passion for the academic world always motivated me. Every group meeting was an unpriced experience that guided me to becoming a professional researcher. I truly assure you that his distinct leadership has trained, is training, and will train people who will be qualified engineers around the world. I have to especially appreciate his patient, warm, and sincere advice on my life, which is more valuable than anything I learned in textbooks or classes. I am sorry that I have not grown enough by fully accepting his advice due to my infinitely lacking self. I appreciate your sincere care for your group and students.

The second is to all the group members. Yongxi Li, Bin Liu, Hafiz Sheriff, Jeffrey Horowitz, Byungjun Lee, Jong Chan Kim, Claire Arneson, Sritoma Paul, Xinjing Huang, Haonan Zhao, Boning Qu, Rebecca Lentz, Kan Ding, and our valuable guard, Eva Ruff. Our office (2222 EECS) doesn't have windows, so I didn't like the space at first. After some time passed, I found that I used to come to the office when I felt anxious about my future. Why? Because there are my friends. Early bird Hafiz, marathoner Claire, hard worker Jeff, very highly motivated person Sritoma, a rising star for OPV modules Xinjing, and non-stop and optics expert Haonan. Thanks to your presence, I was truly happy in our office. The two very kind and warm guys, Yongxi and Bin, thank you, and I respect your passion for research. Without Eva, our group will have unimaginable troubles every day. I sincerely appreciate your kind, attentive, and correct guidance on the administration and logistics.

I greatly appreciate all my collaborators and colleagues. Byungjun and Dejiu were former students in our group, who greatly trained me for thermophotovoltaic fabrications and MBE operations. Especially, Byungjun spent countless time to share his experience for the fabrications and MBE operations. Without his efforts, I must have had more frustrating times.

I thank my collaborators, Bosun Roy-Layinde, Tobias Burger, and Professor Andrej Lenert. The group has been collaborating with me and our research group. During the collaborations, I was truly happy to see insight and receive good advice and encouragement.

I appreciate Professor Pramod Sangi Reddy. During the project for near-field radiative heat transfer, it was my honor that I could attend every meeting with you. One lesson I learned from him is that he has never been late for appointments including the date for my thesis proposal. This is one of the biggest lessons I learned during the period. I realized that keeping promises is the beginning and end of everything. Thank you very much for the valuable lesson.

The University of Michigan supports graduate students in many different aspects. I appreciate all the support from Rackham Graduate School, the College of Engineering, and the Electrical & Computer Engineering Department. Especially, I appreciate Kristen Thornton, Graduate Coordinator, and Professor Heath Hofmann.

I would like to acknowledge many of the LNF staffs for being great help including Brian, Pilar, Dennis, Sandrine, Matt, Shawn, Kevin, Vishva, Casey, Katharine, etc.

I have to express my gratitude to the Korean friends I met in Ann Arbor. Yongbum Park, Eun Sung Moon, Seung Jong Lee, Myung Jin Shin, Won Cheol Lee, Kyu min Kwon, Byungjun Lee, Sung Woon Jang, Sung Yul Choo, Ji Hwan Seol, Hee Woo Kim, Jong Chan Kim, Jae Yoong Cho, Ji Seok Kim. Myung Jin, Won Cheol, and Sung Woon, I will not forget the long time we spent in the Duderstadt library. Yongbum Park, my dear friend. Thank you so much for becoming my good friend.

I always have been missing my friends in Korea. Hyun Jae Na, Kang Min Lee, Hyung Jun Kim, Eung Joo Kang, Jun Mo Yang, and Kyung Ahn Kwon. I always recall your encouragement when I am tired and in a trouble. I love you all guys.

My best friend, Ki bum Kook You have been my best friend since my teens. You are really a good-natured person, which has been training my personality during the long and long time. Always stay healthy until I return to Korea to enjoy our life together.

Sang Yeon Choi, my dear friend, I can’t forget your welcome to me when I visited Korea in August 2021. I will shadow your warm and kind personality every time.

Dr. Joon Seok Park and Dr. Jun Hyung Lim wrote recommendation letters for my doctoral application. I met them when I was at Samsung. I always appreciate all of your kindness and sincere advice. Without your support, it is not an exaggeration to say I couldn’t get started on this

journey. All of my memories with you and our team members encouraged me when I was having a hard time. At this opportunity, I'd like to sincerely thank you for all your support and mentoring.

I have to appreciate my Korean advisors, Professor Dae-Shik Seo, Professor Seoweon Heo, and Professor Hyun-Jae Kim. In 2016, I appreciated your welcome and encouragement for my decision to take a doctoral course. Particularly, I remember Prof. Heo's encouragement, "Good luck!".

I thank all my family members for their endless love and support. After my baby was born, I could see the power of love from my parents and parents-in-law. My young brother, Ji Hyuk Lim, you have done your responsibility very well so far. Always be brave, and I believe you will always find your way toward your dream. My sister, Ji Young Lim, I really miss you, your husband, and my nephews. I especially respect your husband, who is the bravest and most great man. Waiting for someday when we can come together and enjoy a party will be the source that infuses me with new hope. My sister-in-law and her husband, thank you for your support, apple-watch, and Nike clothes. I'm looking forward to the day we drink overnight. My parents and in-law, your infinite love for me have had me alive and energetic.

Tae Hee Lim. Thank you for your birth and becoming my daughter. I'm your father and, in front of you, I am the bravest man on the planet. Let's learn and enjoy our lives together.

The 1st of February 2016 is the start date for preparing the application for this doctoral course. From the day to present, my wife has supported me. This thesis is for my wife. Thank you for your long-time patience. Until Taehee becomes a teenager, a twenty-something, a wife for someone, and a mother for her baby, we will occasionally have difficult times. Let's get through those times well. But let's not miss other little happy moments. Then I think it will be a happy enough life for us. Thank you, and I love my wife, Jiin Kim.

Lastly, I'd like to say that I was happy during the journey because I could learn one lesson, which is that finding something hidden beyond a textbook is truly enjoyable. "Fear is nothing when confronted. The wind is not to be calculated but to be overcome.", a monologue in the movie titled "War of the Arrows".

Table of Contents

List of Tables

List of Figures

Abstract

Diversifying renewable energy sources is important for reducing greenhouse gas emissions, promoting energy security, and economic development. Thermophotovoltaics (TPV) are promising for energy harvesting using electromagnetic radiation to generate electricity via the photovoltaic effect. Photon recycling enabled by spectrally selective TPV cells, in particular, has sparked intense research interest in the pursuit of high-efficiency TPV systems. An air-bridge (AB) TPV architecture can optimize out-of-band (OOB) photon recycling by suppressing Fresnel reflections at the interface between air and semiconductors. However, a thin-film TPV membrane spanning Au gridlines that forms the air bridge is vulnerable to being buckled and cracked due to the small tolerances to strain (less than 1–2 %) before fracture. Such structural failures limit the application of the AB-TPV architectures for energy conversion applications. This thesis focuses on overcoming the challenges and exploring the use of thin-film TPV architectures in many applications.

We study the controllable buckling of free-standing thin-film semiconductor metamaterials using a thin-walled structure spanning Au grid supports. The buckling is developed by application of axial forces to the semiconductor membranes during cold-weld bonding to the substrate. We analyze the degree of membrane distortion using Euler's buckling theory. Finite element analysis (FEA) quantitatively predicts the shape and magnitude of the film deflection. This leads to a method for controlling and even eliminating the buckled morphology.

Next, we design of a 3.4-μm-thick InGaAs/InP photodiode structure for an undistorted AB-TPV cell. For a high-efficiency TPV system, we consider three factors: quantum efficiency (QE), a non-buckled morphology, and high reflectance, R_{OOB}, for OOB radiation from a blackbody source. The photodiode comprises a 2 μm thick n-type InP buffer layer with a Hall mobility > 3000 cm^2/Vs. Technology-aided computer design (TCAD) calculates an internal quantum efficiency (IQE) of 97 % for the InGaAs photodiode. FEA shows the strain of the 3.4-μm-thick TPV membrane is less than 0.001%, resulting in the buckling height of only a few nanometers. Transfer matrix methods (TMM) calculates R_{OOB} of nearly 98 %.

Using the photodiode structure, we demonstrate InGaAs AB-TPV cells grown by molecular beam epitaxy. The enhanced mechanical stability results in high yield of non-buckled TPV membranes. The OOB reflectance is measured using Fourier transform infrared (FTIR) spectroscopy, resulting in R_{OOB} = 97.6 %, which is a significant improvement over a Au-BSR InGaAs TPV showing R_{OOB} = 91.2 %. Measurements via surface profilometry and a 3D laser confocal microscope confirm that the AB-TPV membrane has negligible deflection. The power conversion efficiency (PCE) of the TPV cell was 30.2 % (fill-factor, *FF*, 72.4 % and open-circuit voltage, V_{oc}, 0.45V) at a temperature of 1352 K.

A tandem TPV structure can exceed the PCE of a single-junction TPV cell. A conventional tandem configuration requires lattice-matched epilayer growth and heavily doped ($>10^{19}/cm^3$) tunnel-junctions (TJs). The epitaxial growth restricts available materials of various bandgaps, and TJs cause a large parasitic loss of R_{OOB} due to free carrier absorption (FCA). We demonstrate a multi-air-bridge tandem TPV architecture by combining independently grown and fabricated InGaAs subcells cold-welded into a single stack. The architecture has two different air-cavity layers, totally eliminating the need for lossy TJs. The InGaAs homo-tandem and single-junction

TPV cells have V_{oc} = 0.78 V and 0.42 V, respectively. FTIR measurements show the R_{OOB} = 96.3 %, where the loss by FCA is 1.8 %. This architecture offers the possibility of combining arbitrary materials into a variety of tandem configurations.

Finally, we study the PCE limit for InGaAs AB-TPV cells. Using Drude theory, we reveal that the spectral loss due to FCA causes the reduction of R_{OOB} < 1%, such that it does not significantly affect the PCE. The experimental IQE is 98%, implying that the short-circuit current density (J_{sc}) is close to the design limit. The loss of V_{oc} shows a difference of 0.15V compared to the V_{oc} from radiative limited performance, where the charge loss in the depletion region decreases the V_{oc} and *FF*. The design limit assumes no charge loss due to recombination, resulting in a decrease in V_{oc} below the radiative limit of 0.02 V and a high *FF* of around 80%. With the assumption that the spectral loss caused by metal shadowing results in the drop in spectral efficiency (SE) of < 1 %, the InGaAs TPV structure has an optimized PCE with a gridline spacing of approximately 50 μm.

These studies present comprehensive strategies for the diverse applications of AB-TPV architectures. Understanding the mechanism of thin-film membrane buckling suggests a solution for extending AB-TPV architecture for renewable and sustainable energy harvesting. The demonstrations of InGaAs thin-film AB-TPV devices overcome persistent challenges such as low yield and difficulty of fabrication. The multi-air-bridge tandem structure provides an innovative solution to realize unlimited bandgap partners and optimize photon recycling with air bridges. Identifying the factors limiting the TPV performance helps to forecast the possible PCE limit for AB-TPV cells. Finally, this work opens up the possibility for realizing high-efficiency thin-film AB-TPV architectures.

Chapter 1 Introduction

Heat exchange between two blackbodies (a radiator and a photodiode) enables electricity generation via the photovoltaic (PV) effect, known as thermophotovoltaic (TPV) systems [1-3]. The Stefan-Boltzmann law defines the blackbody radiation power as a function of temperature (blackbody radiant emittance = σT^4, σ: the Stefan-Boltzmann constant, T: temperature), resulting in a TPV system with a low energy conversion efficiency. Therefore, it can limit the various applications of TPV systems for energy harvesting. Spectrally selective methods have dramatically improved TPV efficiency [2,4-6]. In particular, employing a back-surface reflector (BSR) with a TPV cell allows selective absorption of photons with higher energy than the bandgap of the absorber in the PV, where the BSR reflects the photons at out-of-band (OOB) wavelengths [1-3]. Based on the configuration of the TPV system with a relatively high view factor (VF, the ratio of overlap of the emitter and detector areas), the BSR TPV architecture enables the preservation of OOB photons by reflecting them back to the source, contributing to a high energy conversion efficiency. Gold is an available photon reflector but has a parasitic loss by Fresnel reflection and surface-plasmon-polariton (SPP) modes, which limit the maximum reflectance to 96% [2,7,8]. The cavity interference (Fabry-Perot oscillations) causes an additional 1% drop in the OOB reflectance (R_{OOB}) [9,10]. The recent introduction of an air-bridge (AB) embedded TPV architecture alleviates the losses caused by Fresnel reflection and SPP [1], resulting in an enhanced power conversion efficiency (PCE) about 33% compared to an Au-BSR InGaAs TPV. Accordingly, the AB-TPV architecture is expected to enhance the ability of sub-bandgap photon harvesting, thereby

increasing TPV efficiency. The technology can be applied to a wide range of applications, such as other low bandgap materials, near-field radiative heat transfer, and tandem TPVs.

1.1 Background of Photovoltaic Markets and Its Effect on Thermophotovoltaic Generators

Global warming causes unwanted changes to the Earth including unpredictable weather patterns, an increase in average temperature, and deforestation [11,12]. Many researchers have come up with various technical means to replace fossil fuels with renewable sources such as hydroelectric energy [13,14], biofuels [15-17], wind energy [18-21], and others [22-24]. Solar PV devices are a promising method to generate electricity using sunlight [25-35]. The PV market has been fast-growing in energy production industries. The cumulative installed solar PV energy capacity is more than 500 gigawatts [36,37]. Unfortunately, some factors restrain the capacity to approximately a few percent of the world's total electricity [38-40]. For instance, the size of a PV panel is dependent on available space. Second, high-rate energy production requires sunny weather to work best. Although advanced solar PV technologies – for example, multi-junction PVs and transparent/cost-effective organic-PVs (OPVs) [29,30,41-43] – have been introduced, they are still limited by the aforementioned factors.

Recent progress in infrared-based energy conversion has attracted researchers, providing alternatives to generating electricity [44-47]. Among these, TPV devices using infrared energy have the advantage of light source versatility and less reliance on space than solar systems [1,5,48-51]. A TPV system can generate electricity using heat from infrared radiation, as shown in Fig. 1.1 (a). It has merits such as solar-independent operation, high power density, no bounds on daytime and location, and low maintenance cost. Therefore, the TPV energy system can be applied to harvesting energy from renewable power systems, furnaces, and industrial waste heat. Figure

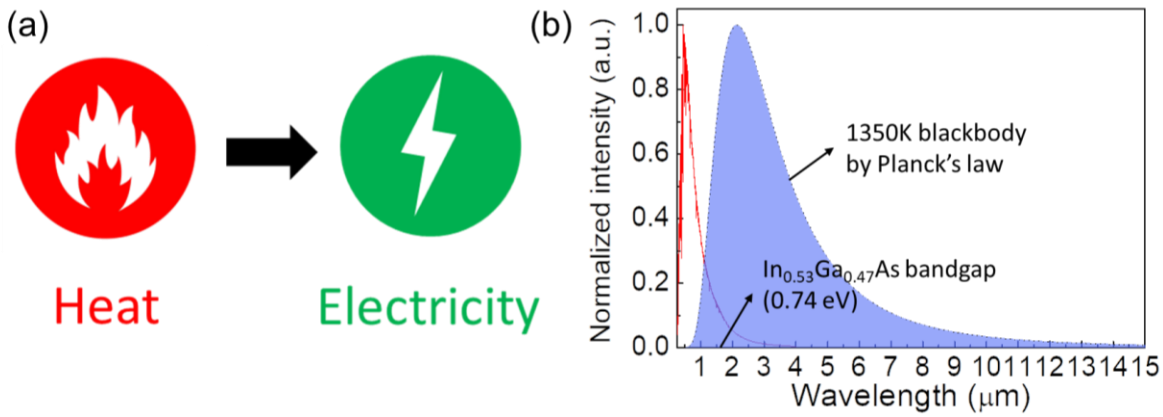

Figure 1.1 (a) Symbolic expression of energy conversion of heat to electricity. (b) Comparison of solar (red-line) and blackbody (1350K) spectrum.

1.1(b) compares the solar and blackbody (1350K) spectrum, showing that most emitted photons are in the infrared wavelength range. The blackbody in the far-field follows Planck's law as [52]:

$$B(\lambda,T)=\frac{2hc^2}{\lambda^5}\cdot\frac{1}{e^{hc/\lambda kT}-1} \tag{1.1}$$

where h is the Planck's constant, c is the velocity of light, λ is the wavelength, k is the Boltzmann constant, and T is the blackbody temperature. The energy conversion efficiency is determined by the output electrical power (P_{out}) of a PV module and spectral light management. Therefore, low bandgap materials are favorable for the high P_{out} in infrared-based energy conversion technologies. III-V compound semiconductors such as InGaAs and InSb are such as low bandgap materials that absorb the infrared.

1.2 Power Conversion Efficiency in a Thermophotovoltaic System

A TPV system comprises three main components: a heat emitter, a cooling system, and a PV cell, as illustrated in Fig. 1.2(a). Unlike a solar system, the TPV system has a relative high VF

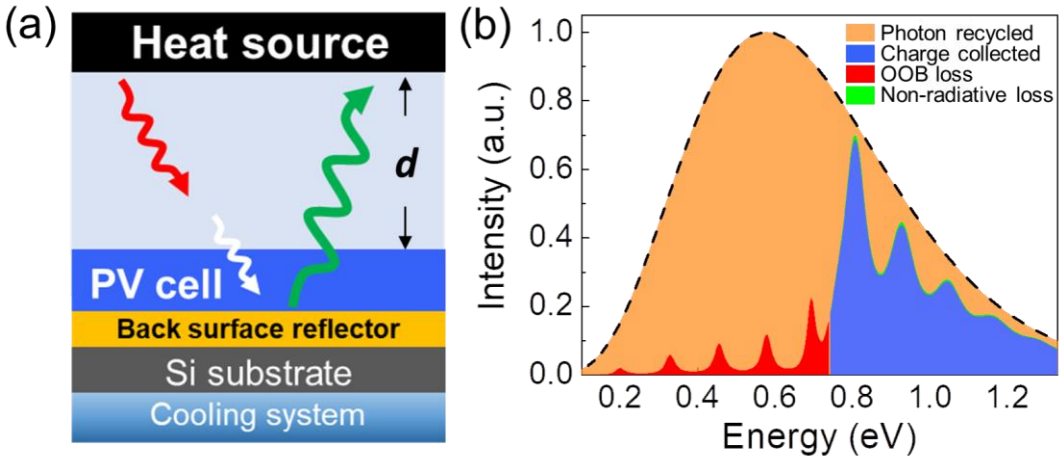

Figure 1.2 (a) Photon recycling between the back-surface-reflector of the TPV and the blackbody. The red, white, and green arrows indicate radiative heat transfer, absorption, and reflected photons, respectively. 'd' indicates the cavity gap formed between the emitter and the PV cell. (b) Power distribution of a thin-film InGaAs thermophotovoltaic with a gold reflector under the 1350 K blackbody illumination. The internal-quantum-efficiency is 98% and the non-radiative loss (green color) is substantially small.

to the heat source, which enables it to collect the reflected sub-bandgap photons at the back surface and re-distribute them into the PV cell again. The VF is determined by the distance (d) between the heat source and the PV cell, where radiative heat transfer modes are governed by propagating ($d \gg \lambda_{th}$: the thermal wavelength) or evanescent ($d < \lambda_{th}$) modes. The power conversion efficiency (PCE) of a PV cell is calculated using the ratio of electrical output power to incident optical power, where the electrical power is determined by the PV performance under light illumination. There are several factors deciding the PCE_{PV}: Shockley-Read-Hall (SRH) recombination; the number of extracted charges; the built-in-potential of the p-n junction; series resistance; and shunt resistance. The calculation of TPV efficiency involves the OOB reflectance as described in Fig. 1.2(a). The energy conversion efficiency is defined by:

$$PCE_{TPV}=PCE_{PV}\times\frac{P_{heat}}{P_{heat}-P_{reflected}}=\frac{P_{electrical}}{P_{incident}}\times\frac{P_{incident}}{P_{incident}-P_{reflected}}=\frac{V_{oc}\times J_{sc}\times FF}{P_{incident}-P_{reflected}} \quad (1.2)$$

where $P_{\text{electrical}}$ is the PV electrical power, P_{incident} is the power of the heat from a thermal source, $P_{\text{reflected}}$ is the reflected power back to the heat source, V_{oc} is the open-circuit voltage, J_{sc} is the short-circuit current, and FF is the fill-factor [1,48,53,54]. Owing to the recycling of sub-bandgap photons, the reflected power ($P_{\text{reflected}}$) is another possible source for power generation. Figure 1.2(b) shows an example of the power distribution of an Au-BSR InGaAs TPV under 1350 K blackbody illumination. The dotted line is the blackbody spectrum, and the orange-color-filled region is corresponding to the $P_{reflected}$. A large fraction of the $P_{reflected}$ is generated in the OOB region. As shown in Fig. 1.2(b), the absorbed power at in-band ($E_{ph} > E_g$) represents the charge generation by absorption in the diode, as indicated by the blue region in Fig. 1.2(b). The green indicates the loss by non-radiative recombination and the fraction determines the internal-quantum-efficiency (IQE) – the InGaAs diode has an IQE = 98% [1]. The in-band reflectance is mainly reliant on the absorption in the cell.

1.3 Spectral Efficiency Dependence on Out-Of-Band Reflectance

The operation of a TPV system is determined by several factors including the spectral irradiance from the heat source, the bandgap of a TPV cell, and a spectral filter. In Equation (1.2), increasing the heat emitter temperature (T_h) can supply more photons above the bandgap. This results in the improvement of P_{out}. The spectral efficiency (SE) is calculated by:

$$\text{SE} = \frac{\text{Number of electrons by absorption}}{\text{Total injected photons}} = \frac{E_g \times \int_{E_g}^{\infty} \varepsilon_e(E) \times \Phi(E) dE}{\int_0^{\infty} \varepsilon_e(E) \times E \times \Phi(E) dE} \tag{1.3}$$

where ε_e is the effective emissivity decided by the emitter and the TPV cell, and Φ is the spectral photon flux from the heat source [1,51,55]. The effective emissivity considers the recycled photons

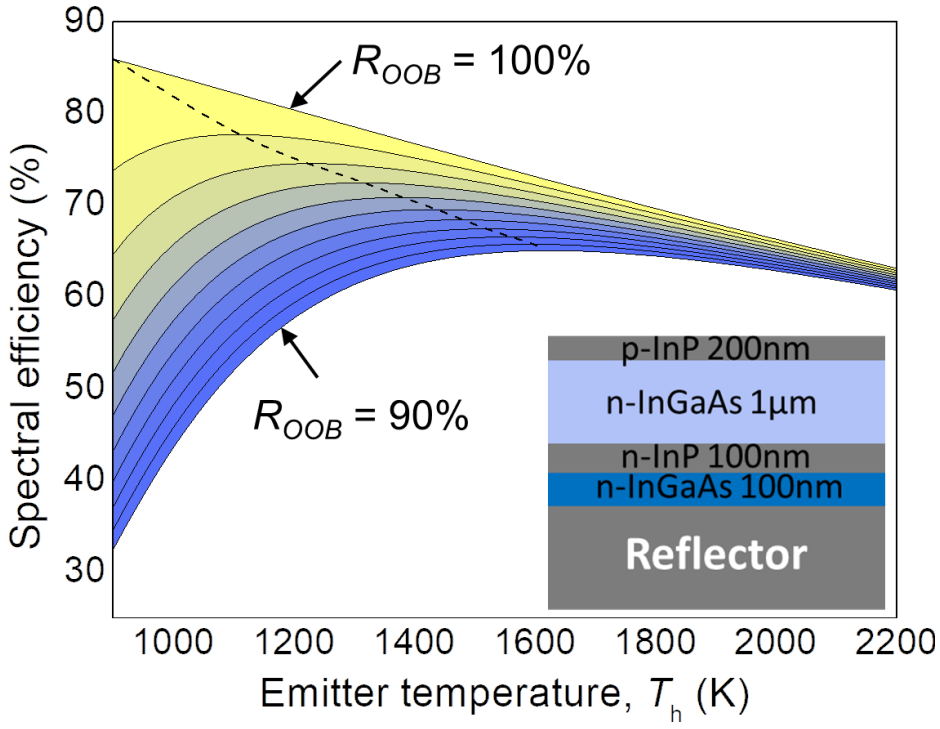

Figure 1.3 Simulated spectral-efficiency (*SE*) versus emitter temperature, T_h. The inset shows the InGaAs thermophotovoltaic (TPV) structure. The out-of-band reflectance (R_{OOB}) is numerically changed from 100 to 90% with interval (Δ) = 1%. The black dotted line indicates the maximum SE points.

by the cavity formed between the heat emitter and the TPV cell. Therefore, the emissivity is expressed by [47,55]:

$$\varepsilon_e(E) = \frac{1-R_e(E)}{1-R_e(E)\times R_{cell}(E)} \times A_{cell}(E) \tag{1.4}$$

where A_{cell} is the absorption of the PV cell above the bandgap, and R_e and R_{cell} are the reflectance of the emitter and the cell, respectively. Figure 1.3 shows the simulated SE as a function of emitter temperature with the different R_{OOB} from 100% to 90% with the interval of 1%. The inset indicates the simulated diode structure, where the InGaAs (In:Ga=0.53:0.47) is lattice matched to InP [1]. For R_{sub} = 100%, the SE is enhanced as the normalized bandgap increases. However, R_{sub} is easily smaller than 100%, where the losses are due to doped semiconductors and Fabry-Perot cavity

oscillations. Thus, the ratio of A_{cell} to R_{OOB} varies with T_{emit}, resulting in the trend of SE at different emitter temperatures. As R_{OOB} is decreased, the SE shows a relatively large drop as the T_{emit} decreases, meaning that this could limit available heat sources and TPV applications. Therefore, achieving high R_{sub} is important for high-efficient energy conversion.

1.4 Bandgaps, Materials, and Epitaxial Growth

Based on Eqs. (1.2) and (1.3), the bandgap of a TPV cell is the key to high efficiency by determining the boundary between in-band and sub-band wavelengths. Epitaxial growth using high vacuum systems is useful to tune bandgaps using III-V alloys. A solid source molecular-beam-epitaxy (MBE) system (Veeco GENxplor) [56] with valved As and P crackers is suitable for III-V compounds of InGaAs, InP, GaAs, AlGaAs, etc. Figure 1.4(a) shows the material bandgaps of the compounds as a function of lattice constant. By linear interpolation of the mole fraction dependence, Vegard's law (e.g., $A_xB_{1-x} = (x)A + (1-x)B$) determines the lattice constants and the bandgaps [57]. When the empirical model does not match the experiments, the law is modified by adding a bowing parameter, b (that is, $A_xB_{1-x} = (x)A + (1-x)B - bx(1-x)$). Lattice-matched growth is important for defect-free epitaxial layers. MBE growth on an InP substrate meets a wide range of materials with bandgaps ranging from 0.74 eV to 1.47 eV. A low-bandgap semiconductor can absorb photons in the near infrared. It permits a wide range of emitter temperatures for TPV operation. One of the applications of TPVs is to use the waste heat generated by steam-turbine power plants, which work at temperatures over 2200 K. In Fig. 1.4(b), the in-band area (left y-axis) and the corresponding power density (right y-axis) for blackbody radiation are shown. The low bandgap of 0.74 eV can promise utilization of a relatively large portion of thermal power over

a broad range of temperatures. Therefore, InGaAs (In:Ga = 47:53) with the bandgap of 0.74 eV is promising for developing a high efficiency TPV system.

The lattice constant of InGaAs grown by the MBE system is calibrated by measuring x-ray

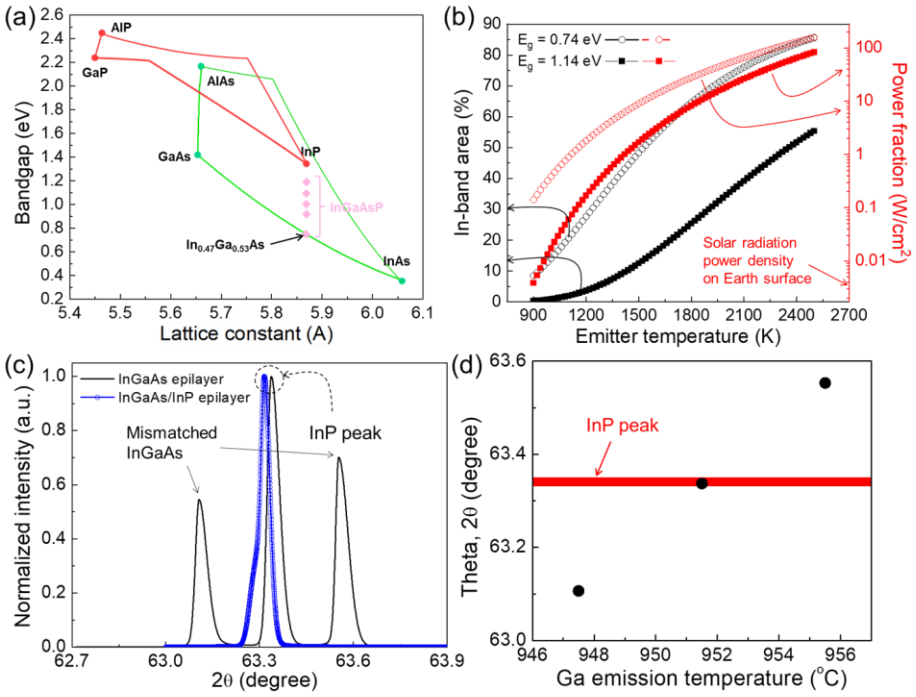

Figure 1.4 (a) Bandgap versus lattice constant for different III-V materials. The symbols indicated by InGaAsP mean the lattice-matched InGaAsP (Chapter 4) for 0.9, 1.1, 1.2, and 1.3 eV, respectively. (b) In-band area and available power fraction for blackbody spectrum versus emitter temperature. (c) X-ray diffraction measurements on InGaAs and InGaAs/InP epilayers. (d) Peak positions of the InGaAs epilayer in (c) as a function of Ga emission temperature.

diffraction (XRD) patterns. In zinc-blende structure ($a = b = c$), the lattice constant (a) in (004) plane is calculated using $a = c/4$ where $\lambda = c\sin\theta/2$. During growth, Ga/In ratio is controlled by changing the Ga Knudsen cell temperature. To avoid the possibility of degradation of the wafer surface by depletion of Group V material, it is necessary to maintain the overpressure for As flux

[58]. Figure 1.4 (c) shows the XRD measurements (Rigaku Smart Lab X-ray diffractometer with source Cu-Kα, λ = 1.5406 Å) for two different InGaAs samples. The InGaAs sample (black solid line) was prepared with three InGaAs layers grown at three different Ga K-cell temperatures. The XRD peak position is linearly proportional to the temperature, as shown in Fig. 1.4 (d). As a result, the linear interpolation finds the lattice-matched condition in the red box shown in Fig. 1.4 (d). In Fig. 1.4 (c), the InGaAs/InP sample (blue circles) was prepared using the lattice-matched growth condition. The sample is composed of InGaAs(0.1 μm)/InP(2 μm)/InGaAs(1 μm)/InP(0.3 μm)/InGaAs(0.1 μm). The XRD data is located near the InP peak, meaning that the InGaAs is latticed-matched to InP with the mismatch about 0.1% [59,60]. The InP peak positions in Fig. 1.4(c) are not fixed because the residual strain due to thermal expansion is not consistent between the different epitaxial growths.

1.5 Applications of Air-Bridge Thermophotovoltaics Cells

The AB-TPV architecture provides a means to enable near perfect photon utilization in the OOB region. Fan *et al*. reported an AB InGaAs TPV with R_{OOB} = 98.5% and efficiency near 32% at T_h = 1500 K (Cell temperature, T_c = 293 K) [1]. Based on the concept, our research goals are to extend the air-bridge architecture to further applications such as a μ-TPV system, near-field radiative heat transfer (NFRHT), and multi-junction TPVs.

The demand for micro-scale and high-power sources motivates the development of micropower devices [61]. The need for high power density and small volume is important due to the trend towards miniaturization of microelectronics and wireless micro-systems. A concept by Epstein and Senturia provided a description to generate power and heat using a micro-heat engine and power MEMS [62]. This gives insight to develop small-scale portable power generators. The

μ-TPV system is a promising power source for micro-electronics and MEMS. The dimension of the TPV cell is important for the application to microelectronics (on the order of a few cm^3) [63]. Considering the 10% or less efficiency reported by others [63,64], the demonstration of air-bridge μ-TPV cells can realize high efficiency micro-power generators. However, mechanically unstable TPV membranes with buckling [1,65] cannot yield μ-TPV cells integrated with the system components such as a micro-turbine, radiative emitter, and maximum power-point tracker. In particular, Au-Au cold welding to transfer III-V materials to a cell substrate generates compressive buckling or cracks. Therefore, understanding the mechanism and finding solutions are important to extend the uses of air-bridge architectures.

Another application of the air-bridge μ-TPV cell is energy conversion using NFRHT. The operation of a TPV system under far field radiation only utilizes propagating modes. This limits the power density of the system by the Stefan-Boltzmann law, which determines the upper limit for the far field radiation. In the near-field regime for the distances smaller than the thermal wavelength ($\lambda_{th} = {hc}/{2\pi k_B T}$, h: Planck's constant, k_B: Boltzmann's constant) between two close blackbodies (a heat source and a TPV cell), the heat exchange is dominated by evanescent waves, having surface modes (evanescent in the heat source and the vacuum gap) and frustrated modes (evanescent by total internal reflection at the heater-vacuum interface). Photon tunneling of the evanescent waves enables NFRHT, exceeding the power limit of the propagating waves [50,66-69]. A recent report of an Au-BSR InGaAs TPV realized the measurement of the NFRHT effect at nanogap proximity (~100 nm) between the TPV and a Si emitter [66]. This work reports 7% efficiency with the primary power loss caused by the large energy flux transfer in the OOB region. Therefore, the air-bridge μ-TPV demonstration can provide a way to suppress the absorption and improve the efficiency.

A multi-junction (or tandem) photovoltaic cell can overcome the Shockley-Queisser (SQ) limit of a single-junction cell. Conventional tandem structures involve heavy doped tunnel junctions (TJs), which electrically connect sub-cells [70-72]. Heavy doped thin films absorb OOB photons by free-carrier absorption (FCA) which generates a few percent loss of R_{OOB}. Simultaneously, tandem structures demand lattice-matched material growth on a wafer involving the TJs, meaning that possible materials are constrained to only a few alloys. Thus, the development of a tandem architecture that is TJ-free with a broad range of material partners is important to employing air-bridge reflectors in multi-junction TPVs.

1.6 Challenges of the Air-Bridge Thermophotovoltaic Architecture

Residual stresses cause compressive buckling of thin films due to mismatch of thermal expansion coefficients [73-75], poor adhesion at the interface of different materials [76-78], plastic deformation [65,79], etc. Computer simulations and mathematical calculations reveal causes for each different buckled shape. Whereas some researchers have reported that buckled thin-film structures have potential for applications such as optoelectronics [80,81], bioelectronics [82], and metamaterials [83-88], structural failures including delamination and cracks are detrimental for most electronics applications.

The thin-film epitaxial growths require specific substrates for the lattice-matched pseudomorphic epitaxial thin-film growth. To employ the spectrally selective method [2,4-6], the epilayer needs to be transferred to another substrate including a thin-film reflector and metal electrode. For example, III-V materials such as InGaAs and InP grown on InP wafers can be transferred to a Si wafer using a thermal compression cold-welding technique. Figure 1.5 illustrates how a III-V epilayer is moved to a silicon substrate. (1) The epitaxial layer with Au grid lines is

grown by molecular beam epitaxy, e-beam deposition of the Au film, and conventional photolithography. (2) The epitaxial layer is bonded onto a Si substrate, and coated with Au, by cold welding. (3) The thick substrate stabilizes the epitaxial film during bonding. The pressure of air or vacuum in the space between the Au grid lines determines the deformed shape of the film, and thus the direction of the compressive strain through the bottom surface of the epilayer. (4) After removal of the substrate, the Au deformation generates the buckled morphology as illustrated in (5).

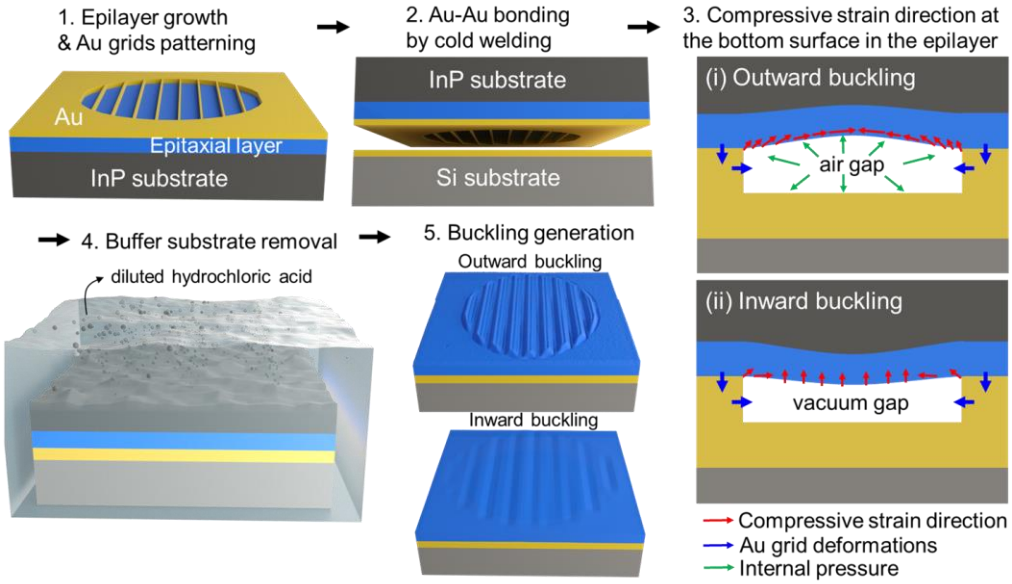

Figure 1.5 Schematic of the fabrication process to transfer the epitaxial layer to Si substrate using Au-Au bonding process. Owing to the deformed Au gridlines, the epilayer on the air-gap forms compressive buckled metamaterials. Figure reproduced from ref. [66].

The reflectance spectrum of an air-bridge architecture is affected by the cavity-interference determined by the PV thin-film structure and the thickness of the air-bridge. The compressive buckled III-V membrane has downward or upward morphology. Therefore, the buckled III-V morphology has multiple air-cavity thicknesses, resulting in a broadening of the resonant cavity peaks which causes additional loss of R_{OOB}.

A recent AB InGaAs TPV structure formed free-standing III-V thin films above 75-μm-wide air cavities between Au-gridlines, where the films are buckled downward by about 200 nm [1]. Buckled membranes have average strains <1%, owing to a low fracture limit (<1%) of solid materials. Importantly, the presence of buckling results in fragile structures. A severely buckled membrane does not have a consistent air-cavity depth, generating the broadening of cavity oscillation peaks by multiple Fabry-Perot cavity modes. Therefore, for practical applications of AB-TPV architecture, achieving non-buckled, high R_{OOB}, and high P_{out} are important.

To demonstrate a multi-junction TPV cell without TJs, we design a tandem cell having an Au interlayer where patterned Au gridlines on two sub-cell surfaces are cold weld bonded. Between the grids, we insert an air-bridge allowing high photon utilization. Insertion of polymers at the interlayer electrically isolates the sub-cells from each other. The challenges are the efficiency calculation and the optimization of fabrication processes.

At T_h = 1500 K, the first AB-TPV using InGaAs reports a 32% efficiency, where V_{oc} ~0.45V, J_{sc} = ~1A/cm^2, and FF = ~71% [1]. Omair *et al*. developed an Au-BSR InGaAs with a 29% efficiency, where V_{oc} = ~0.53, J_{sc} = ~0.9A/cm^2, and FF = ~73% [89]. The Au-BSR TPV can achieve ~38% efficiency when assuming that the Au-BSR is replaced with the air-bridge reflector. These results suggest that we still don't know the efficiency limit of AB-TPVs with detailed balance. Studying the efficiency limit based on detailed balance can reveal the factors restraining the practical TPV performance.

1.7 Flow of Dissertation

In this dissertation, we discuss a new AB-TPV architecture designed for various applications. First, we reveal the mechanism of compressive buckling on free-standing III-V

membranes. A finite-element-analysis (FEA) simulation validates the findings of the main factors causing the buckled membranes. Experimental demonstrations show a wide range of controlled buckling heights from nanometers to microns. Finally, this study provides a solution to control the buckled III-V morphology.

A compressive buckled TPV cell makes it difficult to produce a reliable AB-TPVs with high yield and high R_{OOB}. It limits applications such as μ-TPVs, NFRHT, large-scale AB-TPVs, and multi-Ab tandem TPVs. Therefore, we designed an AB-TPV using an InGaAs/InP heterostructure that can mitigate compressive buckling as well as have highly efficient *J-V* performance. Using multiple methods including FEA, numerical methods, a technology computer-aided design (TCAD) simulator, and the transfer-matrix-method (TMM), we predict the diode performance and manage the risk factors for experiments.

We developed non-buckled InGaAs AB-TPVs with sub-centimeter diameters. We characterized the cells using the Fourier-transform-infrared (FTIR) spectroscopy, laser-confocal 3D microscopy, scanning electron microscopy (SEM), and TCAD simulation. The characteristics are compared to an Au-BSR InGaAs TPV, then we show the effect of the air-bridge architecture. Finally, the efficiency of the AB-TPV cell was measured using a SiC emitter by varying the temperature from 900 to 1500 K.

A single-junction TPV efficiency is limited by detailed balance. Electrical output power can be improved using multi-junction TPVs. However, conventional tandem PV structures require heavy-doped ($>1\times10^{19}$ /cm^3) tunnel junctions, which induce considerable parasitic absorption by free carriers. Therefore, we proposed a tandem PV structure that has an interlayer to bond Au gridline layers between sub-cells. A polymer film is inserted at the interlayer, serving as an insulator between the cells. The scheme eliminates several challenges: heavy-doped tunnel

junctions and lattice-matching conditions between the two cells are not required. The demonstrations include homo-tandem InGaAs TPVs with two or four terminals.

Chapter 2 Understanding and Control of Compressively Buckled Semiconductor Thin Films

2.1 Introduction

Recent developments of advanced micro- and nanomaterial applications, such as optoelectronics [80,81], bioelectronics [82], wearable electronics [90], compressively buckled three-dimensional (3D) mesostructures [80,91-95], and metamaterials [10–15], demand device configurations that are inaccessible to conventional photolithographic processing. During the last decades, researchers have grafted stress-induced techniques onto existing two-dimensional (2D) systems, providing promising routes to transform planar thin-film surfaces and structures into 3D forms using prestrained elastomeric substrates [91-95], residual stress by thermal expansion coefficient mismatched materials [73-75], and topological transformations [96,97]. Among them, thin films buckled by residual stresses have resulted in ribbons and wrinkled 3D mesostructures based on Si [98-100], GaAs [101-103], graphene [104-106], and MoS_2 [74,107-109]. Films with straight-sided, telephone-cord (TC) [76-78], and web-network patterns [74,108], have been developed using film delamination or blisters at the interfaces between substrates and films. A prestrained soft substrate has enabled both upward and downward buckling in thin films [110]. However, these methods require relatively high temperatures, and mismatches of thermal expansion coefficients, thereby limiting the range of available materials, accessible buckling dimensions, and shapes. Here we present a method to compressively buckle free-standing group III-V alloy semiconductor thin films suspended between Au grid line supports. The demonstration

resembles classical buckling formed by thermal residual stresses, blisters, or film delamination [73-78]. In contrast to earlier work, however, the deformation of micron-scale structures results from a combination of a compressive, inward distortion of the Au supports forming a cavity enclosed by the bridging thin film, and a thermally induced increase in air pressure within the cavity during bonding that pushes the film away from the substrate. The free-standing semiconductor structures are inspired by their recent use in air-bridge thermophotovoltaic (TPV) cells, where the air cavity between the thin-film active region and a Au back reflector results in an extremely high reflectivity required for this application [1]. We show a wide range of buckling heights, ranging from nanometers to tens of microns. Finite element analysis (FEA) accurately predicts the morphology transformation from 2D to 3D in the free-standing thin films. The micron-sized upward buckling is accurately modeled via classical Euler beam theory [111,112]. Using this theory, we explore a diversity of buckled metamaterials including nearly flat, extreme upward buckling, TC buckling, and domelike buckling. The fabrication process is compatible with conventional 2D lithography and produces a range of controllable morphologies useful for the formation of precisely shaped metasurfaces required in air-gap devices for energy harvesting, optics, and sensing.

2.2 Materials and Methods

The Si substrate is treated in a buffered hydrofluoric acid solution to remove its native oxide. It is ultrasonically cleaned in acetone, isopropyl alcohol, and deionized water, and then dried in a stream of N_2 gas. A Ti(30nm)/Au(500nm) contact layer is deposited by electron-beam evaporation on the precleaned Si wafer. The epitaxial films are grown on the (100) surface of an InP wafer by solid-source molecular beam epitaxy. The 500- nm-thick Au grid lines are deposited

on the epilayer using electron-beam-evaporation and patterned using a conventional lift-off process. To bond the Au on the epilayer to that on the Si substrate, the wafers are brought into contact, and the sandwich is loaded into a wafer bonding chamber (EVG 510 and EVG 520, EV Group Inc., Tempe, AZ, USA) in air. Compressive, upward buckling is achieved by applying a uniaxial bonding force in air, whereas downward buckling is achieved by bonding in vacuum. A bonding pressure of 2 kN (20 N/s ramping rate) is applied at the top of the InP wafer at 150°C for 5 min, and subsequently the sample is cooled to room temperature. The InP substrate is etched away by immersion in dilute hydrofluoric acid (HCl) (1:1) for 8 h. Post buckling analyses are supported by FEA using COMSOL Multiphysics v.5.5. A physics option for solid mechanics (Solid Mechanics) is used to calculate the structural deformation. To simulate the strain distributions during cold welding in three dimensions, we assume that the bonding force is applied in the z (i.e., normal) direction. The initial air pressure in the cavity is 0.101 MPa (1 atm). The bonding force increases the internal pressure to 1 MPa, which is adjusted to fit the measured buckling heights. A uniaxial force of 2000 N is applied to the Au grid lines along z. The displacement of the bottom boundary of the modeled structure is constrained, as in the experiment. We use experimentally extracted mechanical parameters for InGaAs, multilayers, and Au materials provided in Table 2.1.

Table 2.1 Extraction of mechanical properties by nanoindentation.

Material	Reduced Young's modulus (E_r) (GPa)	Hardness (GPa)	Young's modulus (E_y) (GPa)	Poisson's ratio (v)
$In_{0.53}Ga_{0.47}As$	104.01	9.8	101.94	0.33
Au	102.4	1.84	90.68	0.44
III-V multilayers	90.61	6.39	87.68	0.33

Noncontact optical 3D profilers are used to characterize the buckling shapes, (Zygo NewView 5000, Zygo Corporation, Middlefield, CT, USA, and Olympus OLS 4000 LEXT, Olympus Corporation, Tokyo, Japan). Profilometer line scans are performed by a diamond-tip stylus tool (Bruker, Dektak XT, Bremen, Germany) with a minimum force of 9.8 μN. Nanoindentations are carried out by a Hysitron Ti 950 Tribo-indenter with a Berkovich sharp diamond tip to measure the Young's modulus (E_y) and hardness. A spherical indenter (50 μm 90° conical probe) is used to measure inelastic deformations on planar and buckled surfaces. Film crystallinity is determined using the Cu Kα 1.5418 Å radiation at 40 kV and 44 mA using a Smartlab diffractometer (Rigaku Corporation, Tokyo, Japan). A confocal laser optical profilometer (LEXT OLS 4000, Olympus, Tokyo, Japan) is used to measure the profiles of the Au grid lines before and after transfer onto a Au-coated Si substrate. The 500-nm-thick Au grid lines are formed on a precleaned InP substrate using a lift-off process. The grids are transferred to the Si substrate by cold welding (10 MPa at 150°C in air for 5 min). After removing the InP substrate, the grid profile at the same position is also measured.

2.3 Free-standing Thin-film Structure for Compressive Buckling

As illustrated in Fig. 1.5, the buckled thin-film structures are selectively formed on the free-standing films suspended between Au grids. A crystalline semiconductor multilayer (ML) thin film is comprised of epitaxial $In_{0.53}Ga_{0.47}As$ (0.2μm; Be-doped, 1×10^{18} cm^{-3})/InP (0.1μm; Be-doped, 1×10^{18} cm^{-3})/ $In_{0.53}Ga_{0.47}As$ (1.0μm; Si-doped, 1×10^{17} cm^{-3})/InP (0.1μm; Si-doped, 1×10^{18} cm^{-3})/ $In_{0.53}Ga_{0.47}As$ (0.1μm; Si-doped, 1×10^{18} cm^{-3}) on a (100) p-type InP substrate. **Step 1**: The 500-nm-thick Au grids with 100 μm spacings are photolithographically patterned onto the epitaxial layer surface. A 2D beam structure is defined across the grid lines, where the free-standing

membrane (the "beam") spans the grids (the "beam supports"). **Step 2**: To transfer the epilayers from the InP substrate to a Si substrate precoated with Au, the facing surfaces are pressure bonded to form a metal-metal weld at 150°C in air (**Step 3**: see Sec. II) [1,32,113]. **Step 4**: After bonding, the InP substrate is removed by selective wet etching, resulting in thin-walled cavities enclosed by the Si, the membrane, and the supports. **Step 5**: The bonding force compresses the Au grids, distorting them into the cavities. This offers an opportunity to apply lateral loading to the free-standing film. The force reduces the volume, causing the internal air pressure (P_i) to increase, thus forcing the beam upward, away from the substrate. The supports remain deformed, and P_i is higher than the initial air pressure ($P_{init} \approx 0.101$ MPa). As a result, the deformed supports and the P_i generate parallel compressive strains at the bottom surface of the film. On the other hand, when the empty spaces are evacuated, P_i is lower than P_{init}, and the film flexes downward. Once the cavity is evacuated, it is compressed during the bonding step. The bottom surface of the epilayer is then tensile stressed—here the compressive stress direction is normal to the tensile stress. Thus, control of the initial internal pressure determines whether the buckled morphology is upward or downward. Although the semiconductor and the Au films have different thermal expansion coefficients [InP and $In_{0.53}Ga_{0.47}As$, 4.60–5.66×10^{-6}/K; Au, 14×10^{-6}/K], the bonding temperature is sufficiently low that the residual thermal stress is negligible at the Au-Au bonding interface and at the interface between the semiconductor and the Au films. During the bonding phase, the air cavity is heated to 150°C, and its volume expands. Since the materials surrounding the cavity are stiff, the volume expansion is small and is released upon cooling. Nevertheless, the Au grids remain slightly distorted. This results in a residual elevated pressure that causes the buckled morphology.

2.4 Experiment and Simulation for Compressive Buckled III-V Metamaterial

The microscope image in Fig. 2.1(a) shows a 1-mm-diameter circle with multiple Au grid lines supporting the upwardly buckled free-standing film. The longitudinal grid lengths in the y direction vary from left to right, whereas in the x direction, the 100-μm gap between the supports is constant, except in the boundary regions of the circle that determine the beam length. The thin-walled beam structure extends to the periphery of the circle. The buckling shapes and sizes of the membrane are determined by the 100-μm gaps. From classical Euler beam theory [114,115], the upward buckling is achieved by axial force loading of the beam when a critical loading force (P_{cr}) and a stress (σ_{cr}) are less than the yield strength (σ_y) of the free-standing material. During bonding, the distortion of the grid results in P_{cr} lateral to the film. Then compressive buckling follows:

$$\frac{P_{cr}}{A} = \sigma_{cr} = \frac{\pi^2 E_y I}{A(l_t)^2} = \frac{\pi^2 E_y}{\left(l_t/r\right)^2} < \sigma_y, \tag{2.1}$$

where A is the beam cross-section area in the buckling direction [x axis in Fig. 2.1(a)], E_y is its Young's modulus, l_t is the effective beam length, I is the area moment of inertia of the beam cross section, and $r = h_t/\sqrt{12}$ is the radius of gyration for a rectangular beam of thickness (h_t). The slenderness ratio is l_t/r. The beam length along the x axis is l_{tx} = 100 μm; the lengths along the y axis (l_{ty}) are longer than l_{tx}, although they differ through the buckling regions. The slenderness ratios range from 230 to 2300, where $\sigma_{cr} < \sigma_y$ ~100 GPa for the InP/InGaAs film (see Appendix A1) [116].

Figure 2.1(b) shows a FEA simulation of the experimental compressive strain distribution in the thin film during bonding (see Appendix A1, Fig. A1 for modeling methods). The strain in the film at the grid lines is approximately zero, whereas nonzero compressive strain appears in the free-standing film. The Young's modulus (E_y) and hardness of the InGaAs, epitaxial layers, and

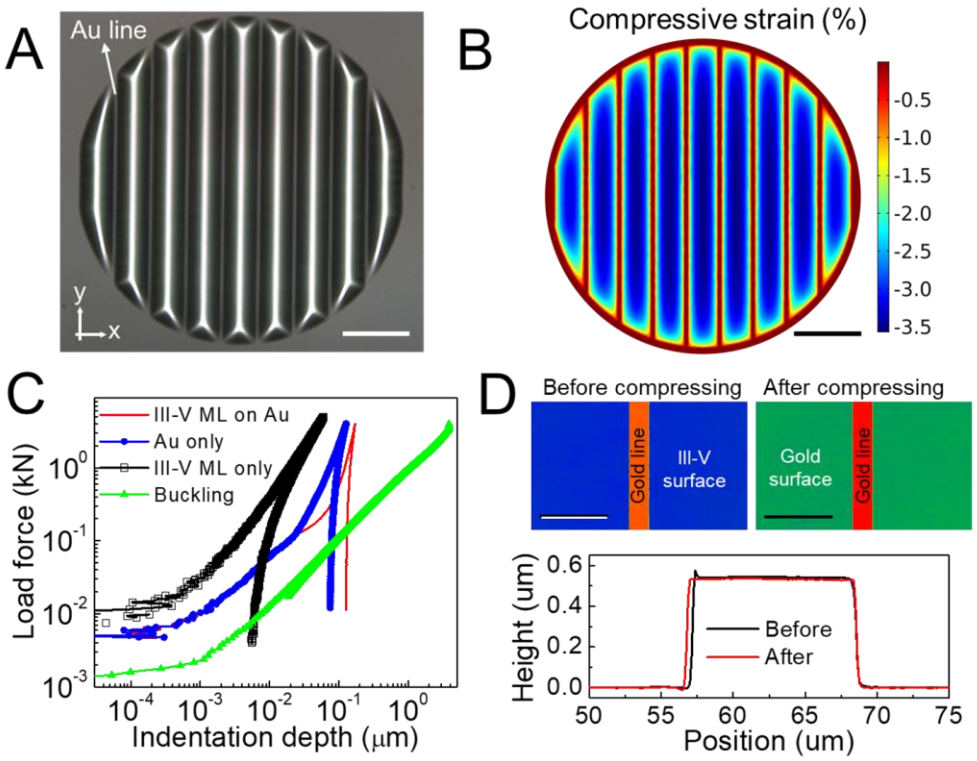

Figure 2.1 Buckle generation by compressive strains and stresses. (a) Optical microscope image of the buckled sample with the grid line spacing of 100 μm. Scale bar, 200 μm. (b) Simulations of the compressive strain distribution in the film. Scale bar, 200 μm. (c) Load-displacement curves of III-V ML, Au, III-V ML on Au, and buckling using a spherical indenter. (d) Profiles of the Au grid line before and after compression. The top images are observed by a laser confocal microscope at the same position. The scale bar is 40 μm. The bottom graph shows the profilometry results.

Au films are extracted by nanoindentation employing a 50–200-nm-radius diamond tip on a three-sided pyramid Berkovich probe (see Appendix A1, Fig. A2). In Table 2.1, the difference in E_y between Au and semiconductor films is about 10%, but the Au hardness is noticeably lower than that of the semiconductor, resulting in a larger Au grid deformation. To characterize the deformation, microindentation measurements are performed using a 50-μm-radius spherical probe tip, with results shown in Fig. 2.1(c). Owing to its higher hardness, the semiconductor membrane endures large loading forces without significant plastic deformation relative to the Au film. This

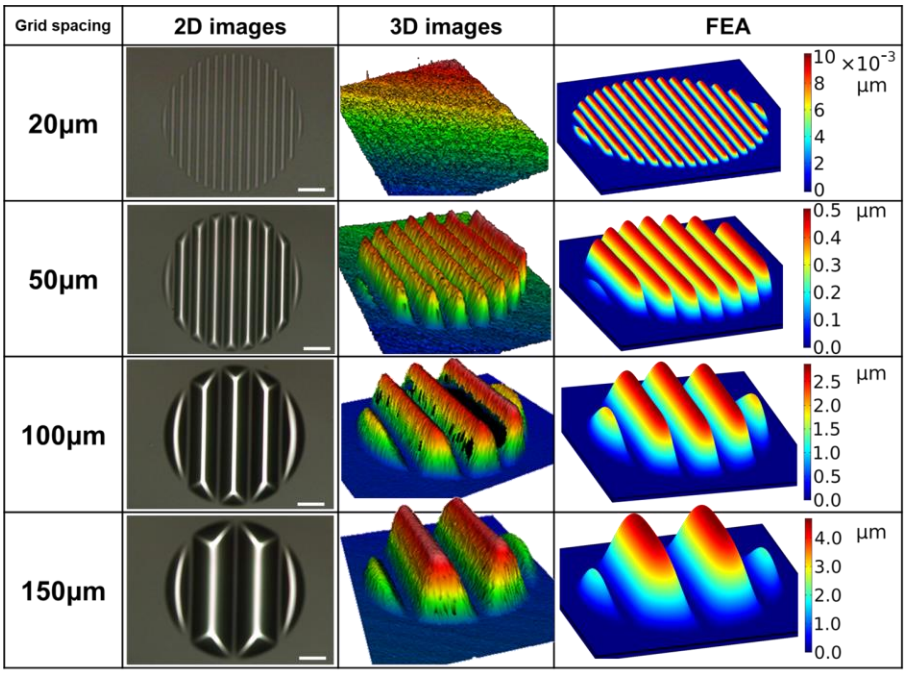

Figure 2.2 Scalable semiconductor microstructures and strains. 2D and 3D optical images, and FEA simulations of the compressively buckled mesostructures with different Au grid line spacings. Scale bars, 100 μm. The legends indicate the displacements. The experimental buckling heights are in the Appendix A1, Fig. S5.

allows structural deformation of III-V materials that follows the Au surface shape. The same microindentation is performed in the distorted region. The loading and unloading curves overlap and exhibit a linear relationship between the displacement and the loading force. The maximum indentation depth is 3.8 μm at 3.4 kN. Once a buckled morphology is formed, it is elastic and rapidly responds to external forces while maintaining its mechanical stability. To investigate the dependence of the grid distortion on pressure, we trace the grid profiles using laser confocal microscopy before and after transferring the grid lines onto a Au-coated Si substrate [Fig. 2.1(d)].

The grid height is compressed by approximately 1.6% and the grid width is extended by 3.5%. Further, the compressively buckled features have a Gaussian profile, viz.:

$$h_b(x) = A \times e^{\left\{-\frac{1}{2}[(x-x_c)/w]^2\right\}} \tag{2.2}$$

where $h_b(x)$ is the buckling height, A is the amplitude of the distortion, x_c is the peak center, and w is its width.

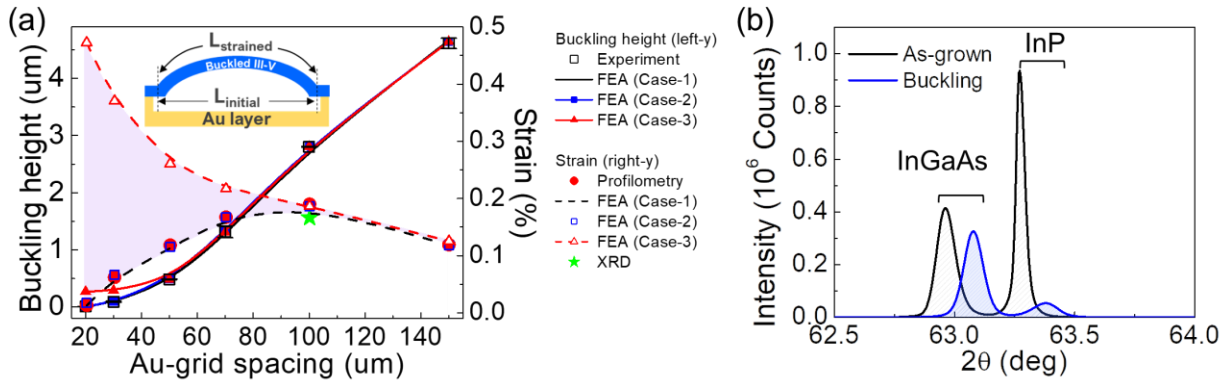

Figure 2.3 Strains in the buckled semiconductors. (a) Buckling heights and numerically estimated strains. The simulations show three cases: there is no Au deformation in case 1, and cases 2 and 3 assume that the Au grid lines are plastically deformed by the compression forces of 70 N and 2 kN, respectively. Inset: Illustration of the buckled film defining variables used in text. (b) XRD patterns on the as-grown versus the buckled metamaterial. The black curve is the XRD pattern of the as-grown thin film, the blue curve is the XRD pattern of the buckled film.

Figure 2.2 shows a set of experimental buckled, 0.5-mm diameter circles with different grid spacings. The 3D FEA simulations accurately predict local pop-up buckling of the free-standing films resulting from the residual stress from the Au-grid deformation. Details of the simulation methods are provided in the Appendix (see Appendix A1, Note 3, and Fig. A3). The FEA simulations also predict the upper and lower bounds of the strains in the buckling with two boundary conditions: one is the Au grid line deformation, and the other is the internal pressure in the air cavity. Further definitions of variables that characterize the film profile are found in the inset of Fig. 2.3(a). Owing to the uncertainty of the quantitative analysis of the pressure-density

relation and Gauss's theorem in the air cavity [45], the internal pressures are numerically estimated to fit the simulated buckling heights to experiment in Fig. 2.3(a). The FEA case 1 corresponds to buckling without structural distortion of the Au grids. The internal pressures are appropriately adjusted to match the buckling heights (h_b) equivalent to the measurements. From the results, the black-dashed line gives the strains in the buckled III-V thin films (see Appendix A1, Note 3, and Fig. A3). The strain increases with increasing spacing, and then decreases when the spacing is larger than 100 μm. As expected, the effect of the internal pressure caused by Au deformation weakens as the cavity volume increases. Case 2 assumes the Au grids are distorted by the 70 N compression force. The buckling heights and strains are comparable to those in case 1 for forces less than 70 N. On the other hand, case 3 includes the plastic deformation of the Au grid lines by the welding force (2 kN) applied in the normal direction. At grid line spacings less than 70 μm, the calculated buckling heights are larger than those in found experimentally even though the internal pressures are set to zero. Additionally, by reducing the grid spacing, the strain (red-triangle-dashed line) is significantly higher than in cases 1 or 2. This implies that the variations of the strain and height are more strongly affected by Au deformation at relatively small grid spacings. Interestingly, at a large grid spacing, the simulated strains are not significantly different in the three cases. The Au distortion generated by a given loading force is inversely proportional to the contact area. That is, the upper and lower bounds of the strains rely on the cavity spacing, the grid design, and the mechanical properties of the materials used. The experimental strains (red-filled circles) are determined using profilometry, where the initial lengths of $L_{initial}/2$ [inset, Fig. 2.3(a)] are adjusted to fit the lower bound line (see Appendix A1, Note 1). Fits, fitting parameters, and FEA simulation methods are found in Fig. A4, Table S1, Note 4 in Appendix A1 for several grid spacings. From these results, the buckling height and strain (ε_b) are shown to be functions of

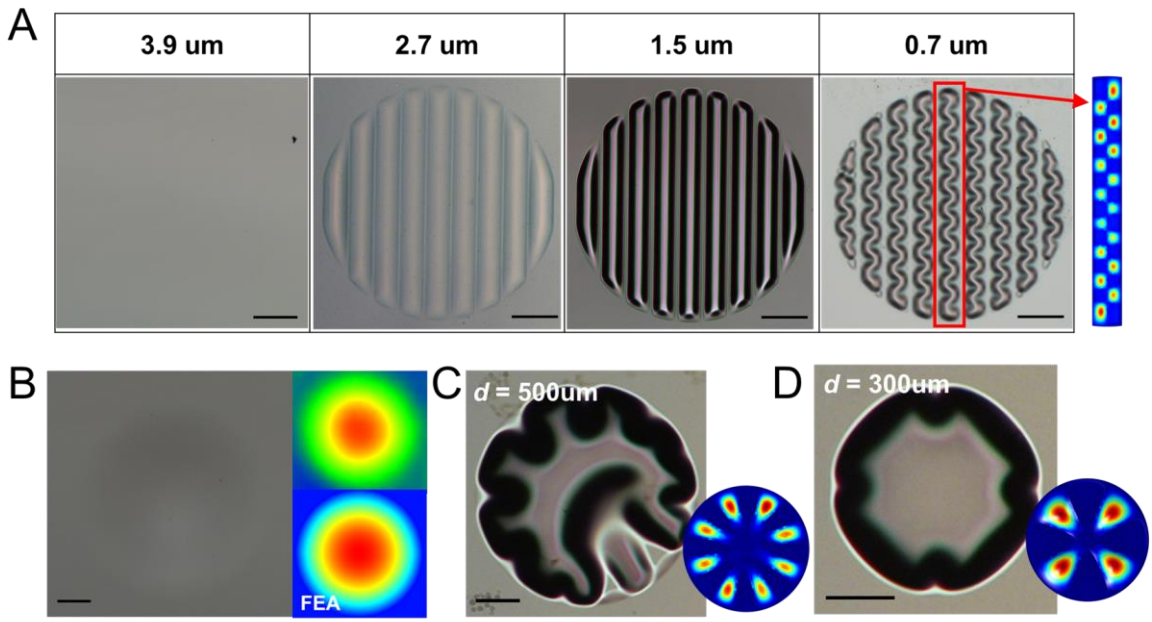

Figure 2.4 Film thickness dependence. (a) Optical microscope images of buckling morphologies for various film thicknesses. The Au grid line spacing is 100 μm in the 1 mm diameter circles. The buckling transitions to a telephone cord (TC) morphology at 0.7 μm. Scale bars, 200 μm. FEA accurately predicts the postbuckling peak positions for TC buckling. (b) Buckling in 600 μm diameter circles for a film thickness of 2.7 μm. Scale bar, 100 μm. The top-right image is measured by a laser confocal microscope, the bottom indicates the FEA result. Geometrically segmented buckling for (c) 500 and (d) 300 μm diameter circles. Scale bars, 100 μm. The FEA results accurately predict the buckling peak positions.

grid line spacing. The stiffness of the structure is proportional to $E_y I/l^3$. For example, the grid line spacing only varies from 20 μm to 150 μm by 7.5 times, but the stiffness is dynamically changed by $7.53 \approx 422$. Therefore, the buckling height maximum, h_b, increases from 10 nm for a grid spacing of 20 μm, to 4.5 μm for a spacing of 150 μm. Remarkably, the buckling height at the same grid line spacing is unaffected by the circle diameter (see Appendix A1, Figs. S5 and S6) when it is greater than the spacing. While the fracture limit of the semiconductor is 1% – 2%, the strains are $\varepsilon_b < 0.3\%$. Hence, the buckling process is nondestructive to the suspended film. The buckling

patterns show a controllable range from nanometers to microns, depending on the grid structures, materials, and the fracture limit of the membrane.

Figure 2.3(b) shows x-ray diffraction (XRD) patterns of the as-grown epitaxial film and the buckled metamaterial. The left and right peaks correspond to the InGaAs and the InP layers, respectively, with a lattice mismatch of 0.4%. However, the critical thickness ($h_c = a_{epi}/2f$, where a_{epi} is the lattice constant of an epilayer and f is the lattice mismatch) to relax the elastic strain energy accumulated in the epitaxial layer, particularly close to the interface, is approximately 70 nm. This is smaller than the total layer thickness, indicating that the lattice-mismatched layers are relatively free of defects. The diffraction peaks in the buckled sample are shifted to a larger half angle, θ, for the buckled film, indicating compressive strain (see Table 2.2). At the InGaAs peak center, the shift is $\Delta(2\theta) = 0.117° \pm 0.003°$, corresponding to a compressive strain of $0.1664\% \pm 0.0047\%$.

Table 2.2 XRD measurements on the as-grown and buckled thin films.

Samples	Materials	2θ (deg)	Full width at half maximum
As-grown films	InGaAs	62.96	0.093
	InP	63.27	0.046
Buckled metamaterial	InGaAs	63.08	0.098
	InP	63.38	0.134

After loading, the curvature is determined by the buckling mode. The effective beam lengths are approximately 50% to 70% of the grid line spacings (W_g) (see Appendix A1, Table S2), consistent with the Euler's assumption for a beam fixed at the Au grid supports. In Fig. 2.4(a), film thicknesses from 1.5 to 3.9 μm result in buckling heights from 2.5 μm to 30 nm, respectively.

FEA predicts that a 5-μm-thick epilayer achieves nearly zero deflection at the same grid spacing. The TC morphology at the buckling mode transition is achieved at 0.7 μm, arising from geometric imperfections in the grids [46–48]. In contrast, thicker layers are undisturbed by imperfections in the thin-walled beam structures. The FEA accurately predicts the sinusoidal buckling peak positions in the free-standing film, as shown to the right of Fig. 2.4(a). Figures 2.4(b)–(d) compare the buckling attained by removing the grid lines within the circles. In Fig. 2.4(b), the film thickness is 3.9 μm, resulting in a uniform dome shape. The air volume expansion depends on the pressure applied during cold welding and the film thickness (see also Appendix A1, Fig. A7). Figures 2.4(c) and 2.4(d) show the buckling mode transition when the film thickness is decreased to 0.7 μm. The dome is transformed into four and eight segmented circles whose peak positions are accurately predicted by FEA. The resulting mesostructures show geometrical complexity that offers opportunities to access a diversity of 3D shapes. On the other hand, the zero-deflection free-standing microstructures can enable high reflectivity air-bridge III-V photovoltaics [1] in near-field radiative heat transfer applications [50,66]. Additionally, since the microstructures are elastic, they provide a platform for sensitive pressure sensors and optical elements [117,118].

2.5 Discussion

In this chapter, we presented a comprehensive study of the compressive buckling of free-standing semiconductor thin films that controllably transforms flat inorganic microstructures into scalable, buckled metamaterials. The study applies classical Euler beam theory where the thin inorganic semiconductor membrane constitutes a beam suspended between Au grid line supports. The accuracy of this approach is confirmed by experiment and FEA that quantitatively predicts the scale and shape of the deformation as a function of material elastic properties, beam length, thickness, and loading conditions. The strain is smaller than the elastic limits of inorganic

materials, and hence does not result in fracture of the brittle, crystalline inorganic thin films, and yet is large enough to achieve a wide range of deflections from nanometers to tens of microns. The distortion is eliminated as the film thickness is increased to approximately 5% of the span length. A flat surface is required in applications such as in high-efficient near-field photovoltaic heat transfer [50]. In contrast, the buckled semiconductor linearly responds to an external force, offering applications in sensitive pressure sensors in electronic skins, medical devices, and wearable devices, as well as in deformable optical elements. The results presented can readily be extended to different beam and grid line materials. Using the known mechanical properties of a free-standing thin-film membrane and the beams in our models, we can accurately predict the extent to which the metamaterial is distorted, and the robustness of the free-standing layer. While we only demonstrate the 3D structures comprising an elastic beam spanning thin Au grid lines, the results deliver a means to explore a broad range of structures on mixed materials platforms with different designs. The controllable buckling of metamaterials has potential for creating precisely designed mesostructures and metasurfaces.

Chapter 3 Demonstration of Non-Buckled Air-Bridge Thermophotovoltaic Cells

3.1 Introduction

Fossil fuels have been the primary sources for most of the energy consumption in the sectors of building, transportation, and industry [38,40,119]. However, the use of fossil fuels has resulted in environment issues such as global warming, climate changes, deforestation, and a limitation of resources [11,12,119]. This has attracted increasing attention to non-fossil fuel resources and energy conversion methods to generate electricity. Among many methods, TPV power generation systems can convert heat to electricity and have been investigated in major energy sectors for the efficient use of fossil fuels as well as non-fossil fuel resources [55,120]. The recent progress of TPV systems shows the potential for high output power density, high conversion efficiency, overcoming the SQ limit, and versatile fuel usage [1,54,66,89]. By adopting spectral selectivity techniques, preserving and re-using of photons below bandgap can reinforce the benefits by increasing the energy conversion efficiency of TPV. The report of an AB InGaAs TPV suggests a fundamental method to enhance the photon recycling rate by suppressing Fresnel reflection [1]. Using Au gridlines bonded to an Au surface by thermocompression cold welding, epitaxial III-V materials can be transferred to a desired substrate, where the air spacings are formed between the gridlines. The thin-film AB-TPV cell enables near-perfect photon utilization of around 99%, promising a high PCE.

The recent demands for miniaturization and portability of mobile devices have attracted the development of micro-power generators. Batteries are a traditional method, but chemistry-based electricity generation (< 0.5 kWh/kg) is limited much lower than hydrocarbon fuels (> 10 kWh/kg). During the last decades, researchers have developed micro solar cells [121,122], MEMS turbine engines [123,124], and μ-TPVs [61,64]. Among them, μ-TPVs are suitable for miniaturization, portable electronics, and wireless devices with less dependence on date, time, and location.

Chan *et al.* demonstrated a millimeter-scale TPV system involving a GaInAsSb diode (E_g = 0.547 eV). Due to the low efficiency of an emitter and the lack of a spectral filter, the PCE only reported 2.5% at T_h = 800℃ (view factor = 70%). Though the compact generator is still larger than > 1mm^2 and the efficiency is low, they predict a 32% PCE limit with power generation > 0.5 W/cm^2 and energy densities over 3 kWh/kg (energy densities of batteries are under 0.5 kWh/kg). Fontana *et al.* simulates a PCE limit of 43% at T_h = 1000 K with the consideration of system cooling, heat transfer coefficients, and the proximity (7.5mm) between an emitter and a cell. Still, there is a lack of demonstrating air-bridge μ-TPV cells, which is important to show the effect of an air-bridge for a high PCE.

Utilization of near-field radiation for TPVs is promising for high power density enabled by evanescent modes, exceeding the far-field blackbody radiation limit between planar surfaces [50,66-68]. Recently, an Au-BSR InGaAs-based TPV with a size of 0.06 mm^2 showed the near-field radiation effect with a high electrical output power density of 5 kW/m^2 using a mesa-patterned Si emitter with T_{emit} = 1270 K, where the close proximity between the PV and the heat source was 100 nm [66]. The electrical power density is higher than the air-bridged far-field TPV (3.2 kW/m^2 under T_{emit} = 1455 K). It records a relatively low efficiency of 7%, which is due to a huge parasitic

photon loss in OOB wavelengths. An air-bridge μ-TPV cell can help to reduce energy loss by suppressing the Fresnel loss. However, a severely buckled III-V membrane floating on the top of an air cavity disturbs the close proximity and limits the effect of near-field operation [1,65].

The thin-film membranes on air are easily strained and fragile due to the small fracture limits in inorganic materials (e.g., Si has a 1% limit) [65]. This restrains the demonstration of a thin-film AB-TPV membrane with an air cavity. As a result, designing a thin-film photodiode membrane with mechanical, optical, and electrical stability is critical for demonstrating the μ-TPV cell. In this chapter, we show the strategies to design an InGaAs thin-film photodiode for the AB-TPV cell: mitigate compressive buckling on InGaAs thin-film membranes; calculate practical spectral loss by FCA in doped III-V semiconductors; and simulate the electrical optimization of the InGaAs diode.

3.2 Design of an Air-Bridge InGaAs Thermophotovoltaic Cell

We design a thin-film InGaAs AB μ-TPV device with a cell size smaller than 200 μm. Figure 3.1(a) shows the cross-sectional schematic of an InGaAs/InP diode. A 3.2 to 3.4-μm-thick thin-film membrane suppresses compressive buckling [65]. Table 3.1 shows the calculation of the average R_{OOB} with different diode structures. The R_{OOB} is calculated by $R_{OOB} = \int_0^{E_g}\left(1 - A_c(E)\right)\times E\times\Phi(E)dE \Big/ \int_0^{E_g} E\times\Phi(E,T_h)dE$ where A_c is the cell absorption and the integration range was from 1.67 μm to 10 μm. Figure 3.1(b) plots the simulated absorption spectrum for the structures in Table 3.1. The air-cavity thickness is fixed to 0.6 μm and FCA was not considered. For cases 3 to 5, at the band-edge (0.74 eV), the cavity interference causes the high absorption and the drop of R_{OOB}. The Urbach tail can appear near the optical band-edge, which causes the loss of

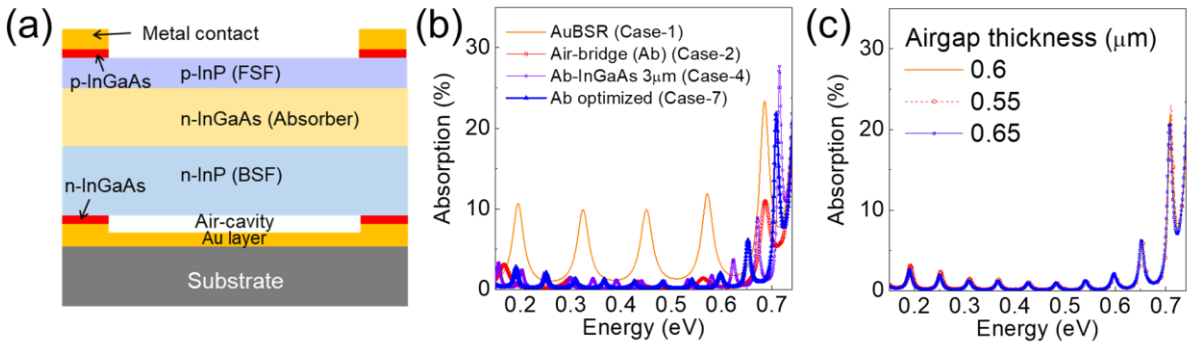

Figure 3.1 (a) InGaAs/InP thermophotovoltaic diode structure. The FSF and BSF mean the front-surface-field and back-surface-field, respectively. The InP (bandgap = 1.34 eV) layers are spectral windows. The InGaAs layers to the metal contacts form ohmic contact formation to metals. (b) Optics simulation to compare absorption spectrum with InGaAs/InP diode structures in Table 3.1. (c) Absorption spectrum for case 7 in Table 3.1 with different air-cavity thicknesses.

photons by the band-edge absorption as increasing the InGaAs absorber thickness [125,126]. Therefore, the absorber thickness should be between 1 to 2 μm. Cases 6 and 7 involve relatively thick InP layers, and the total R_{OOB} is almost the same as in case 2. Because of the InP bandgap (E_g = 1.344 eV) is larger than the InGaAs (E_g = 0.74 eV), the InP under the InGaAs absorber does not severely interfere with the absorption amount in the absorber [Figure A13 in Appendix A6]. We investigate resonant cavity effects (the free spectral range, $\Delta\lambda_{FSR}=\lambda^2/(n\times t_{air})$ where n is the refractive index) determined by the cavity depth (t_{air}). As shown in Table 3.1 and Fig. 3.1(c), the difference of the R_{OOB} is negligible at t_{air} = 0.55 to 0.65 μm. The p-type InP thickness can be varied from 0.2 to 0.4 μm, which mainly determines the series resistance (R_s) of the InGaAs TPV cell.

Next, we investigate the parasitic loss by FCA in the doped InGaAs and InP semiconductors [127-129]. Based on the Drude theory, the absorption due to FCA assumes the linear-dependence on carrier-concentrations and power-law dependence on wavelength [Appendix

A4]. We built the Drude model for InGaAs and InP materials. The extinction coefficient is expressed as a function of wavelength by:

$$\Delta k = \frac{1}{4\pi}(\lambda^{\gamma} \times C \times N), \tag{3.1}$$

where λ is the wavelength, γ and C are constants dependent on a given material, and N is carrier concentration. Figure 3.2(a) and (b) indicate the schematics for doped InGaAs and InP epitaxial layers with Au-BSR layers, where the layers were grown by MBE and transferred to Si substrates using Au-Au cold welding [65]. To find the Drude model parameters, the samples were characterized by FTIR measurements in Figs. 3.2 (c) and (d) for Figs. 3.2 (a) and (b), respectively. The solid and dashed lines indicate the simulations before and after applying the FCA model using the parameters in Table. 3.2. The symbols mean the measured FTIR data. The good agreements between the measurements and the simulations with the FCA model mean that the Drude theory can predict the parasitic loss of photons in OOB wavelengths. As a result, the loss of R_{OOB} by FCA is less than 1 %.

Table 3.1 Simulated out-of-band reflectance (R_{OOB}) with different diode structures [see Fig. 3.1(a)]. The incident angle is 15°. Cases 1 and 2 are the previous reported InGaAs thermophotovoltaic structures.

Case #	BSR type	Each layer thickness				t_{air} (μm)	R_{sub} (%)	Note
		Top InP	InGaAs	Bottom InP	Bottom InGaAs			
1	Au	0.2	1.0	0.1	0.1	No airgap	95.35	Ref. 38, 46
2	Air	0.2	1.0	0.1	0	0.6	98.54	Ref. 38
3		0.2	2.0	0.1			97.71	
4		0.2	3.0	0.1			96.11	
5		0.2	4.0	0.1			95.61	
6		1.5	1.0	1.5			98.37	
7		0.2	1.0	2.0			98.43	
						0.55	98.38	
						0.65	98.46	

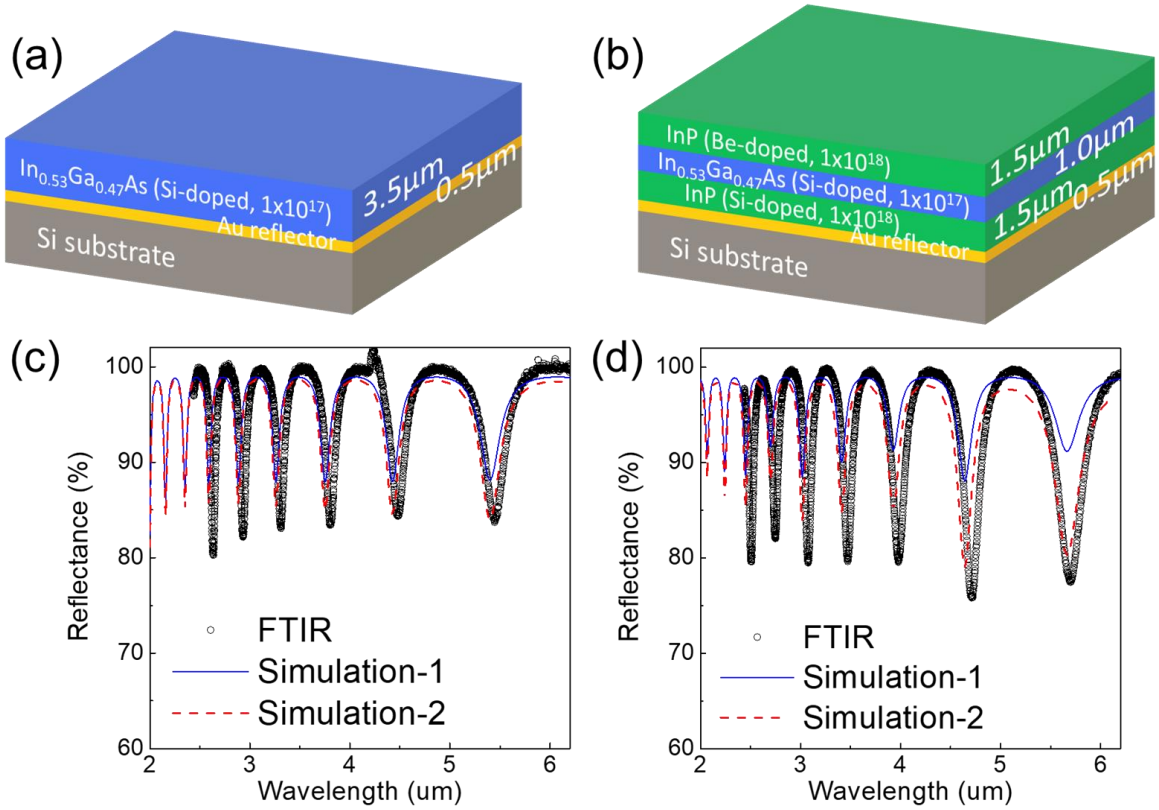

Figure 3.2 Schematics for the Drude model experiments of (a) the InGaAs and (b) the InP/InGaAs/InP thin-film structures with Au back-surface-reflector (BSR). (c) Fourier-transform-infrared (FTIR) measurement and simulations on the InGaAs 3.5 μm (N_c = 10^{17}/cm^3) / Au BSR. (d) FTIR measurement and simulations on the InP 1.5 μm (N_c = 10^{18}/cm^3) / InGaAs 1 μm (N_c = 10^{17}/cm^3) / InP 1.5 μm (N_c = 10^{18}/cm^3) / Au BSR. Simulation-1 does not involve the Drude model, otherwise Simulation-2 reflects the Drude model.

Figure 3.3(a) shows the InGaAs photodiode structure. To suppress a buckled membrane, the 2-μm-thick n-type InP layer is inserted below the n-InP BSF layer. The relatively low doping with 3×10^{16}/cm^3 (μ_h = ~4000 cm^2/V-s) reduces the FCA in infrared wavelength (>1.67 μm) corresponding to the sub-bandgap energy. Using the Drude model, the extinction coefficient (k) is below 0.001 in the wavelength range from 0.4 to 10 μm, meaning that the FCA in the layer is negligible. Figure 3.3(b) shows the energy band structure of the diode including metal-pad contacts, which was calculated using the Synopsys Sentaurus TCAD suite. The 2-μm-thick layer

can affect the R_s. Charge mobility is dependent on scattering and carrier concentrations. Therefore, we simulate and measure the n-type InP resistivity, respectively. The empirical model of doping dependent mobility is calculated using:

$$\mu\,(N_c) = \mu_{min} + \frac{\mu_{max} - \mu_{min}}{1 + \left(\frac{N_c}{N_r}\right)^{\alpha}} \qquad \text{at 300 K,} \tag{3.2}$$

where N_c is the carrier concentration, T is the temperature, μ_{min} is the saturation mobility at degenerate doping concentration, μ_{max} is the saturation mobility at low doping concentration under 10^{16} /cm^3, N_r is the doping concentration at which mobility reduces to half of the maximum at low doping, and α is the empirical fitting parameter [130].

Table 3.2 Drude model parameters for InGaAs and InP materials.

Material	γ	C
InGaAs	2.78	3.33×10^{-18}
InP	2.54	3.71×10^{-18}

Figure 3.3(c) plots the model for n-InP resistance as a function of doping level. The red-solid line is the R_s (26 mΩ/cm^2) of the previous air-bridge InGaAs TPV. The n-type InP bulk resistivity is exponentially increased as the N_c is decreased. In the doping range in $10^{16} \sim 10^{17}$ /cm^3, the resistivity of n-type InP is similar or higher than the metal contact resistivity to p-type InGaAs [131,132], but is much smaller than the R_s. Hence, the InP layer does not cause significant electrical degradation. Owing to relatively low hole mobility (< 200 cm^2-V^{-1}s^{-1}), a relatively thick p-type InP layer can increase the R_s. Furthermore, we note two important considerations. One is the back-surface-field (BSF) n-InP layer, which generates a high junction electric field at the interface of n-

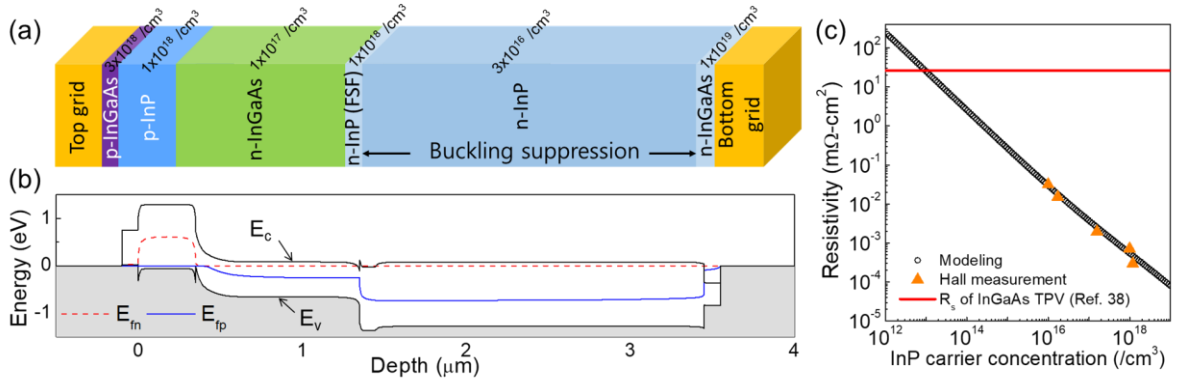

Figure 3.3 (a) Air-bridge InGaAs/InP diode structure (b) Band structure from the top to the bottom metal contacts. (c) Calculation of n-type InP resistance depending on the carrier concentration. The red solid line indicates 26 mΩ-cm^2, which is the series resistance of the previous air-bridge InGaAs TPV.

InGaAs/n-InP. The built-in high electric field supports the transport of majority free charges (electrons) to be collected at the cathode. Also, the BSF blocks minority carrier flow (holes in the n-type InGaAs absorber) to the cathode under illumination. Therefore, we keep the BSF layer with the thickness of 50 nm. Second, the intrinsic carrier concentration of the InP is calculated to be ~10^7 /cm^3 and the minimum doping level of InP by MBE is > 10^{15} /cm^3 at room temperature [133-135].

3.3 Fabrication, Method, and Visual Observation

The lattice-matched $In_{0.53}Ga_{0.47}As$/InP heterostructure is grown on a semi-insulating Zn-doped (100) InP wafer using the Veeco GENxplor MBE system with valved cracker sources for arsenic and phosphorus. Prior to the growth, the InP wafer is subjected to 250°C anneal for 1 hr under a pressure of 1×10^{-9} Torr to remove surface water vapor. Surface oxide desorption is performed in the growth chamber at 510°C for 15 min under phosphorus overpressure. The

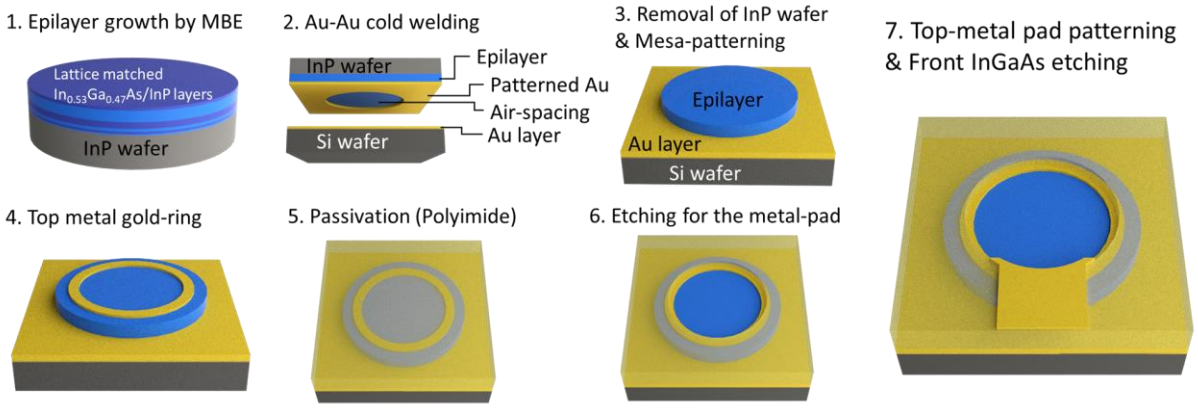

Figure 3.4 Schematic diagram illustrating the fabrication process flow for air-bridged thermophotovoltaics.

reflection high energy electron diffraction (RHEED) pattern shows (2×4) surface reconstruction, indicating a cleaned (100) InP surface. After the de-oxidation, epitaxial growth takes place at 490°C using group-III and -V sources. A schematic diagram showing the complete process flow for fabricating the air-bridge TPV is presented in Fig. 3.4. The Au-gridlines are patterned on the epilayer using a standard lift-off process. The epilayer with Au-grids is transferred to a silicon substrate by Au-Au cold welding, where the spacing between grids forms air spacing. Before starting the bonding process, the chamber is evacuated by ~1 Torr to reduce the internal air pressure. Circular-mesa shapes are patterned by etching the epilayer using CH_4/H_2 (ratio of 1 to 4) reactive-ion-etching (RIE) method. The top metal ring is defined by Pt (90 nm)/Ti (150 nm)/Pt (150 nm)/Au (2000 nm) using thermal-evaporation and lift-off processing. The sample is then passivated by using polyimide (DuPont PI-2555) and cured at 100°C for 10 min and at 200°C for 1 hr, consecutively. The metal pad area is defined by O_2 plasma dry-etching. The pad of Ti (100 nm)/Au (2000 nm) is patterned by conventional lift-off and thermal evaporation methods. Finally, the top 100-nm InGaAs contact layer is wet-etched using H_2O_2:H_2PO_4:DI=1:1:8 for 20 s.

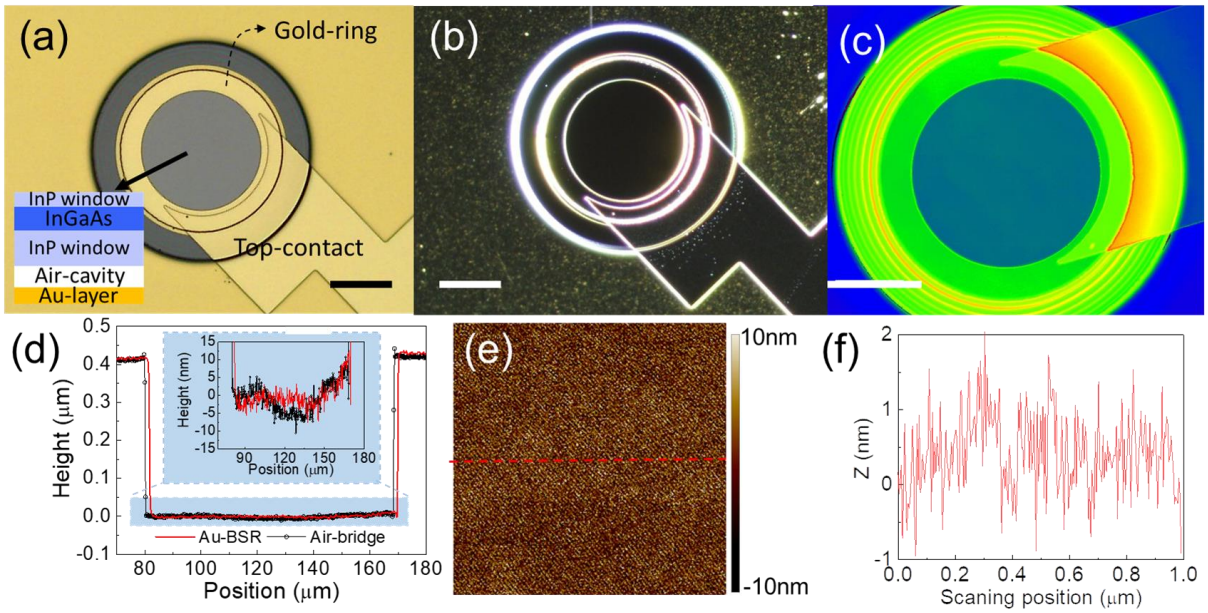

Figure 3.5 Observation of the air-bridged InGaAs-TPV. (a) Bright-field optical microscopy image. The inset illustrates the air-bridge TPV structure. Scale bar, 50 μm. (b) Dark-field optical microscopy image. Scale bar, 50 μm. (c) Laser-confocal-microscopy image. Scale bar, 50 μm. (d) Surface-profilometry measurements from the air-bridge TPV and an Au-BSR TPV. The inset indicates the extended graph at the blue-filled box region. (e) Atomic-force-microscopy (AFM) image measured at the center of the PV surface. (f) Surface roughness profiles at the red-dot crossline in (e).

Figure 3.5(a) is the optical microscope image for an InGaAs AB-TPV device with a 90-μm-diameter air cavity. The device is inspected by a dark-field microscope in Fig. 3.5(b), verifying no particles at the surface. Figure 3.5(c) indicates the observed laser-confocal-microscopy (LEXT OLS4000, Olympus), showing clean and uniform colors on the membrane. This means the particle free and flat morphology. In Fig. 3.5(d), the surface profilometry measurements also reveal the flat membrane compared to the Au-BSR TPV structure. The measurement resolution is 10 nm. Figure 3.5(e) shows the surface roughness measured by using an atomic-force-microscopy (AFM) (Bruker ICON AFM, Bruker-AXS). Three height parameters are considered for quantitative evaluation and surface roughness normalization including mean

roughness (R_a), root-mean-square roughness (R_q), and peak-to-peak roughness ($R_{p\text{-}p}$) resulting in 3.14 nm, 3.97 nm, and 2.99 nm, respectively, resulting in normal roughness observed in solid materials [136-138].

3.4 Results and Discussion

Figure 3.6(a) shows the measured current-density versus voltage (*J-V*) characteristics of an InGaAs AB-TPV cell in the dark. The recombination losses in the space-charge-region (SCR) are evaluated by the ideality factor from the *J-V*. The forward-bias region is fitted with the two-parallel current transports using the two-diode equation following by [139,140]:

$$J_D = J_1\left[\exp^{\frac{q(V-R_sJ_D)}{n_1kT}} - 1\right] + J_2\left[\exp^{\frac{q(V-R_sJ_D)}{n_2kT}} - 1\right] + \frac{V-R_sJ_D}{R_{\text{sh}}} \tag{3.3}$$

where J_1 and J_2 are the saturation current-densities in the quasi-neutral-region (QNR) and the space-charge-region (SCR), respectively. The first term corresponds to the diffusion current flowing across the *p-n* junction and the second term indicates the generation-recombination current ($J_{G\text{-}R}$) by the imperfect junction at the SCR. The R_s and R_{sh} indicate the series resistance and the shunt resistance, respectively. The n_1 and n_2 are the ideality factors. The TPV cell is mounted on a customized water-chiller stage, regulating the cell temperature at T = 20°C. In Table 3.3, the ideality factor in the QNR is close to 1, meaning that the band-to-band recombination is dominant. The ideality factor by the $J_{G\text{-}R}$ is $n_2 < 2$, which is critical to determine the R_{sh} near zero-bias and the loss of V_{oc} by photovoltaic effect. Figure 3.6(b) shows an MBE operation diagram during the transition from the p-type InP to the n-type InGaAs growths. At the transition, the arsenic (As) soak time at the InP interface is important to prevent arsenide diffusion and incorporation into the InP layer. Too long of a soak time causes the desorption of P and generates Ga-P bonding – thereby

producing In-Ga-As-P, where the abrupt InP/InGaAs band structure is not correctly formed [141,142]. We use the same growth temperatures (490°C) for InGaAs and InP layers, intending the short transition time, and the soak time is fixed at 3 sec.

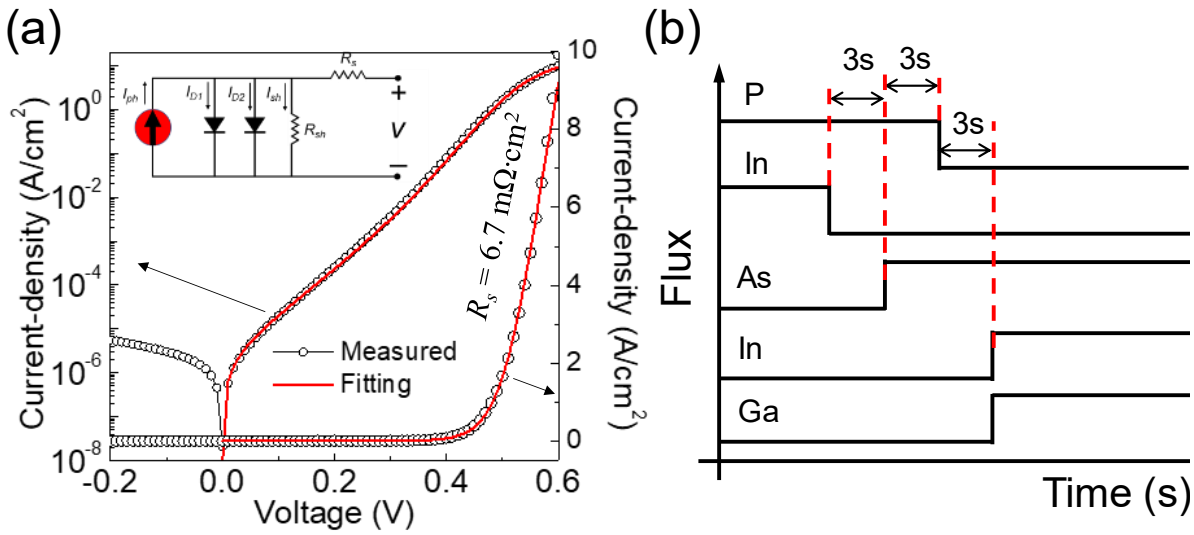

Figure 3.6 (a) Current-voltage (J-V) characteristics under dark. The inset indicates the circuit diagram of the two-diode model including the series (R_s) and shunt resistances (R_{sh}). (b) MBE growth diagram for the InP/InGaAs heterostructure interface.

Table 3.3 Fitting parameters for the double-diode model of the air-bridge InGaAs thermophotovoltaic cell.

J_1 (nA/cm^2)	J_2 (μA/cm^2)	R_s (mΩ-cm^2)	R_{sh} (kΩ-cm^2)	n_1	n_2
10.2	1.9	6.4	100	1.03	1.65

Figure 3.7(a) shows the *J-V* characteristics of the InGaAs TPV cell under illumination using a SiC globar emitter. The measurement set-up is illustrated in the previous work [1]. The J_{sc} and V_{oc} are controlled by changing the emitter temperature as shown in Table 3.4. The relationship between the J_{sc} and the geometrical *VF* is determined by:

$$J_{sc}=q\times VF\times \int_{E_g}^{\infty} \varepsilon_e(E) \Big/ A_{cell}(E) \times EQE(E)\times P(E)dE \qquad (3.4)$$

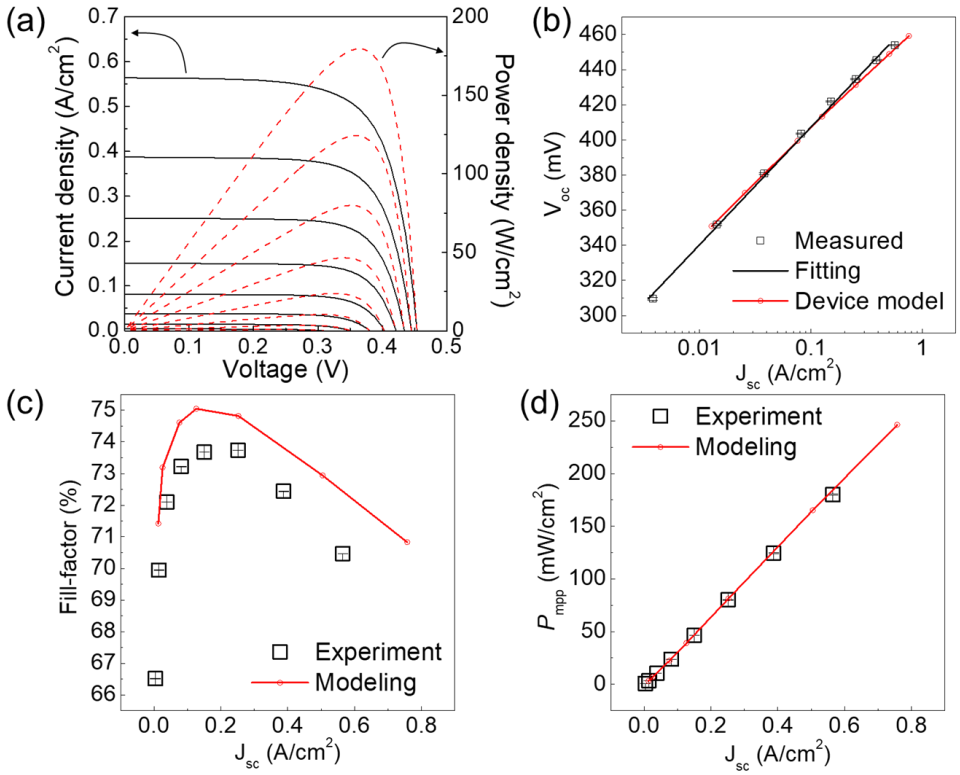

Figure 3.7 (a) Current-voltage (*J-V*) characteristics under far-field emission spectrum using a SiC globar with different temperatures. The left-axis means the measured current-density. The right-axis indicates the power-density. (b) Plot of the measured J_{sc} and V_{oc}. (c) Fill-factor and (d) max-power-density via different emitter temperatures. The error-bar indicates the standard deviation.

where ε_e is the effective emissivity (equation (1.4)), q is the electric charge, *EQE* is the external-quantum-efficiency, and P is the spectral photon flux [89]. During the measurement, the far-field operation was performed at the same geometrical configuration between the TPV cell and the emitter, and the *VF* is approximately 0.07. In. Fig. 3.7(c), the ideality factor from the *J-V* is extracted from the extrapolated fitting using the equation:

$$\frac{q}{nkT}(V_{oc2} - V_{oc1}) = ln\left(\frac{J_{ph2}}{J_{ph1}}\right) \tag{3.5}$$

where $J_{ph2} > J_{ph1}$, $V_{oc2} > V_{oc1}$, and $n = 1.12$. Figure 3.7(d) shows the *FF* and the P_{mpp} as a function of J_{sc}. The *FF* is decreased as J_{sc} is increased higher than 0.3 A/cm^3 ($V_{oc} > 0.43$ V) owing to ohmic losses. We numerically perform the device modeling using a TCAD suite (Sentaurus, Synopsys) [143,144] (see the details in Appendix A3). In Figs. 3.7 (b) to (d), the simulated parameters are similar to the experiments. From the TCAD method, the SRH lifetimes for InGaAs and InP are 10 μs and 20 ns, respectively, meaning that the charge lifetime is determined by radiative recombination. The recombination velocity at the p-n junction is found to be 10^3 cm-s^{-1}. The measured *FF* is 67 – 74%. We note that the *FF* and V_{oc} can be improved by a larger mesa-size or lower charge recombination at the p-n junction [140,145].

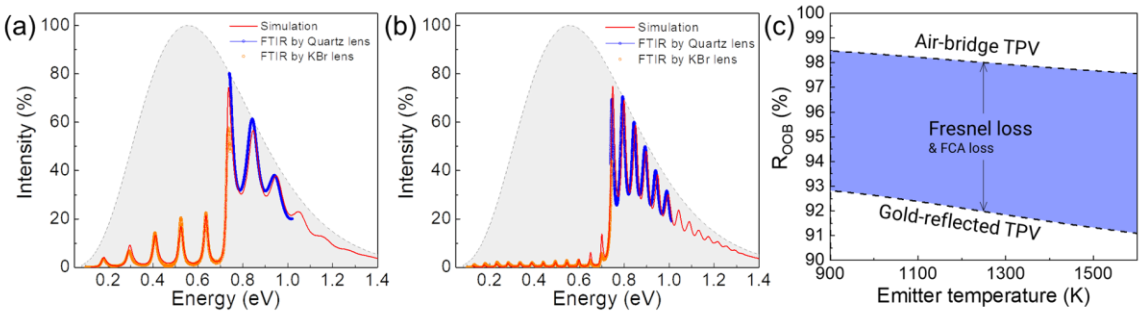

Figure 3.8 Fourier-transform-infrared (FTIR) characterizations for InGaAs (a) Au-BSR TPV and (b) AB-TPV cells. Dashed lines indicate 1300 K blackbody spectrum with the normalized power (%), the red solid lines are simulated absorption (%), and the blue-circle-solid and red-circles are measured FTIR data. (c) Calculated R_{OOB} as a function of emitter temperatures.

Figure 3.8 compares the FTIR measurements and simulations for Au-BSR and AB-TPV cells. The simulations were calculated using the Drude model in Table 3.2. The free spectral ranges (FSR) are different between the two cells due to the different thin-film structures, deciding Fabry-Perot interference. In the below bandgap energies (< 0.74 eV), the absorption of the Au-BSR sample is higher than the air-bridge sample because the air reduces the photon loss by Fresnel

reflection at the back surface of the TPV membrane. Additionally, the air-bridge structure mitigates the total parasitic loss by FCA by removing the bottom n^+-InGaAs contact layer, as illustrated by the schematic in Fig 3.5(a).

Table 3.4 Electrical parameters for the measured current-density versus voltage under different emitter temperatures.

T_{emit}	V_{oc} (mV)	J_{sc} (mA/cm^2)	FF (%)	P_{mpp} (mW/cm^2)	PCE (%)
914	309.52±0.81	3.81±0.02	66.5±0.4	0.784±0.003	16.74±0.01
987	351.71±0.61	14.27±0.12	69.9±0.4	3.511±0.005	21.42±0.01
1060	380.85±0.42	37.95±0.05	72.1±0.2	10.421±0.033	24.80±0.02
1133	403.49±0.38	81.28±0.07	73.2±0.2	24.014±0.103	27.21±0.05
1206	421.82±0.4	150.67±0.1	73.7±0.1	46.828±0.149	28.91±0.05
1279	434.54±0.29	251.11±0.12	73.7±0.1	80.459±0.215	29.95±0.06
1352	445.38±0.22	387.49±0.24	72.4±0.1	125.012±0.328	30.20±0.07
1425	453.98±0.24	565±0.72	70.5±0.1	180.746±0.445	29.94±0.08

Table 3.5 Bandgap, physical parameters, and effective density of states for InGaAs and InP.

	$In_{0.53}Ga_{0.47}As$	InP
Bandgap, E_g (eV)	0.74	1.344
Electron affinity, χ (eV)	4.5	4.38
m_e^*/m_0	0.041	0.08
m_h^*/m_0	0.2	0.6
N_c (cm^{-3})	2.1×10^{17}	5.7×10^{17}
N_v (cm^{-3})	7.7×10^{18}	1.1×10^{19}
n_i (cm^{-3})	6.3×10^{11}	1.3×10^{7}

The OOB reflectance, R_{OOB}, is calculated using the equation [1,51,55]:

$$R_{OOB} = \frac{\int_0^{E_g}[1-A(E)]\times P(E,T_E)dE}{\int_0^{E_g}P(E,T_E)dE}, \tag{3.4}$$

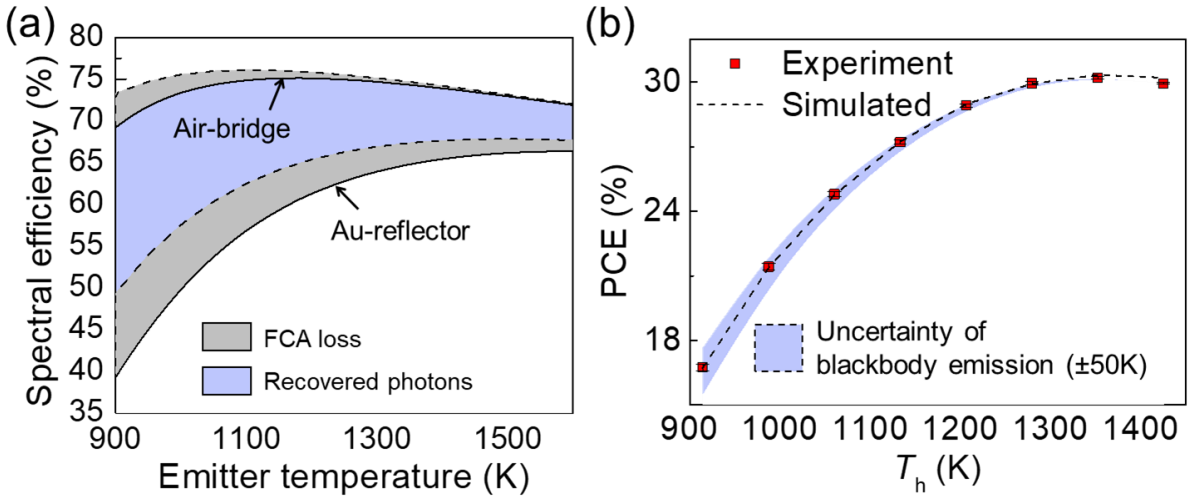

Figure 3.9 (a) Spectral efficiencies (SE) of the Au-BSR and the air-bridge InGaAs TPV cells versus emitter temperatures. The bandgap of InGaAs is 0.74 eV. The orange-colored region means the FCA loss in the air-bridge TPV. The black-colored region means the FCA loss in the Au-BSR TPV. Using the Drude-model, the FCA loss is experimentally calculated. The SE curves involving the FCA effect use the same data plotted in Fig. 3.8. (b) Power-conversion-efficiency (PCE) of the air-bridge cell under different SiC emitter temperatures. The rectangles are measured data and the dashed line means the simulation data. The shaded area reflects the uncertainty of the emitter temperature (±50K).

where $A(E)$ is the cell absorption and $P(E)$ is the power density spectrum at a given emitter temperature, T_E. The R_{OOB} of for the AB-TPV cell is higher than the Au-BSR TPV cell. Compared to the Au-BSR PV cell, the air-bridge device represents a four-fold reduction of the absorption in the OOB wavelengths. The diode structure has the doped InP layers ($N_c = 10^{18}$ /cm^3), which causes a loss of R_{OOB}, less than 1 %. Table 3.5 provides the effective density of states at the conduction (N_c) and the valence band (N_v) for the InGaAs and InP, respectively. Additional small loss can be produced due to doping calibration and defects in the p-type InP. The formation of ohmic-contact to InP is difficult as the valence band maximum is formed at a relatively deep energy level of ~5.7 eV, disturbing ohmic-contacts to metals [146,147]. Fast dopant diffusion during MBE growth leaves vacancy-related defects near the valence band, which affects the ability to regulate precise

carrier concentrations [148,149]. However, the thickness of the p-type InP is not significantly thick, meaning that the loss can be negligible.

The enhanced power reflectance in the below bandgap leads to the improvement of spectral selectivity. Figure 3.9(a) shows the SE of the Au-BSR and the AB-TPV cells. The solid lines indicate the simulations after involving the FCA, as used in Fig. 3.8. The TPV efficiency is calculated by

$$PCE_{TPV} = \frac{P_{out}}{P_{in} - P_{ref}} = \frac{P_{out}}{P_{abs}} = \frac{FF \times J_{sc} \times V_{oc}}{qA \times \mathrm{VF} \times \int_0^\infty A_{eff}(E) P(E, T_h) dE}, \quad (3.5)$$

where the denominator term is determined by a heat source power and total reflectance. Figure 3.9(b) shows the PCE calculation as a function of emitter temperatures. The SiC emitter has an error range of the measured temperature about ±50 K. At T_{emit} = 1352 K, the PCE is estimated by 30.3%.

In conclusion, we introduce a non-buckled TPV membrane spanning Au gridlines, where the TPV size is 0.02 mm^2. The 2-μm n-InP buffer layer suppresses the buckled morphology, resulting in a perfectly flat membrane compared to the Au-BSR TPV structure. The photodiode involves a high-doped n-InP BSF thin film, helping hole charge collection and electron charge transport. The demonstration shows R_{OOB} = 97.6 % where the losses of ΔR_{OOB} = 0.8 % and 1.6 % due to FCA and cavity oscillations, respectively. Under far-field radiation (T_h = 1352 K), the device shows the PCE of 30.3 % at V_{oc} = 0.45 V, J_{sc} = 0.39 A/cm^2, and FF = 72.44 %. Although we only proved a photodiode structure for the non-buckled TPV membrane, the strategies (for mechanical stability, high quantum efficiency, and high R_{OOB}) can be universally applicable to other materials.

Chapter 4 Multi-Air-Bridge Tandem Thermophotovoltaic Architecture

4.1 Introduction

A high-efficiency TPV system is a key factor in thermal management and cost reduction, enabling it to drive commercial TPV markets, particularly in industries that can recycle the waste heat into electrical energy [6,150,151]. Simply, the efficiency can be improved by exceeding the SQ limit of single-junction cells through several methods such as near-field radiative heat transfer [50,66,152], spectral tuning approaches using metamaterials [153,154], infrared back-surface-reflectors (BSR) [1,2,54], and multi-junction structures [70,155-157]. Among them, multi-junction PV structures suggest a fundamental method to achieve high efficiency by improving spectral efficiency and increasing the electrical output power [158,159]. Conventional tandem PVs have two important factors for high performance: one is material partners with different bandgaps, and the others are tunnel junctions and lattice-matched epilayer growth techniques [160-163]. The III-V epitaxial growth technique is essential for multi-junction cells with a wide range of bandgaps, but owing to the unique lattice constants of materials, they have fewer tandem alloying partners, limiting the combination of different bandgaps.

Recent tandem PV technologies have suggested solutions to mitigate the challenge. They demonstrated Si/III-V tandem solar cells with a higher efficiency than 30% (A Si single-junction solar cell is limited to 24 % efficiency) [161,163]. These address advanced tandem architectures to combine two heterogeneous materials (e.g., silicon and III-V materials) by means of mechanical

stacking [161,164] or direct bonding [163,165]. However, they have some disadvantages, that limit the application to TPV tandem architectures. Heavy-doped tunnel junctions (TJs) result in photon loss by free carriers at sub-bandgap wavelengths. Overall, the TJs cause a reduction of R_{OOB}, SE, and TPV efficiency. Furthermore, the complicated fabrication process is not economic for commercial modules.

In this chapter, we propose a novel tandem structure involving multi-air-cavity layers, which paves the way for selecting different bandgap materials without regard to lattice-matching for multi-junction cells. The concept is to connect independent sub-cells by mechanical bonding methods [160,166,167]. Unlike the previous methods using semiconductor-semiconductor bonding, it has several benefits. One is that it does not need high-doped ($>10^{19}$ /cm^3) TJs for electrical connections between sub-cells, implying that the absorption of sub-bandgap photons by free carriers can be reduced. Furthermore, the epitaxial growth between the sub-cells is not required, meaning that the liberty to choose tandem partners is extended. Double air bridges are built in at the bottom of each sub-cell, opening the path for sub-bandgap photons to return to the heat source.

To validate the potential of the concept, we demonstrate a 2-terminal tandem TPV cell, characterized by using a hot SiC globar emitter. The tandem structure has two air-bridge layers, which are examined by scanning-electron-microscopy (SEM) and FTIR methods. In the demonstration, the sub-cells have the InGaAs (In:Ga=0.53:0.47) absorbers. We confirm the effect of the multi-junctions by observing V_{oc} operation nearly two times higher than a single InGaAs cell. As the structure does not contain heavy doped layers, it suppresses the R_{OOB} loss by FCA. In the TPV system, the spectral efficiency depends on emitter temperatures. Hence, the current-matched condition varies as a function of emitter temperatures. To mitigate the efficiency

dependence on the current matched conditions, the conceptual tandem architecture allows three or four terminals by inserting an insulating layer between the sub-cells.

4.2 Tandem Photovoltaic Structure with Double Air-Bridge Layers

4.2.1 Fabrication

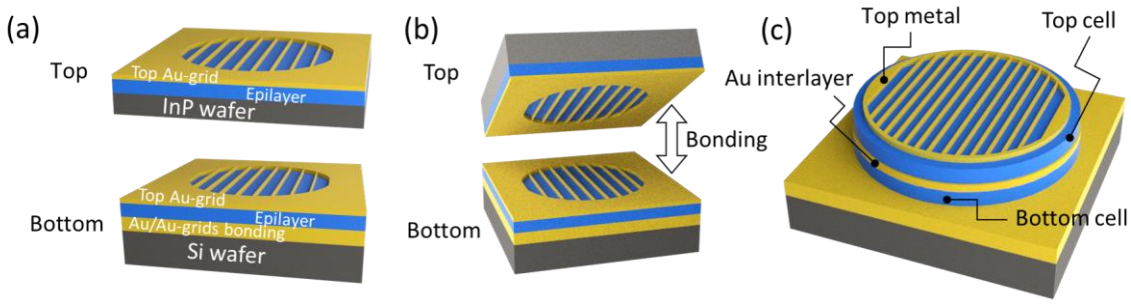

Figure 4.1 Schematic diagram illustrating the fabrication process flow for tandem photovoltaics. (a) The bottom and top subcells are independently prepared. The air-bridge bottom cell fabrication follows the same sequence as depicted in the previous report [1]. (b) The Au gridlines at the two cells are optically aligned and joined using a flip-chip bonding technique. (c) After patterning the circular-mesa structure and the top metal, the tandem structure is formed with the Au-Au interlayer.

Figure 4.1 illustrates the fabrication process flow for an InGaAs homo-tandem TPV cell. The InGaAs/InP heterostructure on an InP wafer is prepared by molecular-beam-epitaxy (MBE), where the InGaAs (In:Ga=0.53:0.47) is lattice-matched to InP. The air-bridge single cell for the bottom TPV is independently prepared following the same methods as previously [1]. The Pt/Ti/Pt/Au (9/15/15/200nm) gridlines at the individual bottom and top cells are patterned by thermal evaporation and lift-off processes. Au-Au cold-welding is performed by two different steps. First, the Au gridlines are aligned using an optical instrument (Flip Chip Bonder, Finetech GmbH & Co. KG, Berlin, Germany) and the two cells are bonded using 200 N (tool-limit) force

at 150 °C for 10 min. The softly bonded sample is moved to another bonding chamber (EVG 520, EV Group, Austria) and the second bonding process is applied using 1 kN force at 150 °C for 10 min. The InP wafer is chemically removed by dilute HCl ($HCl:H_2O$ = 1:1) etchant for 16 hrs. The circular-mesa shape is patterned by wet-etching in $H_2PO_4:H_2O_2:H_2O$ = 1:1:8 for InGaAs and $HCl:H_2O$ = 1:1 for InP. The top-metal contacts are defined by Pt/Ti/Pt/Au (9/15/15/200nm) by thermal-evaporation and lift-off processes.

4.2.2 Method

Current-Voltage Characterization

The current-density versus voltage (*J-V*) properties of the InGaAs tandem PV cell are characterized using a Keithley 2401 Source-Measurement-Unit in the 4-wire sensing mode to minimize the lead and contact resistance effects during the measurement. The sample is mounted on a customized water-cooled stage and the temperature is set to 20°C during the measurement. The PV effect is measured under the far-field radiation using a SiC globar emitter. The measured *J-V* is by the diode equation and a numerical simulator (Synopsys Sentaurus TCAD suite). The TCAD method calculates the charge-carrier distribution and transport by solving the Poisson, electron and hole charge continuity, and drift-diffusion equations. The SRH model is included to account for non-radiative recombination. Light propagation is calculated using the built-in the transfer matrix method (TMM) in the TCAD suite. The Drude model is used to consider FCA.

Optics Simulation and Measurement

The TMM method calculates light propagation through the layered media under black-body spectra at different temperatures. The FTIR spectroscopy system (Cary 670 FTIR spectrometer

and Cary 620 microscope, Agilent Technologies) is used to measure the reflection characteristics of the TPV cell. The measurement is performed using a liquid-nitrogen cooled environment and the light incidence angle is 5 to 25° (average 15°).

Finite-Element-Analysis Simulation

To predict the mechanical stability during the bonding process between the top and bottom cells, we perform the FEA simulations (COMSOL v5.6) for two different bonding structures – parallel or cross-aligned Au gridlines between the cells. A physics option in COMSOL (Solid Mechanics) is used to calculate the structural deformation of the thin-film membranes floating on air bridges. To simulate the dislocations by residual stress after the bonding process, we assume that the compressive Au deformation is caused by the bonding force. The internal pressure in the cavity is set to 0.1 MPa (equivalent to the chamber pressure during the bonding process). The internal pressure can be determined by the amount of Au deformation and air-spacing volume, dependent on different bonding structures. However, this is not large based on our previous study [65]. Therefore, we do not change the pressure to compare two different Au-gridline bonding structures.

4.3 Demonstration of an Air-Bridge InGaAs Tandem Thermophotovoltaic Cell

4.3.1 Two-terminal Air-Bridge InGaAs Tandem Photovoltaic Cell

Figure 4.2 (a) illustrates the cross-section of the InGaAs tandem cell. The air-bridge between the sub-cells is a transparent window, resulting in spectral splitting without a heavy-doped TJ layer. Therefore, it can mitigate photon loss due to FCA in OOB wavelengths. Figure 4.2 (b) shows the optical microscope image of the tandem cell, where the cell size is a 1.5-mm-diameter and the top metals have the 100-μm-spacing between Au-grids. Figure 4.2 (c) is the surface

profilometry measurement by scanning the black dashed line in Fig. 4.2 (b). The membranes has buckled morphology with the height of 10 – 30nm. Figure 4.2 (d) is the cross-sectional SEM image of the sample. Figure 4.2 (e) is the extended image indicated by the white box in Fig. 4.2 (d). The

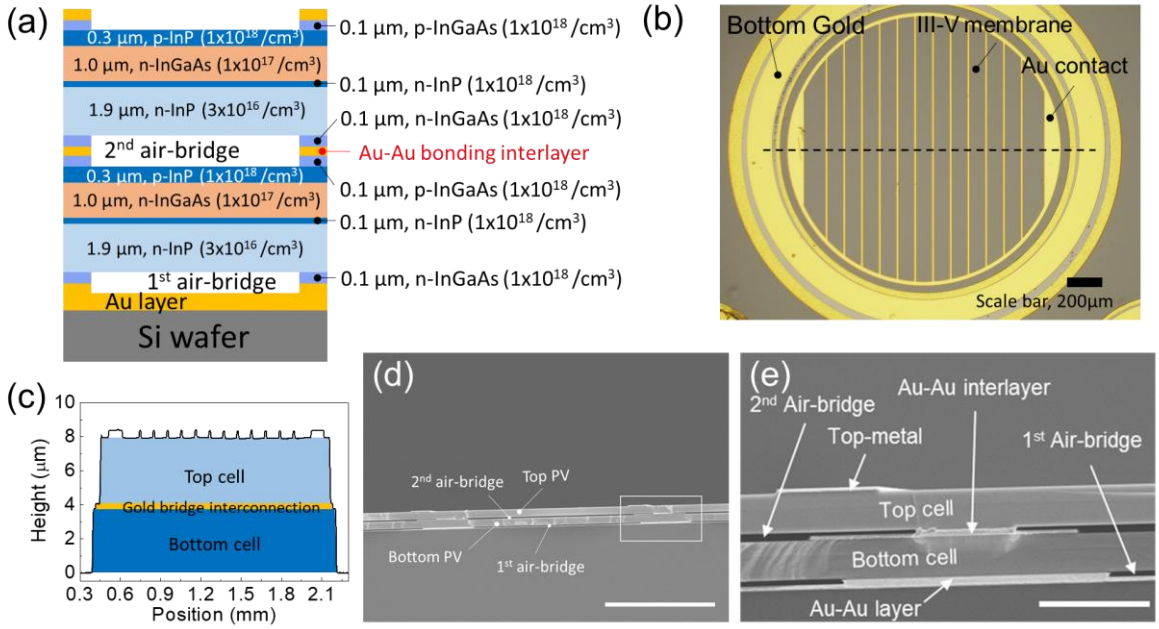

Figure 4.2 (a) Schematic of the double air-bridge tandem cell. The numbers in parentheses indicate the concentrations of the corresponding thin film. (b) Optical microscopy observation of the two-terminal InGaAs tandem cell. (c) Measured profilometry through the dashed-black-line in (b). (d) Cross-sectional scanning electron microscope (SEM) image of the double air-bridge tandem cell. Scale bar, 50µm. (e) High-magnification image indicated by the white box in (d). Scale bar, 10µm.

Au gridlines at the top and bottom cells are aligned and bonded using the optical instrument (see the Method section, 4.2.2). The misalignment tolerance is 5 µm and the gridline widths are 7 and 20 µm for the top and bottom cells, respectively.

4.3.2 Optimization of the Bonding Structure Between Au-Gridlines

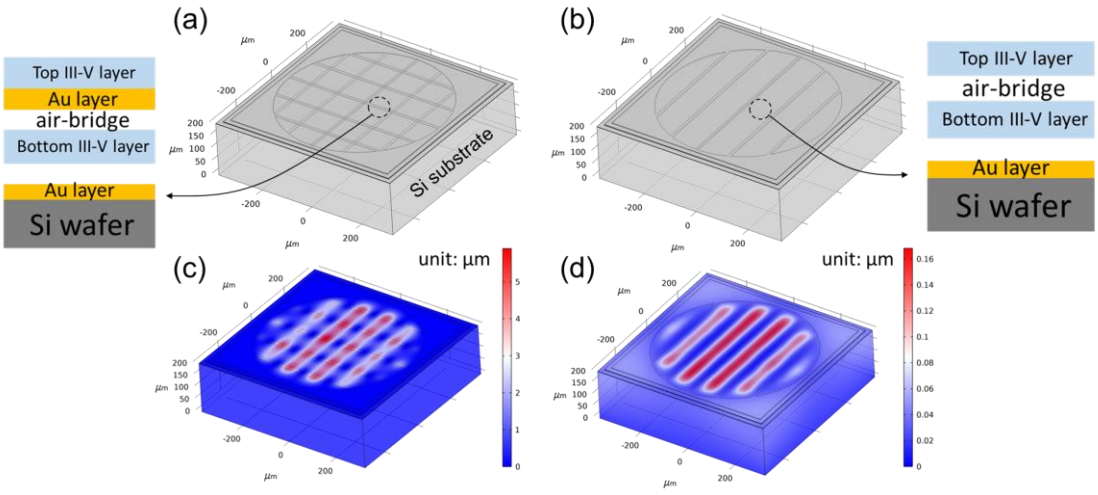

Figure 4.3 Finite-element-analysis (FEA) simulation structures of (a) the cross-aligned and (b) parallel-aligned Au-gridlines for the bonding between the bottom and top cells. The view-mode is the transparency mode. FEA simulation results for the total displacements of (c) the cross-aligned and (d) the parallel-aligned tandem structures. The color labels indicate the total displacements in the structures.

Figures 4.3 (a) and (b) show the FEA simulation models (COMSOL Multiphysics) for cross and parallel-aligned Au-gridlines, respectively, for cold welding. In the software, the view is in transparent mode, generating a circular window at the top to visualize the gridline structures. Figure 4.3 (b) requires a strict rule for alignment between Au-gridlines parallelly, meaning that the cross-aligned design can be feasible for an easier bonding process. However, the geometrical fill factor (GFF: ratio of an air bridge area to a cell area) of the cross-aligned design is smaller than the parallel-aligned design. We calculate the GFF of the air-bridges for each case as 82.6 % (cross-aligned) and 90.9 % (parallel-aligned), respectively, where the Au-gridline width and the air-bridge spacing are assumed as 8 µm and 80 µm, respectively.

Furthermore, mechanical instability is calculated by FEA simulations. Figure 4.3 (c) and (d) show the total displacements for the cross- and parallel-aligned structures, respectively. The boundary conditions are determined by three factors: compressed Au grid deformation (10 N in z-

axis) and the bottom displacement at z = 0. The internal air pressure was assumed to be atmospheric pressure (0.1 MPa). The cross-aligned design has larger displacements compared to the parallel-aligned design. The black-dot circles in Fig. 4.3 (a) and (b) indicate the most mechanically fragile regions by means of compression bonding force. The top cell with the cross-aligned Au-grids has a thin-film membrane with III-V epilayer/Au. Owing to the low hardness of Au (in Chapter 2), the total displacement of the stack follows the Au deformation, resulting in a large plastic deformation [65]. Thus, the parallel-aligned design is promising to demonstrate a multi-air-bridge thin-film tandem cell.

4.3.3 Characterization of an Air-Bridge InGaAs Tandem Thermophotovoltaic Cell

Figure 4.4 (a) shows the measured *J-V* characteristics of the air-bridge InGaAs single and tandem TPV cells under illumination using a SiC globar emitter. The emitter temperatures were varied in a range of 1100 – 1600 K. In Fig. 4.4 (b), the V_{oc} of the tandem cell is approximately two times higher than the V_{oc} of the single cell, implying the two-terminal tandem configuration with two junctions. The sub-cells were not current matched and the spectral splitting between the same bandgap sub-cells was not optimized. Thus, the electrical losses owing to the imperfect tandem structure resulted in a lower power density than the single cell, as calculated in Fig. 4.4 (d).

Figure 4.5 (a) shows the FTIR measurement, representing that the R_{OOB} is 96.3 % with the losses of 0.7 % and 1.8 % by band-edge absorption and FCA, respectively. Additional R_{OOB} loss was about 1.6 %, which was occurred by the cavity oscillations. The red solid line is the simulation using the TMM, where the Drude model calculates the FCA in the doped semiconductors. Figure 4.5 (b) is the SE as a function of emitter temperatures. The FCA significantly drops the SE at a

relatively low temperature. The PCE is optimized in the grey box, where the SE difference is less than 2 %. It implies that the FCA only generates a small reduction of the PCE.

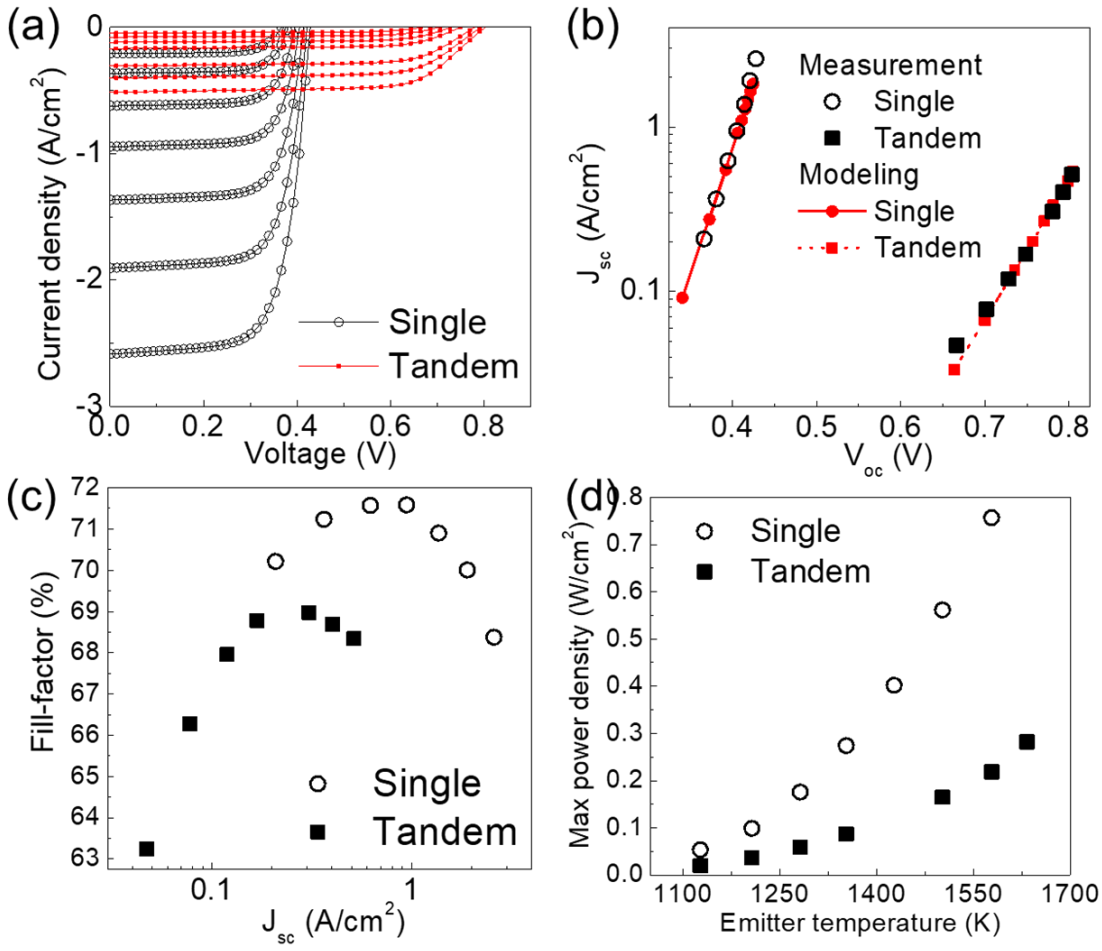

Figure 4.4 (a) Characterization of the current-density versus voltage under heat emission using a SiC globar emitter of the air-bridge InGaAs single and homo-tandem photovoltaic (PV) cells, respectively. (b) Short-circuit current density (J_{sc}) versus open-circuit voltage (V_{oc}) of the single and tandem PVs. (c) Fill-factor (FF) and (d) Max-power-density versus emitter temperatures, respectively.

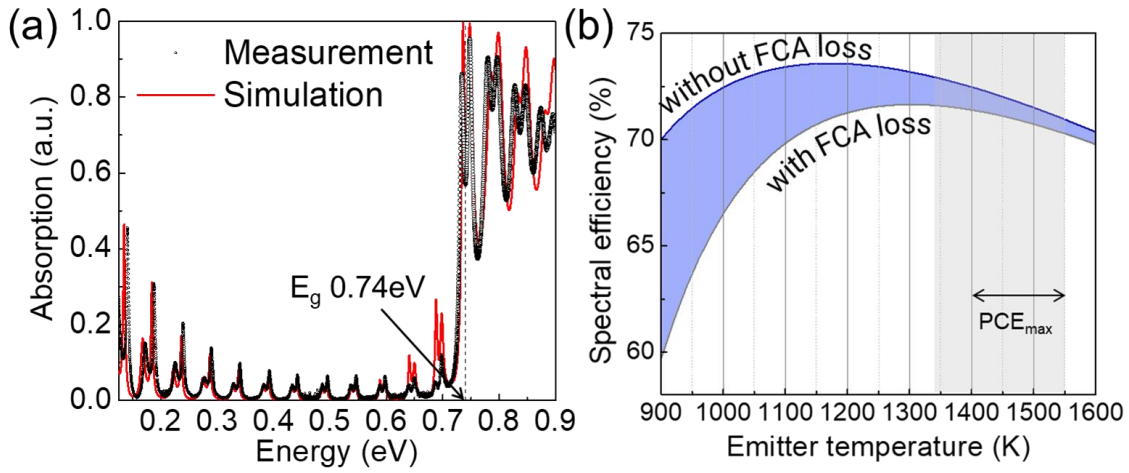

Figure 4.5 (a) Fourier-transform-infrared (FTIR) measurement using the InGaAs tandem cell. Quartz and the kBr (Potassium Bromide) lenses are used to scan the energy of 0.35~1.0 eV and 0.2~0.74 eV, respectively. (b) Spectral efficiency with or without FCA. The grey box is the emitter temperature range for PCE_{max}.

Table 4.1 Electrical parameters for the measured current-density versus voltage of the air-bridge InGaAs single and tandem cells.

T_{emit}	V_{oc} (mV)		J_{sc} (mA/cm^2)		FF (%)		P_{mpp} (mW/cm^2)	
	Single	Tandem	Single	Tandem	Single	Tandem	Single	Tandem
1127	0.366	0.666	-0.21	-0.05	70.2	63.2	54	20
1207	0.381	0.702	-0.36	-0.08	71.2	66.3	99	36
1282	0.395	0.728	-0.62	-0.12	71.6	68.0	176	59
1353	0.405	0.748	-0.94	-0.17	71.6	68.8	274	87
1427	0.414	-	-1.37	-	70.9	-	402	-
1502	0.421	0.780	-1.91	-0.31	70.0	69.0	562	165
1578	0.428	0.793	-2.59	-0.40	68.4	68.7	757	219
1633	-	0.803		-0.51	-	68.3	-	282

4.3.4 Details of Current-matching Condition for InGaAs/InP Heterostructure Diode

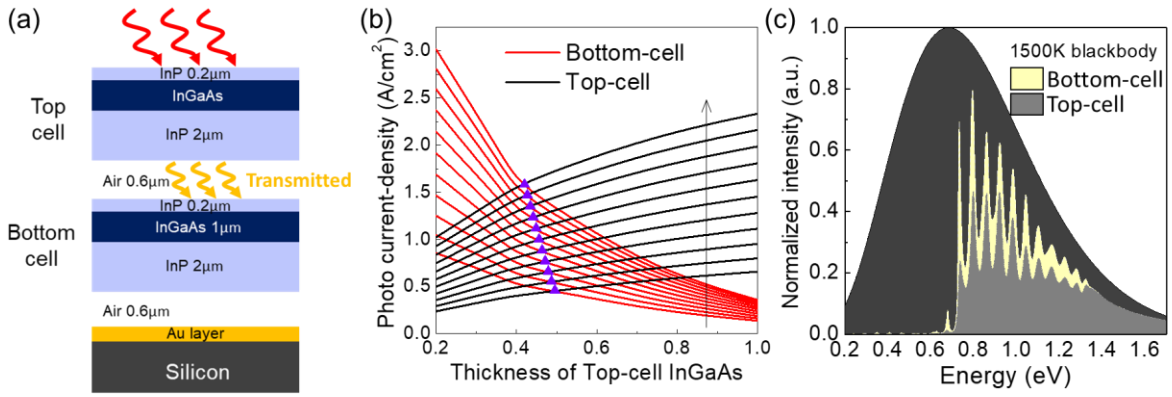

Figure 4.6 (a) Schematic of the double air-cavity layers embedded InGaAs tandem photovoltaic structure. (b) Photo-current-density (J_{ph}) versus the InGaAs-absorber thickness (t_{InGaAs}) at the top cell. The t_{InGaAs} at the bottom cell is 1 μm under the different blackbody temperatures from 1100 K to 1600 K (ΔT = 50K) as indicated by the black-solid-arrow. The violet-color-filled triangles mean the current-matched condition. (c) Simulation of absorption spectrum of top-cell (t_{InGaAs} = 0.43 μm) and bottom-cell (t_{InGaAs} = 1 μm) under 1500 K blackbody.

The performance of a tandem cell can be optimized by considering the current-matching thickness for the top cell. The photo current density (J_{ph}) of the sub-cells follows

$$J_{ph} = q \times VF \times \int_{E_g}^{\infty} \left(\varepsilon_e(E,T_h) \Big/ A_{cell}(E,T_h) \right) \times EQE(E,T_h) \times \Phi(E,T_h) dE \qquad (4.1)$$

where the *VF* is the view-factor, the ε_e is the effective emissivity of the emitter (Equation (1.4)), the *EQE* is the external-quantum-efficiency of the TPV cell, and the Φ means the spectral photon flux. Figure 4.6 (a) shows the schematic of an air-bridge InGaAs tandem structure to describe the spectral splitting through the sub-cells. In Fig. 4.6 (b), the photocurrents at the top and bottom cells are calculated as a function of the thickness of the top InGaAs absorber under different blackbody

temperatures. The J_{ph} is calculated using Eq (4.1) with the assumption of the internal-quantum-efficiency, IQE, as 98% [1] where the *VF* is assumed to 0.1. From Fig. 4.6 (b), the current matched thickness of the top-cell InGaAs is 0.43 μm for a 1500 K blackbody. Figure 4.6 (c) plots an example of the spectrum splitting of blackbody 1500 K emission at the top and bottom cells. The photon flux is determined by the emitter temperatures, resulting in the current matched thickness of the top cell as a variable as a function of T_h, which is indicated by the violet triangles as shown in Fig. 4.6 (b).

4.4 Four-terminal Air-Bridge Tandem Thermophotovoltaic Architecture

Table 4.2 $In_{1-x}Ga_xAs_yP_{1-y}$ mole fractions, bandgaps, and lattice constants.

	Bandgap (eV)	*x*	*y*	Lattice constant (Å)
InGaAsP	0.92	0.31	0.67	5.8690
	1.00	0.24	0.52	5.8687
	1.09	0.17	0.37	5.8687
	1.19	0.1	0.22	5.8690
InP	1.35	0	0	5.8688
InGaAs	0.75	0.47	1	5.8680

Sub-cells are monolithically integrated in a two-terminal TPV device, where they are electrically coupled in series and the optical splitting determines the J_{sc} of the lowest sub-cell. It constrains the PCE of the tandem TPV, meaning that current matching between the sub-cells is important for optimizing the PCE. Alternatively, a four-terminal (4-T) tandem TPV architecture allows the sub-cells to be coupled optically but separated electrically. Figure 4.7 shows the schematic of a four-terminal tandem TPV architecture. The fabrication method is similar to that in Fig. 4.1 but includes the 1–2 μm thick polyimide layer as an insulator between the sub-cells. The polyimide (PI-2555, HD Microsystems) is spin-coated on the bottom cell and patterned by dry-

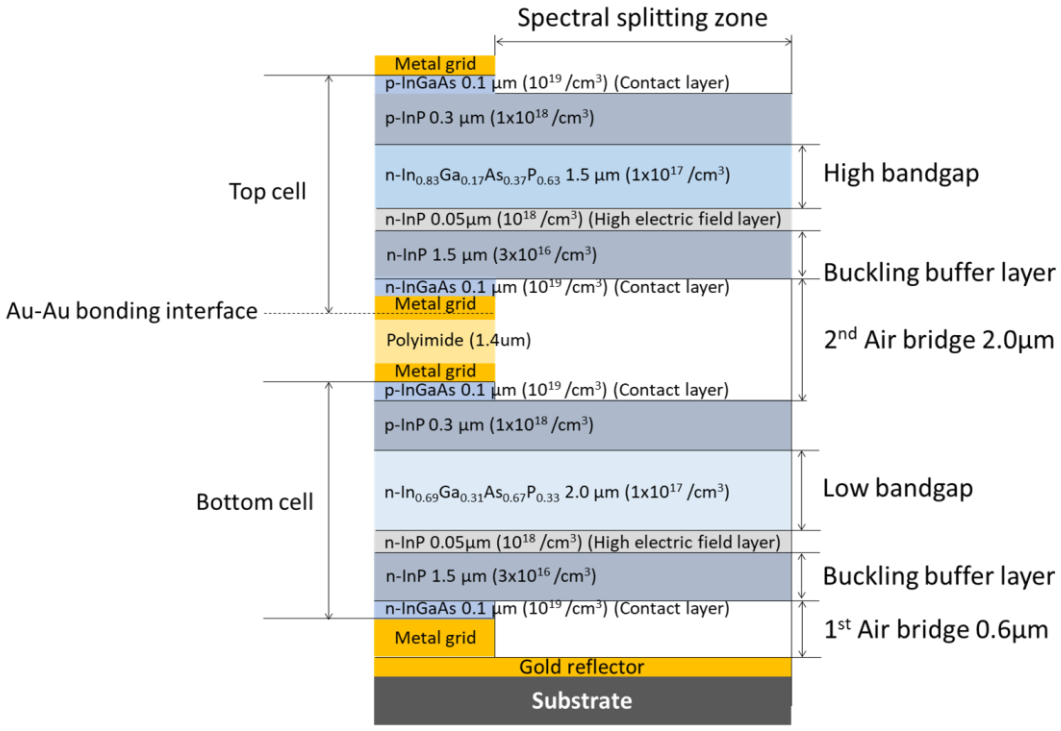

Figure 4.7 Four terminal (4T) tandem thermophotovoltaic architecture with double air-bridges. The top and bottom cells are prepared independently, then both are joined by Au-Au cold welding. The polyimide electrically separates the bottom and top cells, where the four terminals are defined at each metal grid from the bottom-most to the top-most.

etching process using oxygen plasma (the O_2 flow of 20 ppm with a plasma power 150 W). Another thin gold layer (Ti/Au of 10/100 nm) is patterned on the polyimide, and the top and bottom cells are joined by the Au-Au cold welding method. The bandgap materials are $In_{1-x}Ga_xAs_yP_{1-y}$, where the bandgap is determined by the interpolation using mole fraction dependency:

$$E_g = [x \times (1-x) \times (y \times E_g(In_{1-x}Ga_xAs) + (1-y) \times E_g(Ga_xIn_{1-x}P))]$$
$$+ y \times (1-y) \times [x \times E_g(GaAs_yP_{1-y}) + (1-x) \times E_g(InAs_yP_{1-y})]/[x \times (1-x) + y(1-y)], \quad (4.2)$$

where InGaAs, GaInP, GaAsP, and InAsP are side materials for the InGaAsP quaternary alloy. The bandgap of each side material is determined by the mole fraction dependency using corner materials of InAs, GaAs, GaP, and InP [168]. In Fig. 4.7, the tandem partners have the bandgaps

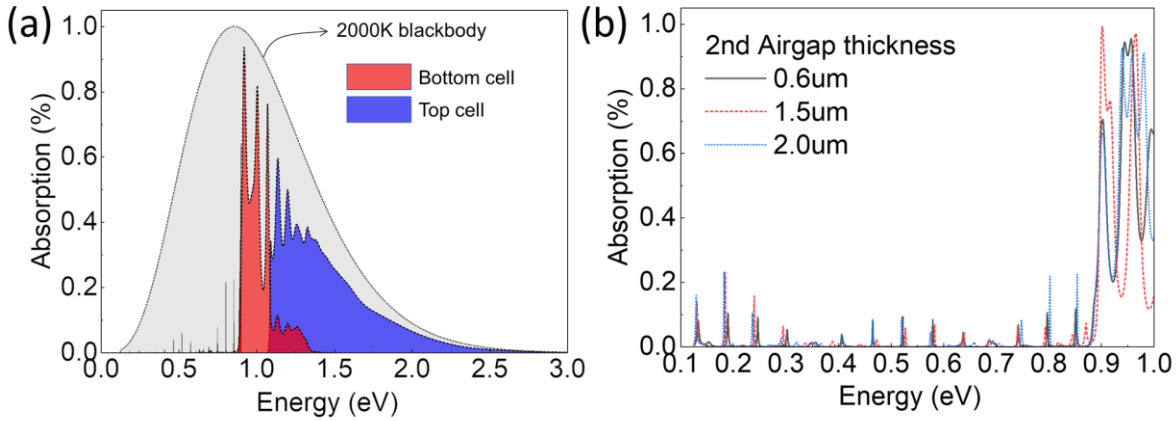

Figure 4.8 (a) Simulated absorption spectra on the tandem cell in Fig. 4.7. The red and blue spectra indicate the bottom and top cells, respectively. (b) Simulation of absorptions on the tandem cell via different second airgap thicknesses of 0.6, 1.5, and 2.0 μm.

of 1.09 and 0.92 eV for the top and bottom cells, respectively. Table 4.2 shows the material parameters for the epilayers, where InGaAsP and InGaAs are lattice-matched to InP. The optical splitting of the 4-T tandem structure is still regulated by the thicknesses of the sub-cells; therefore, we roughly choose a relatively thin thickness of 1.5 μm for the top cell absorber.

Figure 4.8 (a) shows the simulated absorption spectrum by spectral splitting through the sub-cells. The blue and red spectra indicate the absorption at top and bottom cells, respectively, under 2000 K blackbody radiation. It does not consider the loss of photons by free carrier absorption and the total OOB reflectance, R_{OOB}, is calculated by 98.81%. Figure 4.8 (b) indicates the tolerance of R_{OOB} depending on the thickness of the second air bridge. From 0.6 to 2.0 μm, the R_{OOB} varies from 98.79% to 98.81%, showing the variance is under 0.1 % and negligible.

Figure 4.9 shows the observed microscopy images during the fabrication process. Figure 4.9 (a) shows the experimental demonstration of the bottom cell with the top grids including metal/polyimide/metal stacks. Figure 4.9 (b) shows the extended area indicated by the red box in Fig. 4.9 (a). The inset shows the schematic cross the A-A'. The bottom and top gold layers overlap,

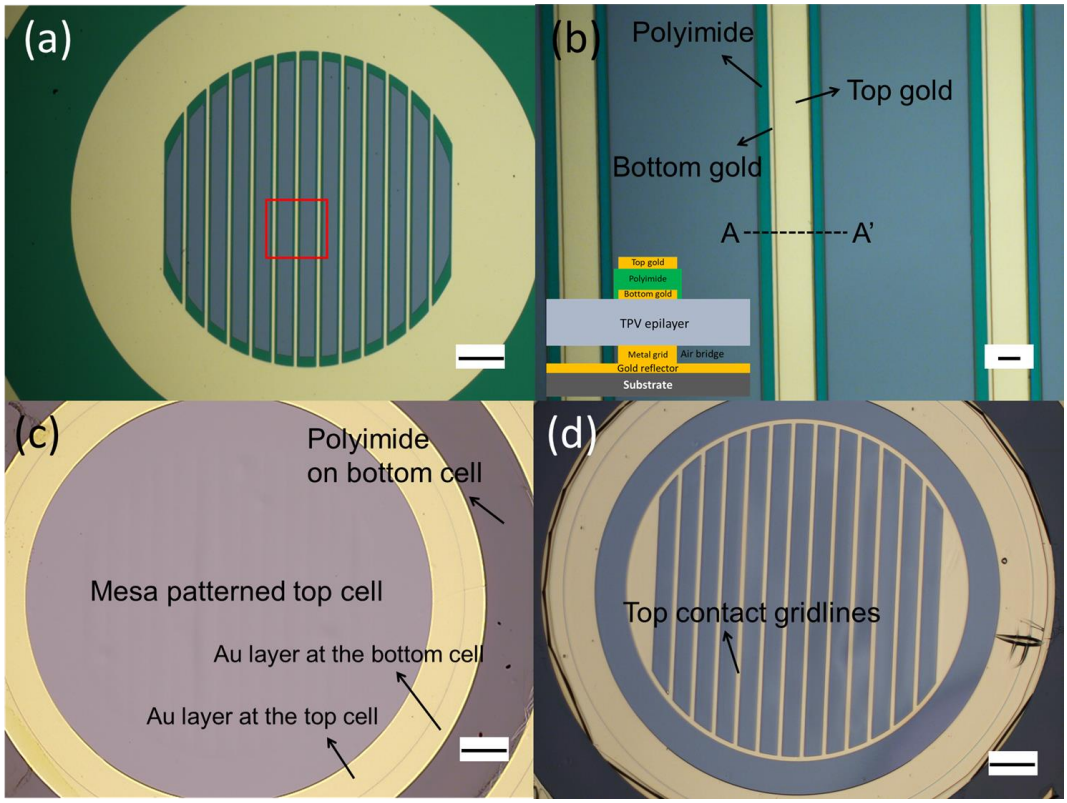

Figure 4.9 Optical microscopy images of (a) a bottom single junction with Au/polyimide/Au at the top gridlines, (c) a tandem TPV cell after Au-Au bonding between the sub-cells, InP substrate removal, and mesa patterning of the top epilayer, and (d) the TPV cell after patterning the top gold gridlines. (b) shows the extended image indicated by the red box in (a). To optimize the fabrication processes, this used an InGaAs/InP epilayer wafer instead of a InGaAsP/InP epilayer wafer.

with a misalignment of less than 2μm. Figure 4.9 (c) is after the sequential processes of Au-Au bonding, InP substrate removal, and mesa patterning for the epilayer of the top cell. Figure 4.9 (d) shows the tandem cell after patterning the top metal gridlines using a conventional liftoff process. The thick polyimide guarantees insulation between the sub-cells. However, the adhesion between polyimide and metals becomes poor owing to humidity penetration and HCl chemical attack on the Ti layers between Au and polyimide. Therefore, good adhesion is important to prevent a peel-off of the top cell and a substantial electrical leakage path through the sub-cells.

We predict the PCE of the designed tandem TPV cell in Fig. 4.7. The *J-V* follows by:

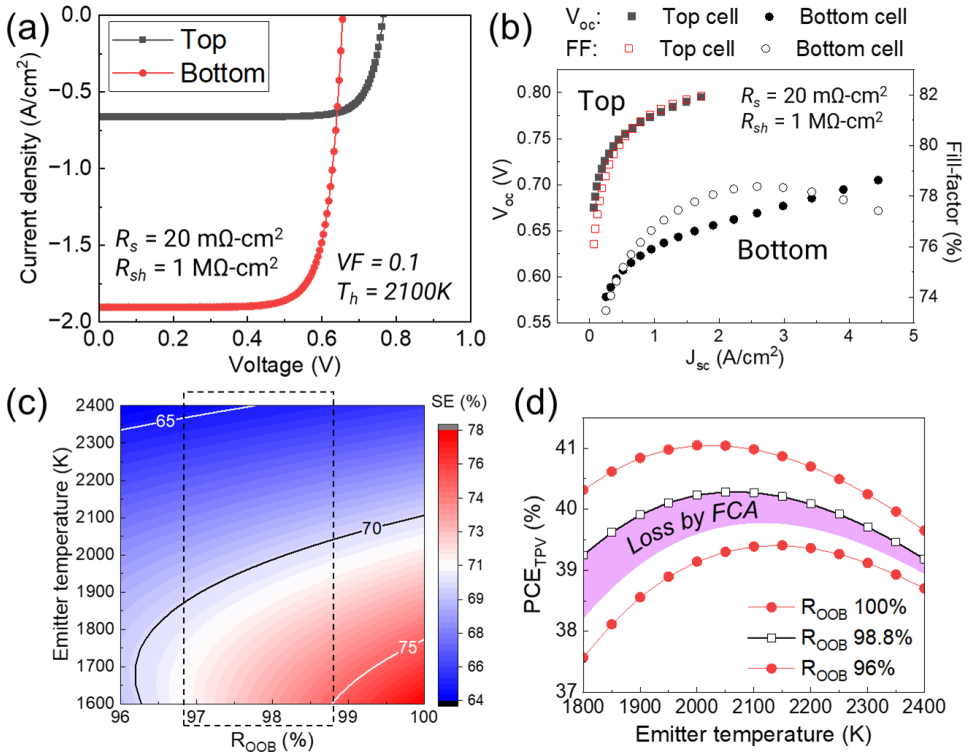

Figure 4.10 (a) Simulated current-density versus voltage characteristics of the top and bottom cells in Fig. 6.5(a). The view-factor (VF) is assumed to 0.1 under the blackbody emission 2100 K. The R_s and R_{sh} are assumed to 20 mΩ-cm^2 and 1 MΩ-cm^2, respectively. (b) Open-circuit voltage (V_{oc}) and fill-factor (FF) as a function of J_{sc} by varying the blackbody temperature from 1600K to 2400K (VF=0.1). The loss of V_{oc} to the ideal V_{oc} is about 0.15V (Chapter 5). (c) Contour plot of the spectral efficiency, SE, as a function of R_{OOB} and emitter temperatures (emissivity = 1). (d) Calculation of power-conversion-efficiency (PCE) of the tandem TPV cell in Fig. 4.7 using the Eq. (4.5). The R_{OOB} in Fig. 4.7 and Fig. 4.8(a) shows 98.8% without the consideration of parasitic photon losses. Considering the uncertainty of R_{OOB} loss, the colored region indicates the predicted PCE range, where the maximum R_{OOB} loss is 2%.

$$J_D = J_{sc} + q\frac{Dn_i^2}{N_d W_d}\left[\exp(q(V - R_s J_D)/k_b T_c) - 1\right] + \frac{qn_i W_d}{\tau_{eff}}\left[\exp(qV - R_s J_D/2k_b T_c) - 1\right], \qquad (4.3)$$

where D is the diffusivity, n_i is the intrinsic carrier concentration, N_d is the doping concentration, W_d is the depletion width, k_b is the Boltzmann constant, T_c is the cell temperature, and τ_{eff} is the effective carrier lifetime. The n_i is calculated by:

$$n_i = 2\left(\frac{2\pi k_b T}{h^2}\right)^{3/2} \times \left(m_e^* m_h^*\right)^{3/4} \times exp\left(\frac{-E_g}{2k_b T}\right), \quad (4.4)$$

where h is the Planck constant and m_e^* and m_h^* are effective charge masses for electron and hole, respectively. The effective masses are determined by the mole fractions in Table 4.2 [168]. The R_s and R_{sh} depend on practical factors such as epilayer growth and fabrications. To calculate J_D using Eq. (4.3), we assume the resistance factors from the literature [1]. Figure 4.10 (a) shows the *J-V* characteristics in the dark for the sub-cells. Figure 4.10 (b) plots the *J-V* characteristics for the top and bottom cells via an optical splitting through the intermediate air-bridge under a blackbody temperature of 2000 K. Figure 4.10 (c) is the calculated V_{oc} and fill-factor (*FF*) as a function of J_{sc}. The J_{sc} is calculated by varying the blackbody temperature from 1600 to 2400 K with a 50 K interval. Figure 4.10 (d) shows the calculated spectral efficiency, SE. The in-band reflectance is not significantly sensitive to the reflector. The R_{OOB} of the tandem structure in Fig. 4.7 shows near 99%. To calculate the practical PCE range of the tandem TPV cell, we consider parasitic loss of R_{OOB} about 2 % by free-carrier absorption and cavity oscillations. Figure 4.10 (d) shows the calculated PCE using:

$$PCE_{\mathrm{TPV}} = \frac{P_{out}}{P_{inc}\text{-}P_{ref}} = \frac{\sum_{\mathrm{m=1}}^{\mathrm{n}} V_{oc,m} \times J_{sc,m} \times FF_m}{P_{inc} - P_{ref}}, \quad (4.5)$$

where m means the m-th sub-cell in a TPV cell, and n = 2 in Fig. 4.7. The R_{OOB} in Fig. 4.8(a) is 98.8%, which does not consider parasitic photon losses. Therefore, we calculate the PCE for three cases of R_{OOB} = 100%, 98.8%, and 96%, which shows the maximum PCE of 41.4% (T_h = 2000 K), 40.3% (T_h = 2050 K), and 39.4% (T_h = 2150 K), respectively. However, this calculation assumes the practical factors of R_s and R_{sh} as 20 mΩ-cm^2 and 1 MΩ-cm^2, respectively, which results in the voltage loss of 0.15V (Chapter 5). We note that the R_s and R_{sh} are strongly dependent on the quality of the epitaxial layer and the metal resistance. Therefore, the PCE can be increased higher than the prediction in case R_s < 20 mΩ-cm^2 and the voltage loss is less than 0.15V.

4.5 Conclusion

First, we demonstrated a mechanical bonding method to fabricate a monolithic air-bridge InGaAs/InGaAs tandem TPV cell. The electrical connection between sub-cells is enabled by the Au-Au interlayer formed by cold welding, eliminating the requirement of heavily doped regions for tunnel junctions. To address the optical splitting, the second air-bridge layer is inserted between the sub-cells. Conceptually, this tandem architecture does not need lattice-matched growth between sub-cells, allowing it to expand the choice of tandem partners with desired bandgaps. The demonstration of an InGaAs homo-tandem TPV cell shows a V_{oc} about 0.8 V, which is twice of the V_{oc} of 0.4 V in a single InGaAs TPV cell. The R_{OOB} of the tandem shows 96.18% (96.95% for a single cell), which can be optimized with the management of total carrier concentration in the semiconductors. However, the monolithic tandem configuration should fulfill current matching between the top and bottom cells for PCE optimization.

Second, we introduce a four-terminal configuration in a tandem device where sub-cells are mechanically stacked, which mitigates the strict dependence on current matching between sub-cells. The connection of the sub-cells is performed by Au-Au cold welding, where a patterned 1.5-μm-thick polyimide layer is inserted between the sub-cells. To demonstrate a four-terminal tandem cell, we design a multi-junction diode structure having 1.1 eV and 0.9 eV for the top and bottom cells, respectively. The thickness of the top absorber is 75% that of the bottom absorber, which increases the electrical output compared to the thickness matching. The R_{OOB} is estimated by 98.8%, however, it does not consider parasitic losses of out-of-band photons. We simulate the PCE as a function of emitter temperatures and R_{OOB} (96–100 %). The PCE reduction is only 1.64% from R_{OOB} 100% to 96%, implying that the PCE is significantly affected by diode performance such as

R_s, R_{sh}, and carrier lifetime. Although our demonstration only focuses on lattice matched epilayers, this method has the potential to address a wide range of bandgap partners for tandem TPV devices without strict fulfillment of lattice-matching epitaxial growth.

Chapter 5 Limits to the Energy Conversion Efficiency of Air-Bridge Thermophotovoltaics

5.1 Introduction

Fossil fuels are the primary source of energy consumption in buildings, transportation, and manufacturing [38,40,119]. However, the usage of these fuels accelerates climate change, deforestation, and scarcity of resources [11,12,119]. This has attracted increasing interest in non-fossil fuel sources for the generation of electricity, exemplified by solar photovoltaic (PV) cells [25,30-32,34,35,169]. A significant challenge to using renewables, however, is the need for very low-cost energy storage. Recovery of excess energy stored as heat is one way to eliminate, or augment commonly used electrochemical or pumped water storage. Specifically, power generation using thermophotovoltaic (TPV) cells has the advantage of employing low maintenance cost thermal storage with high-power density and without constraints as to their location [1,5,48-51].

The basic architecture of a TPV cell is that it has a high efficiency for converting above bandgap (in band, IB) photons to electrons, while reflecting out-of-band (OOB), low energy photons back to the source. This design requires a back-surface-reflector (BSR) with near-unity reflectivity. The recently introduced air-bridge (AB) TPV provides a unique means to maximize the reuse of OOB photons via loss-free Fresnel reflections [1,170]. Understanding the limits to various approaches to TPV design is necessary to develop guidelines that lead to enhanced energy conversion. In a TPV system design, we must consider three factors: 1. The radiative path between

the heat source (the emitter) and the cell, 2. the temperatures of the emitter and the cell, and 3. IB photon absorption efficiency, OOB reflection efficiency, and parasitic photon losses. Among several attempts to more closely approach the TPV thermodynamic efficiency limits, Baldasaro, *et al.* stressed the importance of parasitic loss of photons and spectral control limitations, which results in a tradeoff between the cell bandgap and its efficiency [171].

Here we analyze the efficiency limits of the AB-TPV cell based on detailed balance. We employ the Drude model for III-V materials which quantifies the spectral efficiency (SE) loss due to free-carrier absorption (FCA) in undepleted regions of the cell. We then calculate the efficiency limits of a lattice-matched InGaAs diode, and the SE determined by the active PV membranes suspended between conductive gridlines to form air bridges. We employ a technology computer-aided design (TCAD) model for InGaAs AB-TPV cells to include recombination losses that degrade the open-circuit voltage (V_{oc}), shunt-path losses, and the influence of the cell and geometric fill factors (*FF* and *GFF*, respectively). Finally, we determine the thermodynamic efficiency limits based on detailed balance and the dependence of OOB photon loss as a function of bandgap and emitter temperature.

5.2 Methods

TCAD simulation

The air-bridge InGaAs TPV simulations were performed using Synopsys Sentaurus (Version S-2021.06), which simulates the charge-carrier distribution and transport by solving the charge continuity, Poisson, and drift-diffusion equations. In the simulator (Sentaurus Device), the SRH model was included to account for non-radiative recombination. Also, the TMM solver calculates light propagation under blackbody spectrum. The Drude model reflects the FCA effect during the

light propagation. We used the Sentaurus default material database (DB) for the $In_{0.53}Ga_{0.47}As$, InP, and metals. In the DB, the physics parameters of $In_xGa_{1-x}As$ follow the linear interpolation method using conner materials (InAs, GaAs). In the DB, the material air is not built-in and therefore its material properties were added manually. Parameters for air: Permittivity constant (ε) = 1, Refractive index = 1, Complex refractive index (n_r and k_r) = 1 and 0, Resistivity (Ω-cm) = 10^{13}. Appendix 3 provides additional TCAD results.

5.3 Result

I. Efficiency Limits and Losses in AB-TPVs

Figure 5.1 illustrates the components of an AB-TPV. The PV cell comprises an InGaAs (In:Ga=0.53:0.47) active region grown by molecular beam epitaxy lattice-matched on (100) InP. The transfer of the epitaxy to the Si substrate is achieved via Au-Au cold weld bonding to the BSR [65]. The top gold metal is deposited by e-beam evaporation, followed by patterning it and the p-type InGaAs contact layer. The black body emitter and PV cell are at temperatures of T_h and T_c, respectively, while the substrate temperature (T_s) is also at T_c [170,172]. The paths for photon flux have contributions, Θ_{in}^{h}, from the emitter, and Θ_{in}^{b} from the BSR. The flux is reduced by absorption and parasitic loss in the PV cell, expressed by $\Theta_{in}^{h} = \alpha_{PV}^{1} + \Theta_{out}^{b}$, where α_{PV}^{1} are the parasitic losses

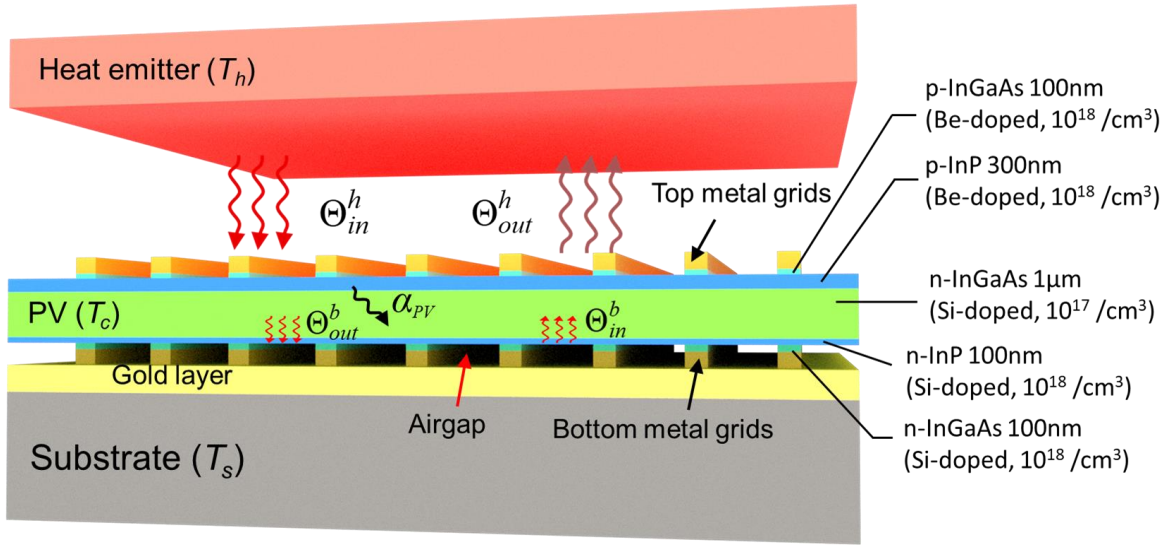

Figure 5.1 Schematic to illustrate a thermophotovoltaic system composed of a heat emitter, a photovoltaic diode with metal grids, and a substrate connecting to a heat sink. The PV cell has five epilayers of InGaAs and InP. The numbers in parentheses mean the dopant concentrations of Si and Be.

at the metal/semiconductor interface and absorption by the reflector, and Θ^h_{out} is the photon flux reaching the reflector. An air cavity minimizes the losses, thereby leading to $\Theta^b_{in} \approx \Theta^b_{out}$ and $\Theta^b_{in} = \alpha^2_{PV} + \Theta^h_{out}$, where α^2_{PV} is photon absorption in the PV, giving a total absorption of $\alpha_{PV} = \alpha^1_{PV} + \alpha^2_{PV}$.

The sub-bandgap, or OOB reflectance, is $R_{OOB} = \Theta^h_{in} - \Theta^h_{out}$. Now the view-factor, VF, is the ratio of overlap of the emitter and detector areas. Since the two black bodies are planar with areas larger than their separation, $VF = 1$. The absorption in the PV is the sum of radiative and non-radiative terms, where the non-radiative term is primarily due to defects in the bandgap and free-carrier absorption (FCA), which in turn, decreases SE and the output power of the PV cell (P_{out}). Under illumination, the top and bottom metal gridlines conduct free charges to electrodes at the periphery of the cell. The geometric fill factor, which is the ratio of the metal grid to the total device area is $GFF \leq 1$. This contributes to an additional reduction of SE.

To calculate the maximum achievable energy conversion efficiency based on detailed balance (i.e. the thermodynamic limit) of AB-TPVs for a TPV having unity external quantum efficiency (EQE), we assume that T_c is fixed at 293K, and R_{OOB} = 100%. Table 1 compares parameters used to estimate the maximum and practical power conversion efficiencies (PCE) of a previously reported InGaAs AB-TPV cell [1]. For the practical cell, we include the loss of OOB photons by FCA, series resistance (R_s) including contact resistance (R_c), junction shunt resistance (R_{sh}), and internal (IQE) and external-quantum-efficiency (EQE). The practical efficiency limit is calculated by assuming three extrinsic sources: R_{OOB} loss of the cavity mode, less than unity EQE, and ohmic losses. In this approximation, FCA, R_c losses and SRH are neglected. Finally, we consider shadowing by top metal grids, causing additional photon loss.

Table 5.1 Parameters used for the ideal and practical InGaAs AB-TPV cells.

Parameters	Ideal limit	Design limit	Practical case (Ref.1)
R_{OOB} (%)	100	98.62	97.84
R_s (mΩ·cm^2)	0	12	26
R_c (Ω·cm^2)	0	≤ 2×10^{-7}	2.0×10^{-5}
R_{sh} (Ω·cm^2)	∞	∞	127.7
EQE (%)	0	0	2×10^{5}
IQE (%)	100	68	68

5.3.1 Efficiency Limit of a Thermophotovoltaic cell

The SE is given by:

$$SE = \frac{E_g \times \int_{E_g}^{\infty} \varepsilon_{eff}(E) \times \Phi(E) dE}{\int_0^{\infty} \varepsilon_{eff}(E) \times E \times \Phi(E) dE}, \tag{5.1}$$

where $\Phi(E)$ is the photon flux from the emitter and ε_{eff} is the effective emissivity [1,51,55], given by [47,55]:

$$\varepsilon_{eff}(\mathrm{E}) = \frac{1-R_{\mathrm{e}}(E)}{1-R_{\mathrm{e}}(E) \times R_{\mathrm{cell}}(E)} \times \alpha_{\mathrm{PV}}. \tag{5.2}$$

Here, $R_{\mathrm{e}} = 1-\varepsilon_e$ and R_{cell} are the spectral reflectances of the emitter and the cell, respectively. Next, *PCE* is given by [89,171]:

$$PCE = \frac{P_{out}}{P_{abs}} = \frac{V_{oc} \cdot J_{sc} \cdot FF}{q \times VF \times \int_0^{\infty} \varepsilon_{eff}(E) \times E \times \Phi(E) dE} = SE \cdot IQE \cdot \frac{V_{oc}}{E_g} \cdot FF, \tag{5.3}$$

where P_{abs} is the TPV cell absorbed power, and J_{sc} is the short-circuit-current. The current density-voltage characteristics are as follows:

$$J = J_1\left[\exp\left(\frac{q(V-R_sJ)}{k_bT_c}\right) - 1\right] + J_2\left[\exp\left(\frac{q(V-R_sJ)}{2k_bT_c}\right) - 1\right] + \frac{V-R_sJ}{R_{\mathrm{sh}}} - J_{ph}, \tag{5.4}$$

where J_1 and J_2 are the saturation current densities for diffusion and recombination-limited current sources (including bulk, surface, and junction recombination), respectively, J_{ph} is the photocurrent density, and k_b is the Boltzmann constant. In the radiative limit, the photocurrent density is given by:

$$J_{ph} = q \times VF \times \int_0^{\lambda_g} \frac{\varepsilon_e(\lambda)}{1-R_{\mathrm{e}}(\lambda) \times R_{\mathrm{cell}}(\lambda)} \times IQE(\lambda) \times \alpha_{cell}(\lambda) \times \Phi(\lambda) d\lambda. \tag{5.5}$$

Here, $J_{ph} = J_{sc}$ and IQE = 100%. From Eq. (5.4), V_{oc} is expressed by:

$$V_{oc}^{rad} = \frac{k_bT_c}{q} \times \ln\left(\frac{J_{sc} - \frac{V_{oc}}{R_{sh}}}{J_1 + J_2 \exp\left(-\frac{qV_{oc}}{2k_bT_c}\right)}\right) \cong \frac{k_bT_c}{q} \times \ln\left(\frac{J_{sc} - \frac{V_{oc}}{R_{sh}}}{J_1}\right), \tag{5.6}$$

Including non-radiative (*nr*) recombination, the voltage is decreased by:

$$\Delta V_{loss} = V_{oc}^{rad} - V_{oc}^{nr} = \frac{k_bT_c}{q} \times \ln\left(\frac{J_{sc}^{rad}}{J_{sc}^{nr} - \frac{V_{oc}^{nr}}{R_{sh}}} \times \frac{J_1^{nr}}{J_1^{rad}}\right). \tag{5.7}$$

The origin of the ΔV_{loss} in the AB device is understood using:

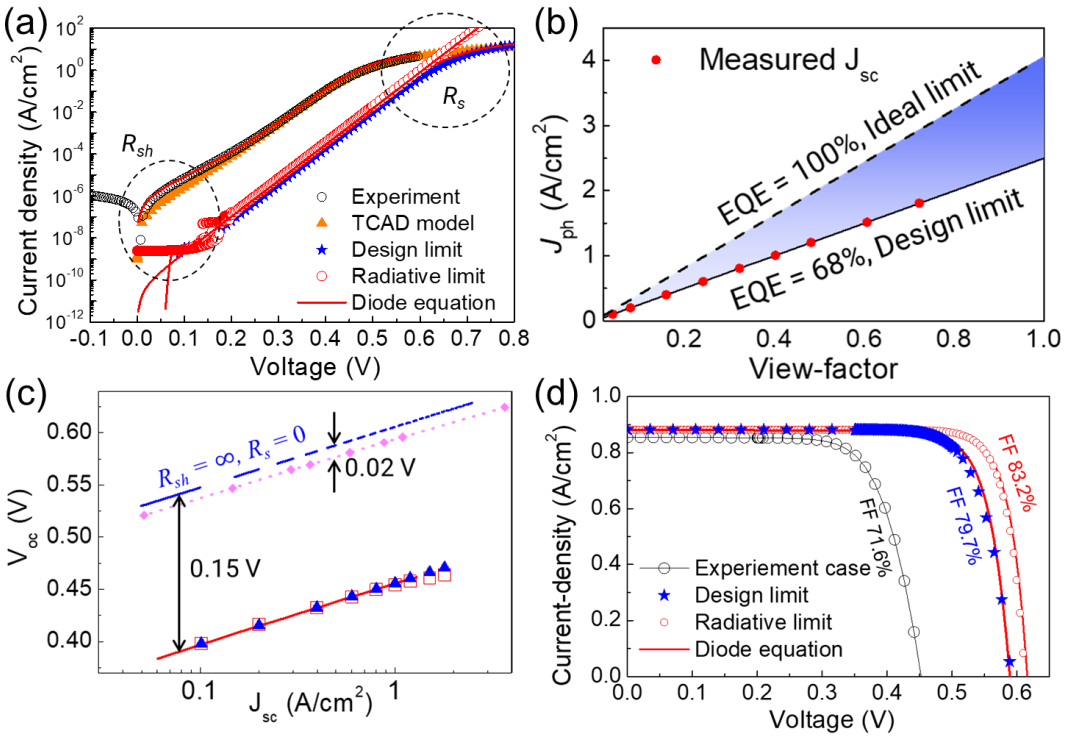

Figure 5.2 (a) Dark current density-voltage (*J-V*) characteristics of an InGaAs/InP AB-TPV cell. The low bias region (< 0.1 V) is governed by junction shunt resistance (R_{sh}) and the high bias region (> 0.4 V) is dominated by series resistance (R_s). Open circles are for the InGaAs AB-TPV cell from Ref. [1]. The design limit assumes that the R_s is only determined by semiconductors and the contact resistance (R_c) and the Shockley-Read-Hall (SRH) at the p-n junction are negligible. The radiative limit assumes $R_s = 0$ and $R_{sh} = \infty$. The solid curves are fits using Eq. (5.4) in text. (b) Photo current-density (J_{ph}) calculated as a function of the view-factor (VF). The symbols are the measured short circuit current density (J_{sc}) from the device in Ref. [1]. (c) Open-circuit voltage (V_{oc}) as functions of the J_{sc}. Rectangles: from the device in Ref. [1].Triangles: from a technology computer-aided design (TCAD) model. Dashed line: Radiative limit. Diamond-dot line: Design limit. The losses of V_{oc} were calculated using Eq. (5.7). (d) *J-V* characteristics for the InGaAs AB-TPV cell using the TCAD model. The circle solid line is the model fit to Ref. [1].

$$J_D = J_{sc} + q\frac{Dn_i^2}{N_d W_d}\left[\exp(qV/k_bT_c) - 1\right]\Big|_{\text{rad}} + \frac{qn_iW_d}{\tau_{SRH}}\left(\exp(qV/2k_bT_c) - 1\right)\Big|_{\text{non-rad}}, \quad (5.8)$$

where $N_d = 10^{17}$ /cm^3 is the carrier concentration the InGaAs active layer, W_d is the depletion width at the *p*-*n* junction, D is the diffusion coefficient of minority carrier holes, n_i is the intrinsic carrier concentration, and τ_{SRH} is the Shockley-Reed-Hall (SRH) recombination time [173]. Eq. (5.8) is identical to (5.4) where $V \rightarrow V - R_sJ_D$. The V_{oc} at $J_D = 0$ is determined by N_d, which varies with W_d and τ_{SRH}. The recombination lifetime (τ_c) is given by:

$$1/\tau_c \cong 1/\tau_{SRH} + 1/\tau_{rad} \cong (\tau_{SRH}^{-1} + BN_d), \quad (5.9)$$

where B is the radiative recombination coefficient:

$$B_{rad} = \frac{2\pi}{n_i^2h^3c^2}\int_{E_g}^{\infty} E^2 \times \alpha(E) \times \exp^{\left(-\frac{E}{k_BT}\right)} dE, \quad (5.10)$$

where n_i is intrinsic carrier concentration, c is the light velocity, and $\alpha = 4\pi k_r/\lambda$ [174]. We obtain $B_{rad} = 2.0\times10^{-10}$ cm^{3}s^{-1} [175,176], and $\tau_c = 30$ ns [177,178] using TCAD. This matches the other reports (17 – 70 ns) for InGaAs [175,179]. The design limit (it defines a design limit only for the structure in Fig. 5.1) assumes that $\tau_{SRH} \rightarrow \infty$, and $B_{rad} = 4.1\times10^{-12}$ cm^{3}s^{-1}. Rewriting Eq. (5.6), the J_{sc} is expressed by:

$$J_{sc} \approx \exp(qV_{oc}/k_bT_c) \times \left[q\frac{Dn_i^2}{N_dW_d} + \frac{qn_iW_d}{\tau_{SRH}}\left(e^{-qV_{oc}/2k_bT_c}\right)\right], \quad (5.11)$$

where the first term in the square brackets is ~10^{-8} A/cm^2. At $\tau_{SRH} > 1\mu$s, the second term is < 10^{-10} A/cm^2, and hence is negligible.

Finally, the open circuit voltage of the InGaAs TPV in the radiative limit is $V_{oc} = 0.63$ V ($T_c = 293$ K, $T_h = 1450$ K, $E_g = 0.74$ eV) given by [10,171,180]:

$$V_{oc}^{rad} = k_BT_c \ln\left(\frac{J_{sc}}{J_0} + 1\right)\Big|_{\text{rad}} = E_g\left(1 - \frac{T_c}{T_h} + \frac{k_BT_c}{E_g}\ln\left(\frac{T_h}{T_c}\right)\right). \quad (5.12)$$

As R_{sh} is decreased, ΔV_{loss} is increased from Eq. (5.7) [172].

Figure 5.2(a) shows the radiative limited *J-V* characteristics (blue circles) corresponding to $R_{sh} \rightarrow \infty$ and $R_s \rightarrow 0$. Also shown is the measured dark current from the AB-TPV in Ref. [1], along with a fit to Eq. (5.4) (red solid line) yielding R_{sh} = 1 MΩ-cm^2, R_c = 2.02×10^{-5} Ω·cm^2, and R_s = 26 mΩ-cm^2. The grey-filled symbols show the design limit where the SRH is negligible, resulting in R_s = 12 mΩ-cm^2 and $R_c \rightarrow 0$, whereas in the thermodynamic limit we have R_s = 0 and $R_{sh} = \infty$.

The EQE of the InGaAs AB-TPV cell has 68 % as the design limit. From Eq. (5.5), the J_{sc} is calculated for a blackbody spectrum of 1500 K as a function of VF as shown in Fig. 5.2(b), which agrees with experiment (filled circles), suggesting that IQE approaches 100% [1,89]. Thus, the experiment is nearly the same with the design limit. The EQE is limited by the Fabry-Perot cavity oscillations and the TPV thickness [181], resulting in the loss of EQE about 32 %.

Figure 5.2 (c) compares the parameters of V_{oc} and J_{sc} for the experiment (rectangles), the TCAD model (triangles), the design limit (diamonds dotted line), and the ideal limit (dashed line). The design limit was calculated by using the same TCAD model but assuming that the metal contact resistance (R_c) and the charge loss by non-radiative recombination at the p-n junction are negligible. The design limit has R_s = 12 mΩ·cm^2. Using the Eq. (5.7), ΔV_{loss} = 0.15 V and 0.02 V for the experiment case and design limit, respectively.

Figure 5.2(d) compares the different *J-V* characteristics under illumination at T_h = 1500 K. The experiment model for the InGaAs AB-TPV cell ignores surface recombination at mesa-sidewall because the TPV size is relatively large [140]. The red circles and blue starts represent the radiative limit and the design limit calculated using the TCAD (Appendix A3). The design limit assumes no junction recombination, resulting in the high V_{oc} nearly close to the ideal limit.

The experiment model has the junction recombination velocity (v_{rec}) about 2×10^5 cm/s, meaning that the charge loss at the p-n junction generates a large loss of V_{oc}. The diode equation, Eq. (5.4), was used to calculate the fitting lines. In the diode equation, the dark current density was calculated by integrating the blackbody spectrum (T_c = 293K) over the in-band region [171]. The J_{sc} difference is only 3% between the ideal and the experiment case.

5.3.2 Spectral Efficiency loss from Free-Carrier Absorption

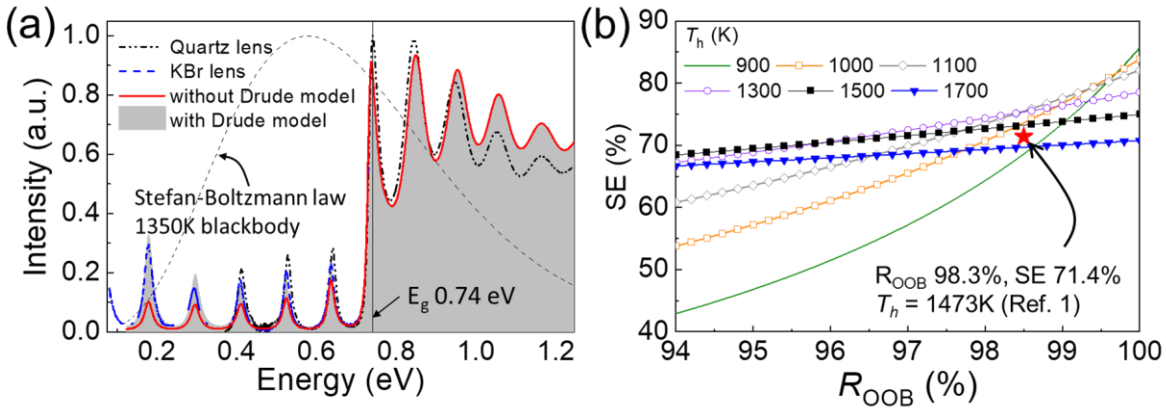

Figure 5.3 (a) Measured and simulated Fourier-transform infrared spectroscopy (FTIR) spectrum for Au BSR InGaAs TPV. The FTIR measurements were performed using two different lenses (quartz (λ = 1.0 − 3.57μm) and KBr (1.70 −15.4μm)). The Drude model simulation fits the measured spectrum. (b) Calculation of spectral efficiency as a function of R_{OOB} for several emitter temperatures, T_h. The absorption spectrum above the bandgap is from Fig. 2(b).

At infrared wavelengths, the interaction of free carriers with infrared photons results in a decreased R_{OOB}. The Drude model is used to calculate the extinction coefficient [182,183]:

$$k_r = \frac{1}{4\pi}(\lambda^{\gamma} Cn), \tag{5.13}$$

where λ is the wavelength, γ and C are parameters dependent on the sample reflectance, and n is the free carrier concentration (Appendix A4.). The dashed and dotted lines in Fig. 5.3a indicate the Fourier transform infrared spectroscopic measurement on a Au BSR InGaAs TPV cell. The solid line and shaded area are from simulations using the transfer matrix method (TMM). In the absence of FCA, the k_r at sub-bandgap energies < 0.74 eV is zero, and k_r is calculated to fit the measured Fourier-transform infrared spectroscopy (FTIR) results using Eq. (5.13) in the presence of FCA. From simulations, R_{OOB} = 94.4% at photon energies, E_{ph} = 0.12 – 0. 74 eV, without FCA, and 91.3% when it is included, giving an excess loss of ΔR_{OOB} = 3.1%. A large portion of the loss is due to the undepleted layers (with $n > 10^{18}$ /cm^3). The Fabry-Perot oscillations are determined by the total PV thickness.

Table 5.2 Drude model parameters for InGaAs and InP.

Material	γ_k	C_k
InGaAs	3.04	3.33×10^{-18}
InP	3.13	3.71×10^{-18}

Figure 5.3(b) shows the relationship between SE and R_{OOB} for the TPV in Fig. 5.1, assuming an effective emitter emissivity of unity. The trend reveals that a relatively high R_{OOB} leads to higher efficiency, although the improvement decreases with T_h.

5.3.3 Losses due to Out-of-band Photon Mirroring by the Air-Bridge Reflector

Figure 5.4(a) shows the calculated absorption spectrum of the InGaAs AB-TPV structure with an airgap of 0.6 μm.[1] Once more neglecting FCA, the calculated R_{OOB} = 98.6% for λ =

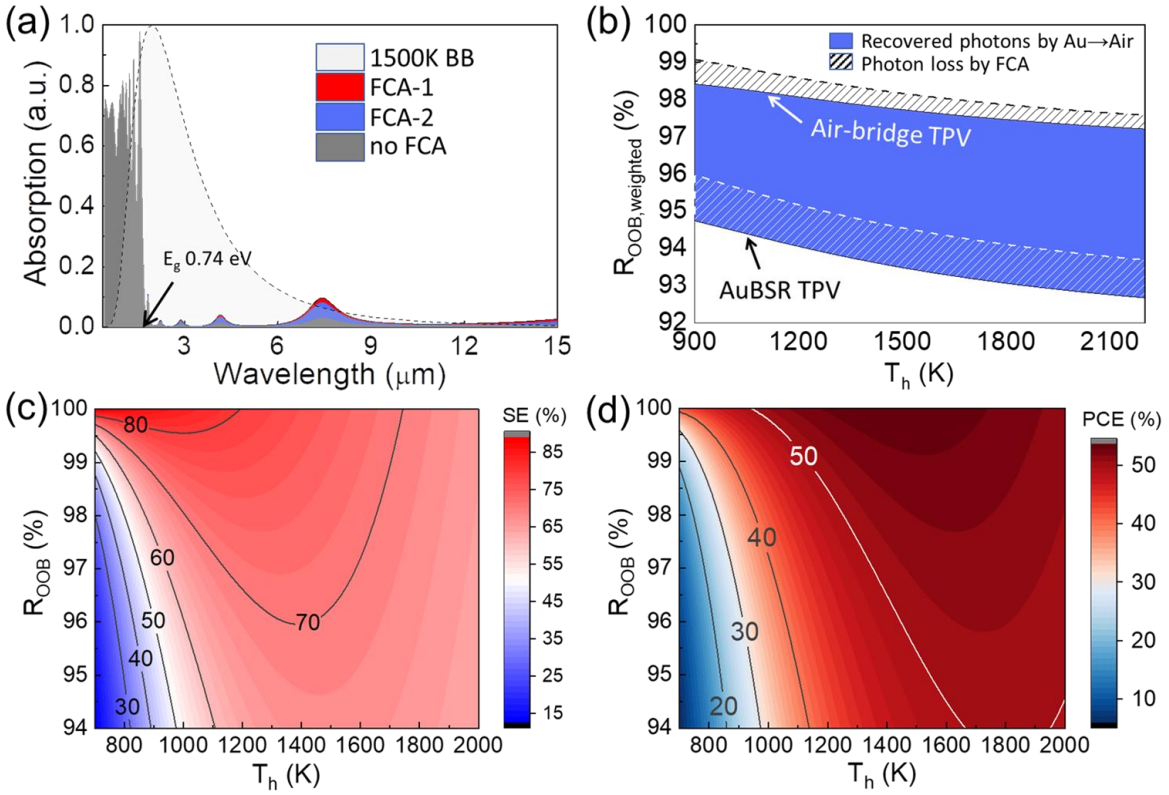

Figure 5.4 (a) Simulated power distribution spectrum for the air-bridge InGaAs TPV in Fig. 5.1. FCA-1 corresponds to doped InGaAs and InP, whereas FCA-2 assumes doping only in InP. The dotted line is the 1500 K blackbody spectrum. (b) Calculated R_{OOB} vs. T_h. The cross-hatched region is the loss due to FCA, and the shaded region is due to improvements in R_{OOB} achieved by replacing the Au BSR with air. (c) Contour plot of the spectral efficiency (SE) as a function of R_{OOB} and T_h. As decreasing the R_{OOB}, the SE is significantly dropped at a relatively low T_h (left bottom) implying that the importance of a high R_{OOB} rises at the low T_h. (d) Contour plot of the maximum power conversion efficiency (PCE) as a function of R_{OOB} and T_h. As R_{OOB} increases, the variation of the PCE becomes less sensitive to T_h.

1.68μm – 15μm, and is 97.8% (corresponding to ΔR_{OOB}, = 0.8%) when FCA is included (FCA-1). When FCA is negligible, R_{OOB} is reduced to 98.1 % (ΔR_{OOB} = 0.5 %) (FCA-2). In this case, the reduction is largely due to the relatively highly doped InP layers. Figure 5.4(b) compares R_{OOB} weighted by the blackbody spectrum for AB and Au-BSR TPVs using the same diode structure.

The shaded region indicates the improvement in reflectivity achieved by replacing the Au-BSR with an air-bridge, resulting in a significant increase in R_{OOB} by 2.5% to 3.7%. The dashed regions are the loss, ΔR_{OOB} due to FCA, which is ~1% at T_h > 1300 K for the AB-TPV. In Fig. 5.4(c), we observe that the relationship between SE and R_{OOB} becomes important at a relatively low T_h, where the difference in SE between the AB and Au BSR devices is 23% at T_h = 900 K, but it is reduced to less than 3% at T_h > 1700 K. Figure 5.4(d) shows the dependence of PCE on SE as a function of T_h and R_{OOB}, where the diode is assumed to exhibit only radiative recombination of charge carriers. Compared to the Au-BSR, the AB-TPV cell leads to a >40% increase in efficiency for T_h > 900 K. For R_{OOB} = 1, PCE exceeds 40%, even at the lowest temperatures.

5.3.4 Loss due to the Geometric Fill-Factor

The current density in TPVs is typically much higher than in solar PVs due to the proximity of the thermal source. For this reason, it is important to use conductive gridlines to extract the photocurrent with minimum resistance loss. Hence, there is a tradeoff in efficiency between gridline shadowing and series resistance. The area occupied by the gridlines is the geometric fill factor, GFF = $[(W_{PV} - W_M) \times W_{PV}]/(W_{PV})^2$ assuming a square cell configuration, where W_{PV} is the open cell width, and W_M is the area occupied by the gridlines (see Fig. 5.1). The metal grid reduces the SE as follows (cf Eq. 5.1):

$$SE = \frac{\mathrm{GFF}\times E_g \times \int_{E_g}^{\infty} \varepsilon_{eff}(E)\times\Phi(E)dE\Big|_{PV}}{\mathrm{GFF}\times \int_{0}^{\infty} \varepsilon_{eff,PV}(E)\times E\times\Phi(E)dE\Big|_{PV} + (1-\mathrm{GFF})\times \int_{0}^{\infty} \varepsilon_{eff,M}(E)\times E\times\Phi(E)dE\Big|_{Metal}}, \tag{5.14}$$

where the $\varepsilon_{eff,PV}$ and $\varepsilon_{eff,M}$ are the effective emissivities of the active area and the metal grid, respectively. The numerator is the absorption in the PV region, and the denominator expresses the total reflected photons from the BSR and the gridlines.

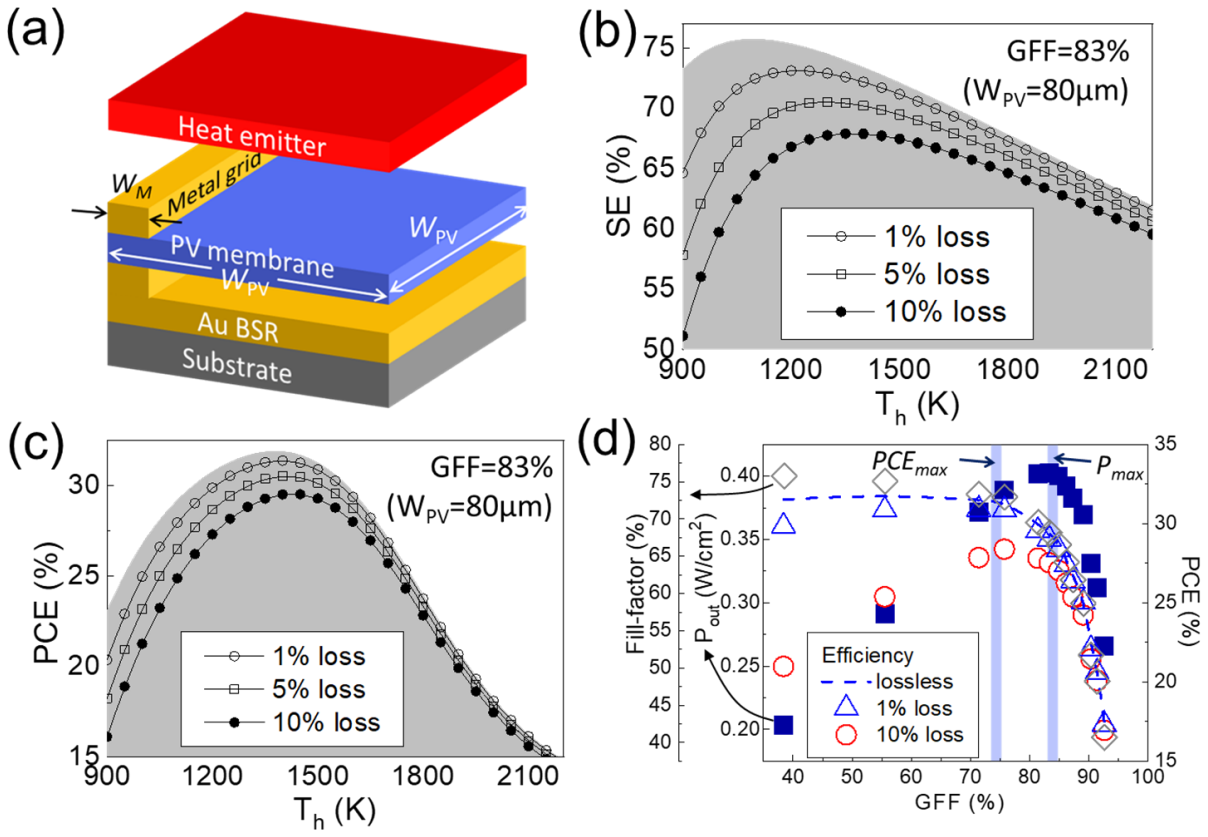

Figure 5.5 (a) Device geometry used to calculate the geometric fill factor (GFF). W_M is the metal grid width, and W_{PV} is the width and length of the device. As the cell size increases, the GFF identically approaches to the equation. (b) Spectral efficiency of the air-bridge InGaAs TPV calculated as a function of emitter temperature for W_{PV} = 80 μm and W_M = 8 μm. The shaded region indicates the limit to SE limit for the InGaAs AB-TPV structure in Ref. [1]. (c) PCE vs. T_h. The shaded region assumes perfect reflectivity of the metal grid lines. (d) Left-axis: Fill-factor (FF) (diamonds) and P_{out} (squares) using TCAD to model the InGaAs AB-TPV cell. Right-axis: Calculated PCE assuming R_{loss} = 1% (triangles) and 10% (circles). The dashed line is the practical efficiency limit assuming GFF = 100%.

Since $\varepsilon_{eff,M} < 1$, there are losses from light reflected from the metal surface. Figure 5.5(b) and 5.5(c) show the *SE* and cell efficiencies for 1, 5, and 10% reflectance losses by the gridlines, and GFF = 83% for the InGaAs AB-TPV cell in Ref.[1]. The edge of the shaded regions shows the limit of the InGaAs AB-TPV in [1]. The reflectance loss is particularly significant at low T_h.

Figure 5.5(d) illustrates the tradeoff between cell resistance and GFF using the TCAD simulated *FF*, P_{out}, and PCE. The dashed line is the calculated PCE at T_h = 1500 K corresponding to the upper limit of the SE in Fig. 5.5(b). The triangle and circle symbols are the PCE using the *SE* limited by reflectance losses by the gridlines of 1 and 10%. An optimal P_{out} is found at a GFF between 0.82 and 0.85.

5.4 Discussion

Figure 5.6(a) shows the PCE vs. T_h including the effects of different loss mechanisms discussed in Sec. II. The upper boundary shows the thermodynamic limit of the InGaAs AB-TPV efficiency with R_{OOB} = 100% and *EQE* = 100, where the maximum *PCE* = 57.2%. The InGaAs AB-TPV structure has the maximum EQE = 68%, resulting in the second boundary line with R_{OOB} = 100%, *EQE* = 68%, and *IQE* = 100%. The absorption oscillations in the OOB (see Fig. 5.4a) introduce "cavity loss". The dotted line indicates the boundary at R_s = 0, such that the yellow region indicates the ohmic losses. The design limit of the InGaAs cell assumes negligible R_c and SRH, and R_s = 12 mΩ·cm^2, leading to a maximum *PCE* = 48.6%. The upper boundary of the orange region is the maximum PCE in the absence of surface recombination, whose suppression is clearly critical to achieving high efficiency. The bottom solid line is for the InGaAs AB-TPV, where the red-dashed line indicates the InGaAs model with *VF* = 0.3 corresponding to the conditions used for the device indicated by the star [1]. The violet-colored region is the loss due to a contact resistance of $R_c = 2\times10^{-5}$ Ω·cm^2, with the loss becoming negligible for $R_c \leq 2\times10^{-7}$ Ω·cm^2. Among the different losses, surface recombination is the largest contributor.

Figure 5.6(b) shows the PCE limit (EQE = 1 and R_{OOB} = 100%) as a function of E_g and T_h. The dashed line addresses the maximum PCE vs. the normalized bandgap, E_g/kT, addressing that

the corresponding T_h decreases as the bandgap decreases. Figure 5.6(c) shows the dependence of the maximum PCE on R_{OOB} vs. E_g/kT_h for various R_{OOB}. A R_{OOB} decrease from 100% to 96% results in a reduced PCE for increasing bandgap. Larger bandgaps (E_g > 1.0 eV) are useful at high emitter temperatures (1900-2400°C) commonly found in low-cost thermal energy grid storage [54,184]. Recently, however, the efficient conversion of low-temperature heat to electricity has also become important [124]. The symbols represent published PCE results [1,54,89,170,185-191]. The air-bridge TPV cell (red-star) apparently has achieved the highest efficiency among single-junction TPVs. The large gap between current device performance and the radiative limit

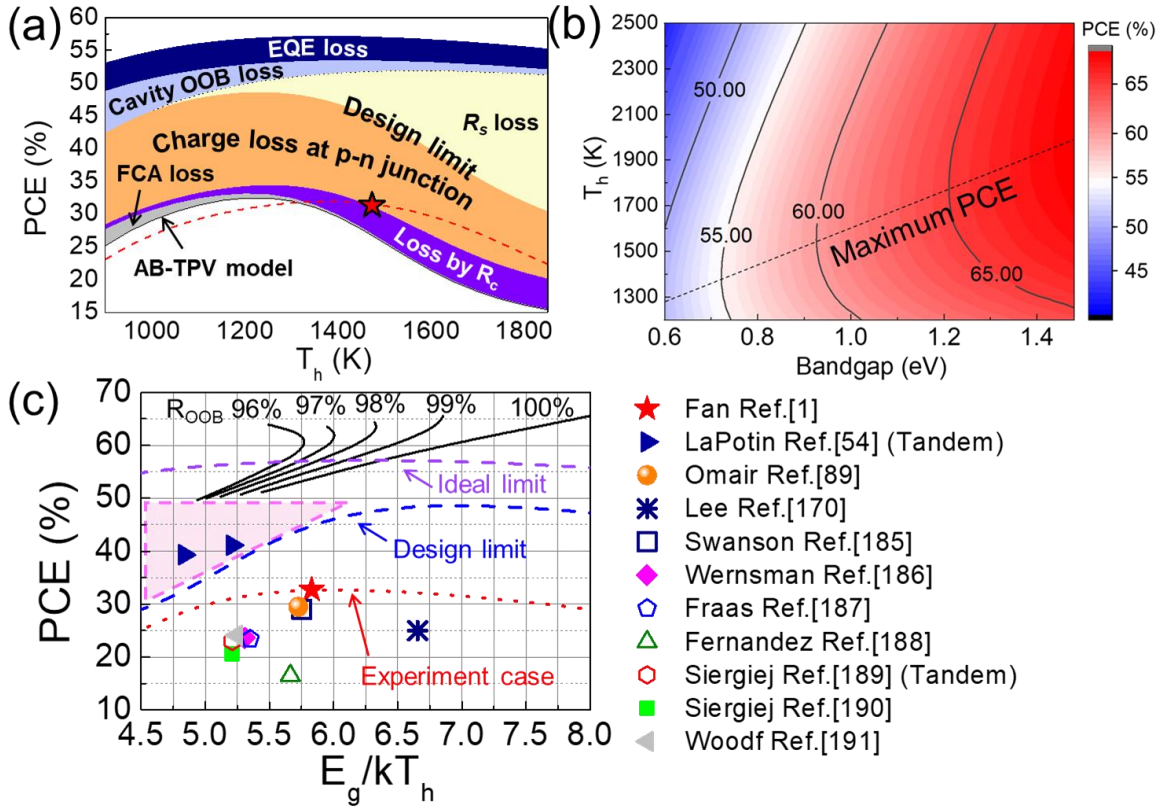

Figure 5.6 (a) Calculation of the air-bridge PCE limits with the relative effects of the various losses. The maximum PCE limit corresponds to *EQE* = 100% and R_{OOB} = 100%. The design limit corresponds to the case where the metal contact resistance (R_c) and junction recombination are negligible. The orange region includes loss from p-n junction recombination. The violet-shaded region is the power loss due to device contact resistance, and the grey-shaded region is due to FCA loss. The most bottom line indicates the model for the experiment InGaAs AB-TPV cell. The dashed line is the model for the device in Ref. [1] where VF = 0.3 and the red start from the literature. (b) Contour plot of the PCE at R_{OOB} = 100% with the radiative limit as a function of bandgaps and emitter temperatures. The dashed line is the maximum PCE. (c) PCE as a function of E_g/kT_h for prior results (symbols) from the literature. The top solid lines are the calculated maximum PCE with the radiative limit and various R_{OOB}. The bandgap (E_g) is varied from 0.6 to 1.4 eV. The dashed lines indicate the calculated PCE ideal and design limits for the InGaAs AB-TPV cell [1]. The dashed triangle indicates the ohmic loss by R_s.

suggests the possibility of still achieving considerably higher single-junction AB-TPV efficiencies, particularly if surface recombination is reduced.

5.5 Conclusion

We analyze the performance of InGaAs AB-TPVs cell by identifying various losses including FCA, non-radiative and ohmic losses, and metal grid shadowing. The free carriers in relatively high-doped semiconductors primarily lead to the loss of R_{OOB}. With ΔR_{OOB} = 2%, large bandgap semiconductors (e.g., Si and GaAs) become highly inefficient at low T_h. The largest PCE loss results from recombination at the semiconductor surface. The InGaAs diode model indicates the $v_{rec} < 2\times10^5$ cm/s leads to a voltage loss of 0.15V. By reducing the velocity to zero, it generates the design limit with the efficiency improvement of 12−17% at T_h = 900−2000 K. At T_h = 1400 K, the maximum radiative efficiency limit of an InGaAs AB-TPV is 55.5%. Tradeoffs between cell resistance and shadowing by the metal grid leads to an optimal InGaAs AB-TPV P_{out} for GFF = 84%. In conclusion, the voltage loss by surface recombination results in a significant fraction of efficiency loss compared to the practical PCE limit, implying that the p-n junction must be improved to reach even higher efficiencies than the highest performance single-junction AB-TPV cells reported to date.

Chapter 6 Summary and Future Opportunities

6.1 Summary of Present Work

An air-bridge TPV architecture allows high rates photon utilization by suppressing parasitic loss (Fresnel loss, SPP effect, and IR absorption by free carriers) at OOB wavelengths. To demonstrate air-bridge TPVs in a variety of applications, free-standing TPV membranes on air-cavities needs careful engineering considering output power of diodes, mechanical instability, and optical properties. Our work presented here is focused on the fundamental understanding of the compressive buckled III-V membranes, the design of InGaAs/InP thin-film membrane diode, the demonstration of air-bridge micro-TPV cells, a novel air-bridge tandem TPV architecture, and analysis of air-bridge TPV efficiency based on detailed balance.

As a result of Au-Au cold-welding, the thin-film TPV membrane supported by Au gridlines is compressively buckled owing to the Au plastic deformation and the change of internal pressure. The III-V buckled materials with ~1% deformation are mechanically unstable, thereby resulting in thin-film fractures and non-flat morphologies which distort refractive optical paths and has multiple cavity interference modes. This obstructs the high reflectance at the sub-bandgap region, therefore suppressing the buckled morphology is an important goal. The buckling is controlled by changing the spacing between the gridlines and the thin-film thickness (t_{tpv}). Using the previously reported TPV structure (t_{tpv} = 1.5 μm), compressive buckling forms micron-height upward-buckling at only a 100-μm gridline spacing. This can be planarized by increasing the t_{tpv} to > 3.5 μm.

Next, we engineer the thick InGaAs/InP structure with six different thin-film layers – p-InGaAs contact (0.1 μm), p-InP window (0.2 μm), n-InGaAs absorber (1 μm), n-InP surface-field (0.1 μm), n-InP buffer (1.9 μm), and n-InGaAs (0.1 μm) contact layers. Insertion of the n-InP buffer (1.9 μm, doping 10^{16}~10^{17} /cm^3, μ_e = ~5000 cm^2/V-s) suppresses the buckling by increasing the membrane stiffness approximately 13 times. The conductivity of the InP is high enough to eliminate a significant increase of R_s.

We design and demonstrate an air-bridge micro-TPV cell with an area smaller than 0.1mm^2. Using a laser-confocal microscope, we define that the buckling height is less than the measurement limit (10 nm). Under far-field radiative heat transfer, the electrical performance shows the highest FF 68 – 74%, R_{sh} > 20 kΩ-cm^2, and R_s < 10 mΩ-cm^2. The TPV efficiency records PCE near 30% under T_h = 1300 K using a SiC globar emitter. The FTIR measurement shows a remarkable improvement of sub-bandgap reflectance in comparison with the previously reported Au-BSR TPV [66]. The effective R_{sub} of the air-bridge TPV is 98.7% under 1300 K blackbody radiation, which is higher than the Au-BSR TPV (R_{sub} 95.3%).

A multi-junction TPV is a promising method for achieving high efficiency TPVs. However, conventional tandem PV structures have heavy doped TJs or quantum-well layers, which generate loss by IR absorption of free carriers. Therefore, we propose an air-bridge tandem TPV architecture, where the sub-cells in the tandem cell are electrically coupled by Au-Au cold welding. From the demonstrations, the InGaAs tandem TPV shows a high V_{oc} of 0.8 V, which is two times higher than a single junction InGaAs TPV. The novel tandem architecture allows the choice of different material partners without the restriction of epilayer growth on a common substrate. A four-terminal tandem architecture releases the PCE dependence on current matching, which is strictly required for a monolithic tandem TPVs. The 4-T air-bridge tandem structure is

enabled by inserting polyimide at the Au-Au bonding interlayer. Currently, the project is aiming to demonstrate PCE near 40% using a III-V quaternary tandem TPV cell with double air-bridge layers. Cost and high throughput are important to encourage the commercialization of TPV systems. Simultaneously, the main purpose of the tandem architecture is to broaden the selection of tandem materials partners. Therefore, the demonstration of an air-bridge tandem TPV cell using cost-effective materials rather than quaternary compound alloys is important to prove the true value of the concept.

Air-bridge thermophotovoltaic (AB-TPV) devices have demonstrated near-99% utilization of photons whose energy is less than the semiconductor bandgap (known as out-of-band, OOB, photons). Here, we determine 55.5% as the radiative efficiency limit at an emitter temperature of 1400 K for AB-TPVs based on detailed balance, which compares to a thus-far reported efficiency of 32%. A technology computer-aided design model for the InGaAs diode predicts that suppressing the surface recombination velocity to < 200cm/s significantly improves the open-circuit voltage and the shunt resistance, resulting in 48.6% as the practical efficiency limit. We find that a 1% OOB loss due to free-carrier absorption (FCA) in doped regions of the TPV can drastically decrease the efficiency at larger bandgaps and lower emitter temperature. The effects of shadowing by metal grids only introduce minor losses in TPV performance. Overall, achieving a defect-free p-n junction in a single-junction TPV device is important to realize higher power conversion efficiency than reported so far.

6.2 Future opportunities

6.2.1 Four-terminal Air-Bridge InGaAsP Tandem Thermophotovoltaic Cell

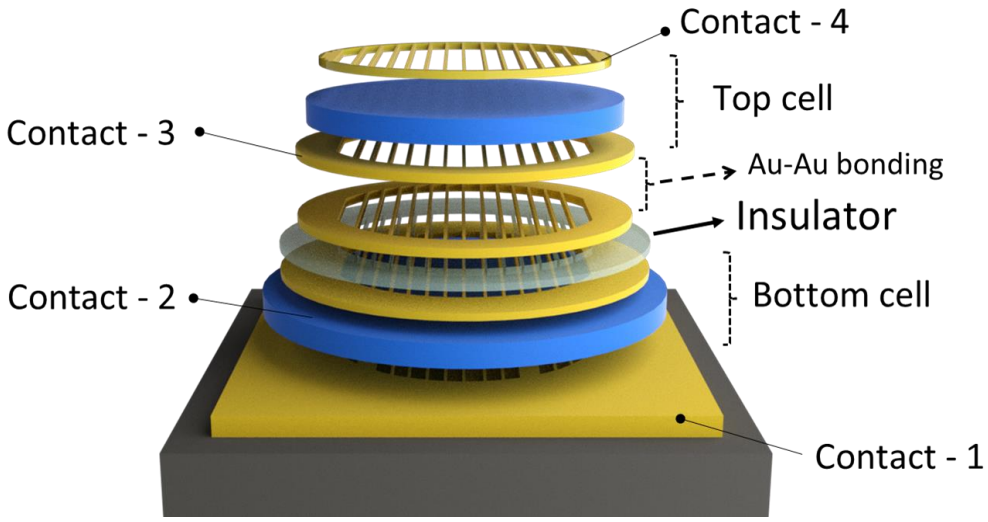

Figure 6.1 Schematic of four-terminal tandem structure by Au-Au cold welding between the top and bottom cells.

To demonstrate the 4-terminal structure, the interlayer includes an insulator thin film to block the electrical connection between the sub-cells. Silicon nitride (Si_3N_4) and silicon oxide (SiO_2) are good insulating materials. However, the materials with high-temperature process over 300°C deteriorate the performance of the InGaAs/InP diodes since the InP has the sublimation point at 350°C. Also, the high temperature processes can cause the mechanical destruction of TPV membranes. Instead of the solid materials, we adopt a polymer film. Figure 6.1 depicts the 4-terminal tandem structure. Most of fabrication processes follow the same method in Fig. 4.1 (2-terminal tandem structure), but the schematic includes an insulating film between the cells. At the Au-Au bonding interface, the top and bottom cells are aligned using a flip-chip-bonder (Finetech GmbH & Co. KG, Berlin, Germany). The aligned sample is moved to another conventional bonder chamber (EVG 520, EV Group, Austria) and the second bonding process is applied using 1 kN force at 150 °C for 10 min. After removing the InP handle wafer, the mesa TPV membranes are defined for the top and bottom cells. The top metal pads are patterned with the gridlines having

the spacing of 80μm. The final device configuration has four-terminal contacts as illustrated in Fig. 6.1.

Modeling of 4-terminal Hetero Tandem Thermophotovoltaic Cells

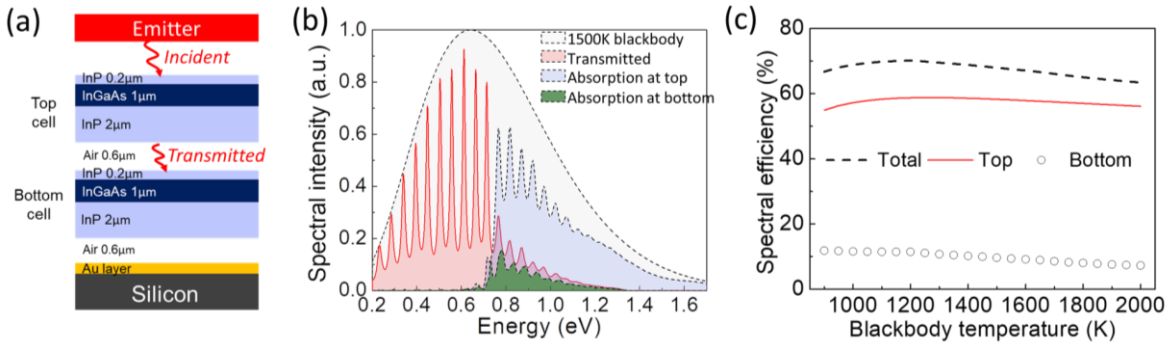

Figure 6.2 (a) Schematic of the tandem architecture with two sub-cells. The spectrum from the emitter is split to the sub-cells with 1-μm InGaAs. (b) Simulation of transmitted and absorption spectrum under 1500 K blackbody. The transmitted data means after subtracting the absorption and reflectance at the top cell from the 1500 K blackbody spectrum. All data was weighted by 1500 K blackbody spectrum. c) Calculation of spectral-efficiency as a function of blackbody temperature for the top, bottom, and tandem cells, respectively.

We are developing a 4 terminal (4T) air-bridge tandem structure, where the sub-cells have different bandgaps. The 4T tandem enables the parallel electric connection of the sub-cells, mitigating the high R_s degradation which occurs in the 2T tandem demonstration (Chapter 4). The spectral flux is split through the top and bottom cells. The SE of a solar 4T tandem PV is calculated by summing the SE of each cell following by:

$$SE_{4T\ tandem}=\frac{\left[\int_{E_{g,top}}^{\infty} EQE_{top}\times\Phi_{top}(E)dE\right]_{Top}+\left[\int_{E_{g,bottom}}^{\infty} EQE_{bottom}\times\Phi_{bot}(E)dE\right]_{Bot}}{\int_{0}^{\infty}\Phi(E)dE}, \quad (6.1)$$

where the *EQE* is the external-quantum-efficiency and the Φ is the spectral photon flux from illumination [159]. The Φ_{top} and Φ_{bottom} are the photon flux considering the spectral splitting

[72,192]. In TPV system, the effective emissivity from Eq (1.4) is combined to Eq (6.1), therefore, the SE at the 4T tandem is defined as:

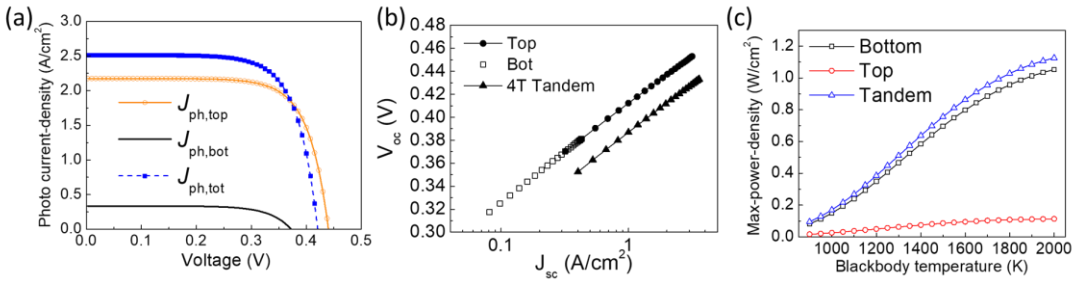

Figure 6.3 (a) Calculation of the top, bottom, and 4-terminal tandem J-V characteristics. The blackbody spectrum is 1500-K. An experimental dark-current from an air-bridge single InGaAs PV was used for the calculations. (b) Calculation of open-circuit-voltage (V_{oc}) and short-circuit-current-density (J_{sc}) as a function of blackbody temperature (900 – 2000K, ΔT=50K). (c) Calculation of the max-power-density as a function of blackbody temperature.

$$SE_{4T\ tandem}=\frac{\sum_{n=1}^{m}\left(E_{g,n}\times\int_{E_{g,n}}^{\infty}\varepsilon_{e,n}(E)\times A_{cell,n}\times\Phi_{n}(E)dE\right)}{\int_{0}^{\infty}\varepsilon_{e}(E)\times A_{cell}\times E\times\Phi(E)dE}, \quad (6.2)$$

where the $E_{g,n}$, $\varepsilon_{e,n}$, $A_{cell,n}$, and Φ_n indicate the bandgap, effective emissivity, absorption at PV, and spectral photon flux at the n_{th} sub-cell, respectively. To calculate the SE for the 4T tandem structure, Figure 6.2 (a) schematically illustrates the spectral splitting in the InGaAs homo-tandem cell having two sub-cells. Figure 6.2 (b) shows the four-power distribution: 1500 K blackbody, transmitted spectrum passing through the top cell, and absorption spectrum at each cell. The heat radiation from 1500 K is absorbed through the sub cells, and the SE_{bot}, SE_{top}, and $SE_{4T,\ tandem}$ are calculated as shown in Fig. 6.2 (c). The $SE_{4T,\ tandem}$ is calculated by summing the SE of the sub-cells as expressed in Eq (6.2). The InGaAs tandem structure does not consider the current-matching condition, resulting in the SE of the bottom cell being relatively small compared to the top cell.

We calculate the $J_{ph,top}$ and $J_{ph,bot}$ using the Eq (4.1) and the data in Fig. 6.2(b). Figure 6.3 (a) shows the graphs of the J_{ph} at each sub-cell and the 4-t tandem, where the J_{ph} of the 4T tandem is calculated by summing the J_{ph} from each sub-cell. Figure 6.3 (c) plots the calculated maximum power point (P_{mpp}) as a function of the emitter temperature. Regardless of the temperature, the P_{mpp} is higher than each sub-cell, where the sub-cells are not current-matched.

Measurement and Calculation of 4-terminal Tandem Photovoltaic Cell.

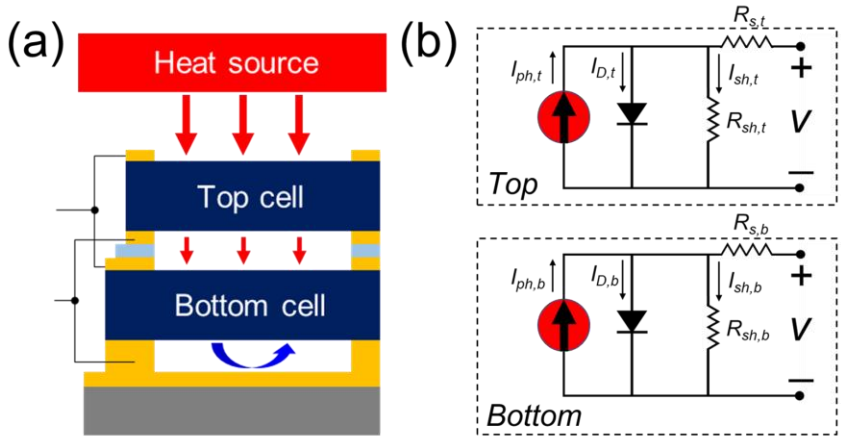

Figure 6.4 (a) Schematic of the mechanically stacked double-air-bridges tandem thermophotovoltaic structure. In the demonstration, the 4-terminal contacts are paired as depicted in the illustration. (b) Equivalent circuit diagram of the 4-terminal tandem diode model with the independent operation. The photocurrent components at the top ($I_{ph,t}$) and bottom ($I_{ph,b}$), the series-resistance (R_s), and the shunt-resistance (R_{sh}).

The 4T tandem TPV cell can be measured by the four-probe configuration. As illustrated in Fig. 6.4 (a), the cathodes and anodes from each cell are electrically paired and have two probing contacts. Figure 6.4 (b) schematically shows the electric-circuit equivalent of the two cells. Both cells generate the top ($I_{ph,t}$) and the bottom ($I_{ph,b}$) photo currents, respectively. Therefore, the total output power density of the cell is summed by the P_{out} of each sub-cell following by:

$$P_{out}=\sum P_{out,subcell}, \tag{6.3}$$

resulting in higher output power than the single TPV cell. Depending on the metal contact configurations, the tandem architecture offers the opportunity to operate the bottom and top cells independently, or it can be functional as a 3T TPV cell.

Hetero-tandem Thermophotovoltaic Demonstration.

In this project, our focus is to develop a reliable approach for an air-bridge tandem TPV architecture. This technique can be extended to hetero-tandem architectures using InGaAsP/InGaAs [71], GaSb/InGaAsSb [70], Si/III-V [163,193], and InGaAsP/InGaAsP (different bandgaps). In future, our group aims to demonstrate a hetero-tandem TPV cell, where InGaAsP alloys with different compositions (see Table 6.1) are possible tandem partners. Using the TCAD method described in Chapter 5, we build the material database for InGaAsP and simulate the electrical and optical performance. The material physics parameters are calculated using the linear interpolation from conner (InAs, InP, GaAs, GaP) and side (InGaAs, InGaP, InAsP, GaAsP) materials. For example, the bandgap is calculated using E_g = [x×(1-x)×(y×E_g($Ga_xIn_{1-x}As$)+(1-y)×E_g($Ga_xIn_{1-x}P$))+y×(1-y)×(x×E_g($GaAs_{1-y}P_y$)+(1-x)×E_g($InAs_yP_{1-y}$))]/[x×(1-x)+y(1-y)]. A TPV cell is a blackbody with room-temperature and the dark current is defined by [171]:

$$J_D = \frac{q}{4\pi^2 c^2}\int_{E_g}^{\infty} \omega^2 \cdot e^{\left(\frac{\hbar\omega}{k_B T_c}-1\right)^{-1}} d\omega. \tag{6.4}$$

With the assumption that $E_g \gg kT_c$, the equation is simplified to:

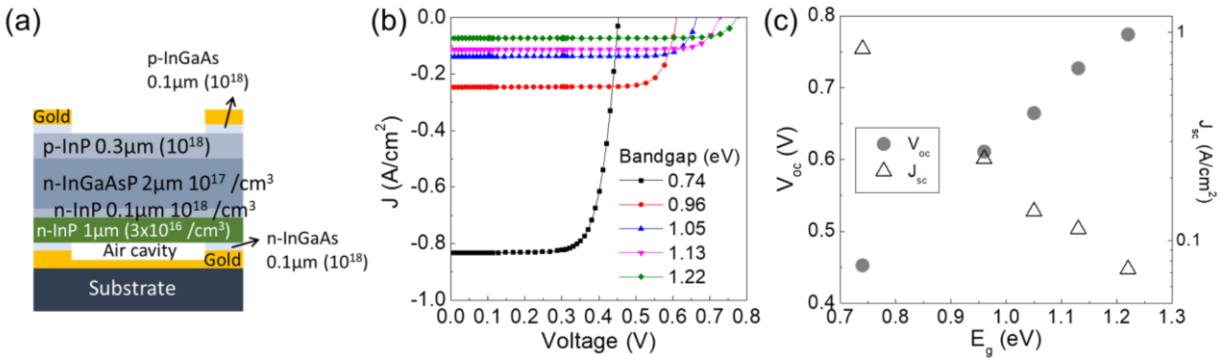

Figure 6.5 (a) Schematic for the InGaAsP single-junction air-bridge TPV cell. (b) J-V curves as a function of the bandgap with different InGaAsP alloys. (c) V_{oc} and J_{sc} extraction as a function of the bandgap.

$$J_D = \frac{q}{4\pi^2 c^2 \hbar^3} e^{(-E_g/k_B T_c)} \times \left[E_g^2 k_B T_c - 2{k_B}^3 T_c^3 \times \left(\frac{E_g}{k_B T_c} - 1 \right) \right]. \quad (6.5)$$

As increasing the bandgap, the J_D and J_{ph} are decreased. Given a bandgap, V_{oc} is determined by the temperature difference between a cell and a heat source. Using the 1900 K blackbody spectrum with a blackbody power, Figure 6.5 shows the TCAD simulation results for *J-V* characteristics. In future, the material database for InGaAsP quaternary compounds in the TCAD suite can be manually updated based on experiment data.

Table 6.1 $Ga_xIn_{1-x}As_yP_{1-y}$ alloy compositions and bandgaps.

x	y	Bandgap (eV)	Lattice constant (Å)	Lattice mismatch to InP (%)
0.47	1	0.74	5.8680	-0.012
0.31	0.67	0.96	5.8690	0.005
0.24	0.52	1.05	5.8687	0.000
0.17	0.37	1.13	5.8687	0.001
0.1	0.22	1.22	5.8690	0.006

Cost-effective Air-bridge Tandem Thermophotovoltaic Cell

III-V ternary and quaternary compound materials have a merit to tune a bandgap. However, lattice-matched epitaxial growth accounts for a large portion of the cost in III-V devices, which is driven by low throughput and precious materials, raising costs when compared to relatively inexpensive materials and binary compounds such as silicon, Ge, and GaAs. Therefore, a tandem TPV cell comprising such materials can provide a route to realize cost-effective tandem TPV cell manufacturing. Figure 6.6 shows possible tandem partners using silicon, binary compounds, and ternary compounds. However, this research requires a fundamental understanding of the efficiency map for a tandem cell (two junctions) as a function of top and bottom bandgaps, emitter temperatures, and R_{OOB}.

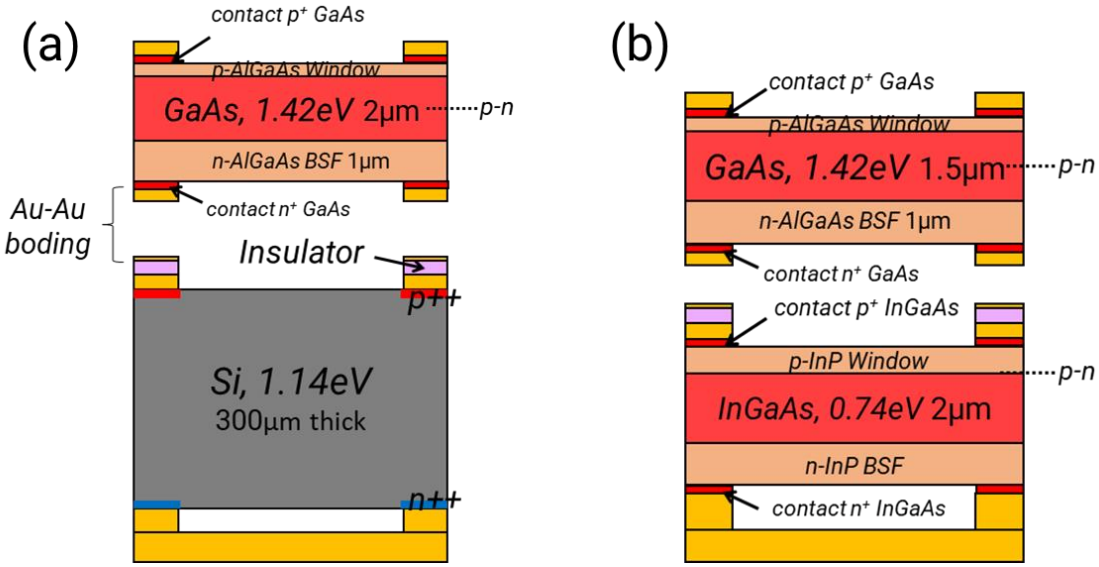

Figure 6.6 Double air-cavities tandem TPV cells for the tandem partners of (a) GaAs/Si and (b) GaAs/InGaAs, respectively. Note that the absorber thicknesses are arbitrary.

6.2.2 Towards portable, high-power, and high-efficient μ-TPVs

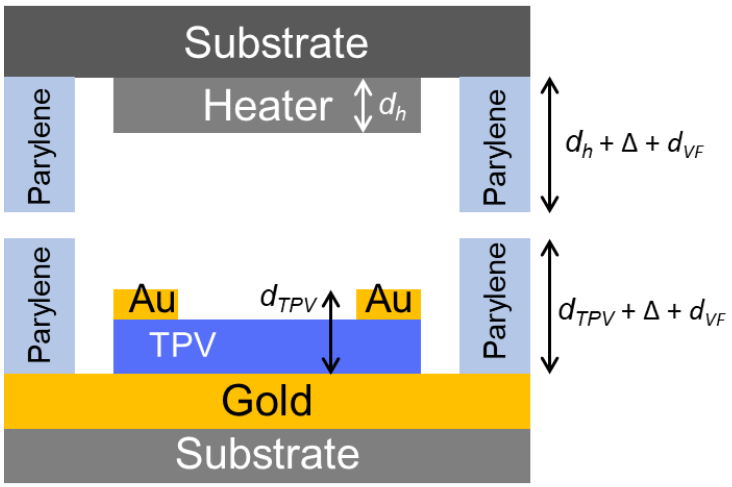

Figure 6.7 Schematic of a heater and a TPV cell with patterned parylene columns. The d_h and d_{TPV} are the thicknesses of the heater and the TPV, respectively. The Δ means the compressed parylene thickness during the bonding. The d_{VF} is the required distance for a high view-factor (VF) formed by the cavity between the heater and the TPV cell.

In Chapter 3, we demonstrated and characterized the air-bridge InGaAs TPV cells. The size is smaller than 0.07 mm^2 and it shows 18–30 % efficiency with T_h = 950–1400 K. It demonstrates the feasibility of the air-bridge architecture for a compact TPV application. Some researchers reported 10% or less efficiency μ-TPV cells [63,64]. In the micro-TPV systems, the effective efficiency is calculated by considering the diode performance and the heat emission efficiency. Theoretically, the authors predict 30% or higher efficiency. Therefore, the integration of an air-bridge μ-TPV cell with a high-efficient heat source can promise a high-efficient micro-power generator.

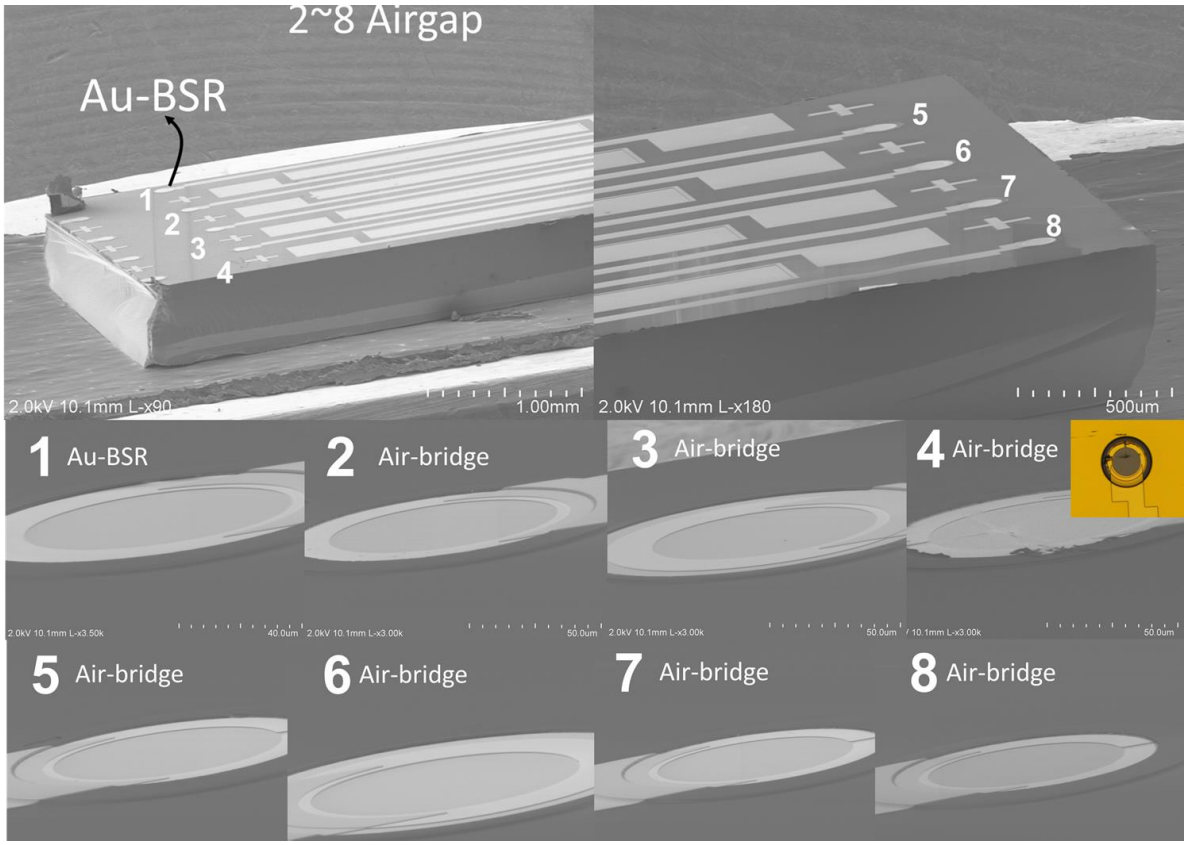

Figure 6.8 SEM images observed on a chip having the air-bridge TPV cells. '1' is an Au-BSR TPV cell. '2' to '8' indicate the air-bridge TPV cells.

To realize this goal, there are many challenges such as mechanical pairing of a micro-heat-source and an air-bridge TPV cell. In Chapter 4, we demonstrated the air-bridge tandem cell, where the sub-cells were optically aligned between Au-grid patterns and bonded by cold welding. Instead of the Au-Au bonding, we also developed parylene grid bonding using the same method. Figure 6.7 shows a concept to illustrate how to integrate a TPV cell and a heat engine. For the demonstration of a chip-scale air-bridge TPV system, the heater can be a Si or SiC emitter. The view-factor is higher than 0.8 at the gap (between the TPV and the heater) < 10μm. Therefore, d_{VF} (the distance between the emitter and the cell to form a high view-factor) can be 5μm or less. The Δ (compressed thickness by bonding) can be a variable as a function of bonding force. Therefore, it needs to be measured experimentally. The TPV substrate is linked to a heat sink, thereby keeping

the cell to a reference temperature, 293K. The empty space between the emitter and the TPV cell can be air or vacuum.

Under near-field radiation, the TPV operation exhibits high power density enabled by evanescent wave coupling, surpassing the far-field blackbody radiation limit between planar surfaces [50,66-68]. A non-buckled air-bridge TPV cell promises a constant nanogap proximity close to an emitter. For the demonstrated air-bridge micro-TPV cells (Chapter 3), the flatness of the membrane has been observed by SEM (Fig. 6.8), 3D microscope, and surface profilometry. In addition, the non-buckled TPV cell is nondestructive to high temperature (no deformation by passivation process performed at 200 ℃) or RF plasma treatment. With the fundamental understanding of the non-buckled membrane formation, our demonstration can give a solution to explore the first 20% efficiency of TPV using NFRHT.

6.2.3 Centimeter-scale Air-Bridge Thermophotovoltaic Cells

The practical performance of TPV devices is strictly affected by TPV size and the TPV system configuration involving a heat source and a TPV cell. As the size increases, the view-factor approaches unity, allowing for a high output power. Simultaneously, the demonstration of a large TPV cell is important to realize the potential of commercial TPV panels. The resistance of a TPV cell consists of R_{PV}, R_M (metal resistance), and R_c (metal contact resistance). In Chapter 5, the design limit of R_S can be 12 mΩ-cm^2 for an InGaAs TPV cell where the R_c and R_M are negligible. Figure 6.9 shows the relationship between the R_s and R_M as a function of TPV size. The line indicates where the R_M is the same as the R_s, suggesting that the metal thickness should be greater than the data in the line at a given TPV size. Figure 6.10 shows the simulation results of heat transfer from a 1600 K heat source to an InGaAs TPV cell; we used a finite-element-analysis

method (COMSOL Multiphysics). In Fig. 6.10 (a), as the TPV size increases, the GFF is saturated at 89%, where the airgap spacing = 80μm, the metal grid width = 10μm, and the metal outer frame has a 20μm width. The GFF is nearly saturated when the TPV area is greater than 0.3 cm^2, implying that the discontinuous heat conductivity between metals and air becomes negligible in terms of the TPV surface temperature under thermal illumination. As shown in Fig. 6.10 (b) to (e), we varied the TPV area from 2.88×10^{-4} cm^2 to 0.22 cm^2 and the results show negligible minimum to maximum temperature changes. In an experimental set-up, the TPV cell temperature is maintained by a cooling stage at the back surface. During the simulations, the back surface of the TPV cell was cooled to 293K.

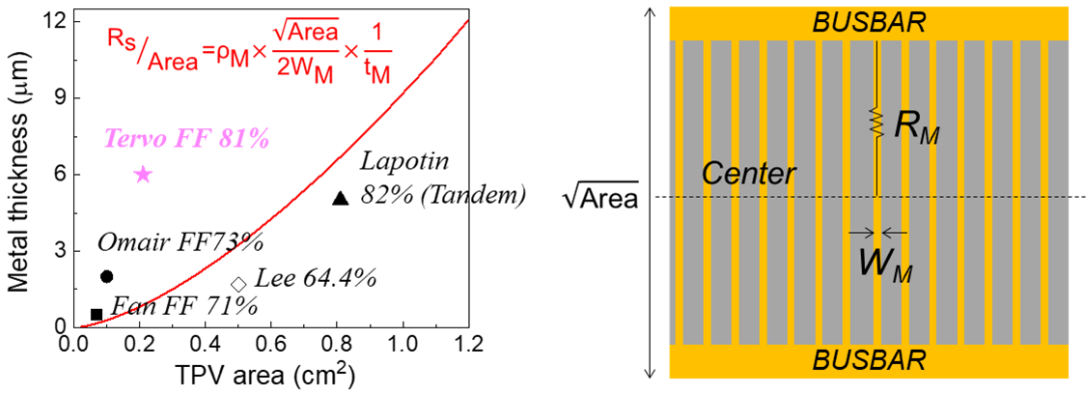

Figure 6.9 Calculation of TPV areas and the metal gridline thicknesses where R_s (Semiconductors) = R_M (Gridlines resistance). Assume that the metal contact resistance is negligible. The data line follows the equation to the inset, where R_s is the design limit (in Chapter 5), 12 mΩ-cm^2, ρ_M is the metal conductivity (Au: 2.2×10^{-6} cm-Ω), W_M is the metal grid width (10μm), A_s is the airgap spacing (80μm) and t_M is the thickness of metal grids.

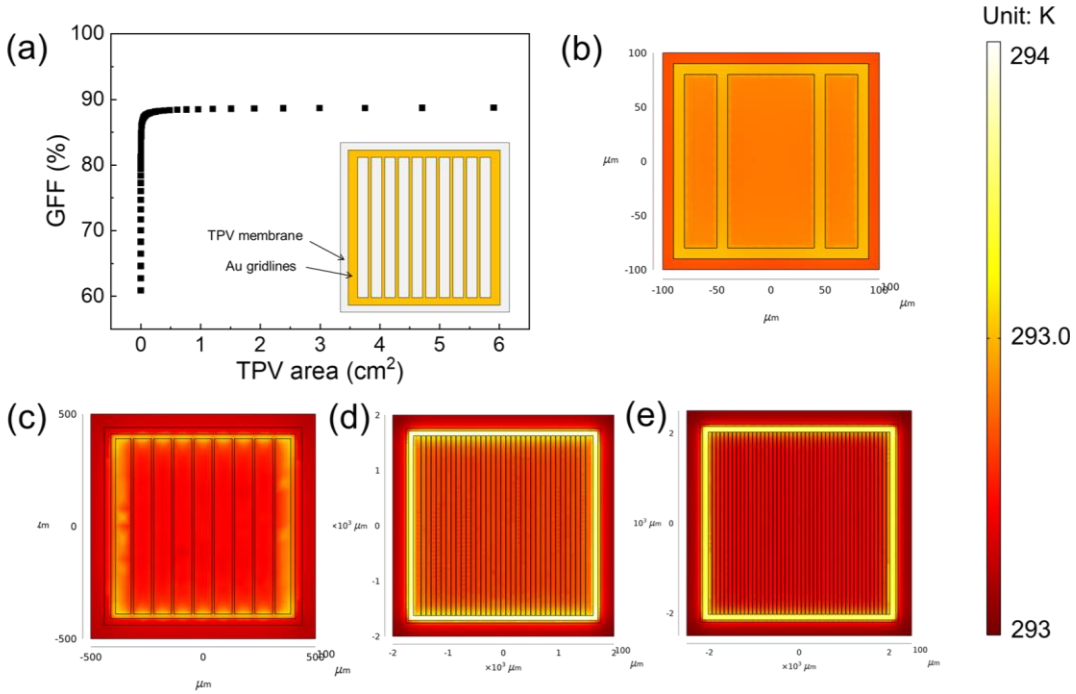

Figure 6.10 (a) Calculation of geometric-fill-factor of air-bridges as a function of TPV area. Finite-element-analysis of TPV temperature of TPV areas (b) 2.88×10^{-4} cm^2, (c) 8.50×10^{-3} cm^2, (d) 1.41×10^{-1} cm^2, and (e) 2.20×10^{-1} cm^2. We couldn't simulate 1 cm^2 or larger sizes owing to the constraint of 32 GBytes of memory. The heat transfer coefficient between a heat source to the TPV surface is assumed to 70 $W/(K\cdot m^2)$, where the gap between them is assumed to 1mm. The heat temperature was fixed to 1600K.

Appendix

A1. Understanding and Control of Compressively Buckled Semiconductor Thin Films

Note 1. Principal and compressive stresses

3D stress elements are represented by the 3×3 matrix stress tensor:

$$\sigma = \begin{bmatrix} \sigma_{xx} & \tau_{xy} & \tau_{xz} \\ \tau_{yx} & \sigma_{yy} & \tau_{yz} \\ \tau_{zx} & \tau_{zy} & \sigma_{zz} \end{bmatrix} \xrightarrow[\text{Eigenvalue}]{} \begin{bmatrix} \sigma_1 & 0 & 0 \\ 0 & \sigma_2 & 0 \\ 0 & 0 & \sigma_3 \end{bmatrix} \quad \text{(A1)}$$

where σ_{xx} (or σ_x), σ_{yy} (or σ_y), and σ_{zz} (or σ_z) are the normal stresses acting on the face identified by the subscripts, and the τ components indicate the shear stresses with the first and second subscripts denoting the face and its direction, respectively. The three stress elements along the *x*, *y*, and *z*-axes lead to the symmetric matrix at the left-hand side in Eq. A1. The eigenvalue transforms the symmetric tensor to the orthogonal set of principal axes, thereby defining principal stresses, where σ_1 is the tensile stress, σ_2 is the shear stress, and σ_3 is the compressive stress. During bonding, the shear stress is negligible. The compressive stress is higher than the tensile stress, thereby determining the stress of the buckling.

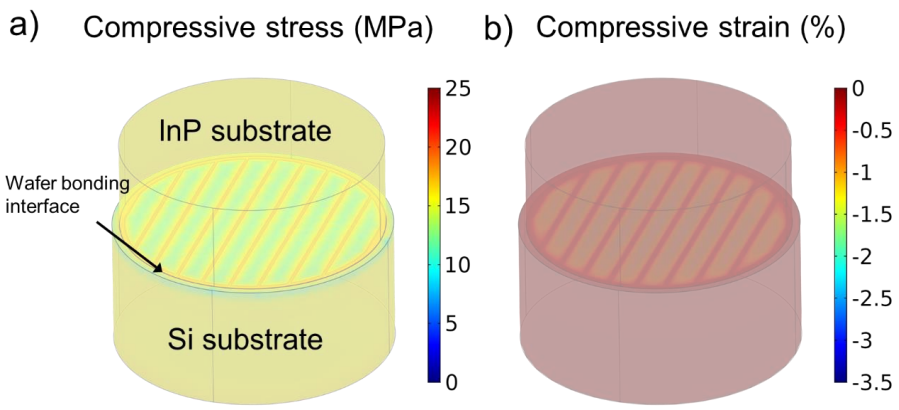

Figure A1. 3D finite-element-analysis simulation. Finite-element-analysis modeling structure to simulation bonding process.

Note 2. Extraction of Young's modulus (E_y)

$$\frac{1}{E_r} = \frac{(1-v_t^2)}{E} + \frac{(1-v_i^2)}{E_i} \tag{A2}$$

where E_r is the reduced modulus, E_i is Young's modulus of the indenter (1140 GPa), v_i is the indenter's Poisson ratio (0.07), and v_t is the III-V Poisson ratio (0.33).

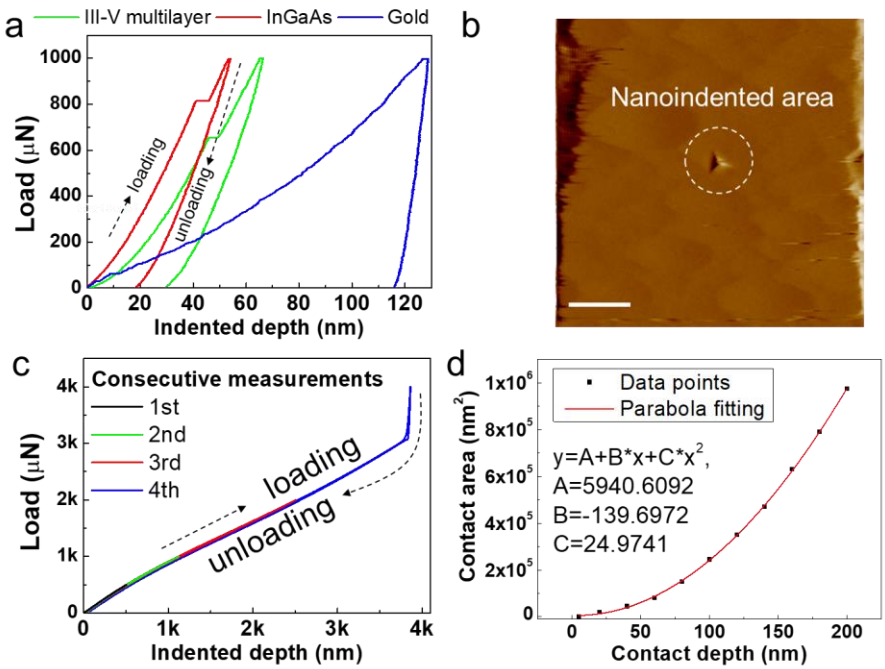

Figure A2. Nanoindentation measurement and Young's modulus extraction. **(**a) Load-displacement curves by nanoindentations on thin films using a Berkovich diamond nanoprobe tip with the radius of 50~200 nm. Film thicknesses: III-V multilayers (ML) of InGaAs(0.1 μm)/InP(0.1 μm)/InGaAs(1.0 μm)/InP(0.2 μm)/InGaAs(0.1 μm), InGaAs of 2.7 μm, and Au of 500 nm. (b) Representative atomic-force-microscopy image of a nano-indented region. The scan size is 20 μm × 20 μm. Scale bar, 4 μm. (c) Load-displacement curves by nanoindentation on the buckled region with gridline spacing = 100 μm. The consecutive tests were performed in the same position by increasing the loading force until the thin film touches the bottom Au surface. (d) Nanoindentor contact area versus the contact depth.

Note 3. Buckling simulations

Figure S3(a) shows the 3D structure used to simulate buckling III-V microstructures. The bottom is the Si substrate, where the displacement of the bottom boundary is fixed for the simulations. The 500-nm-thick gold layer / 500 nm gold gridline layer / 1.5 μm III-V layer are

stacked on the substrate. To simulate the structure, a uniaxial compression force is applied to the Au-gridline layer as shown in Fig. A3(c). Figure S3(d) indicates the cavities between the gold gridlines. The air inside is treated as an ideal gas. Therefore, the internal pressures are defined in the cavities. The internal pressures are numerically adjusted to fit the buckling heights to the experiments. Finally, the buckling is simulated as shown in Fig. A3(e). Here the gridline is deformed by the axial compression force of the 70 N in the *z*-direction. The internal pressures in the air cavity are 0.29 MPa and 0.55 MPa, at the three center cavities and the both side-end cavities, respectively.

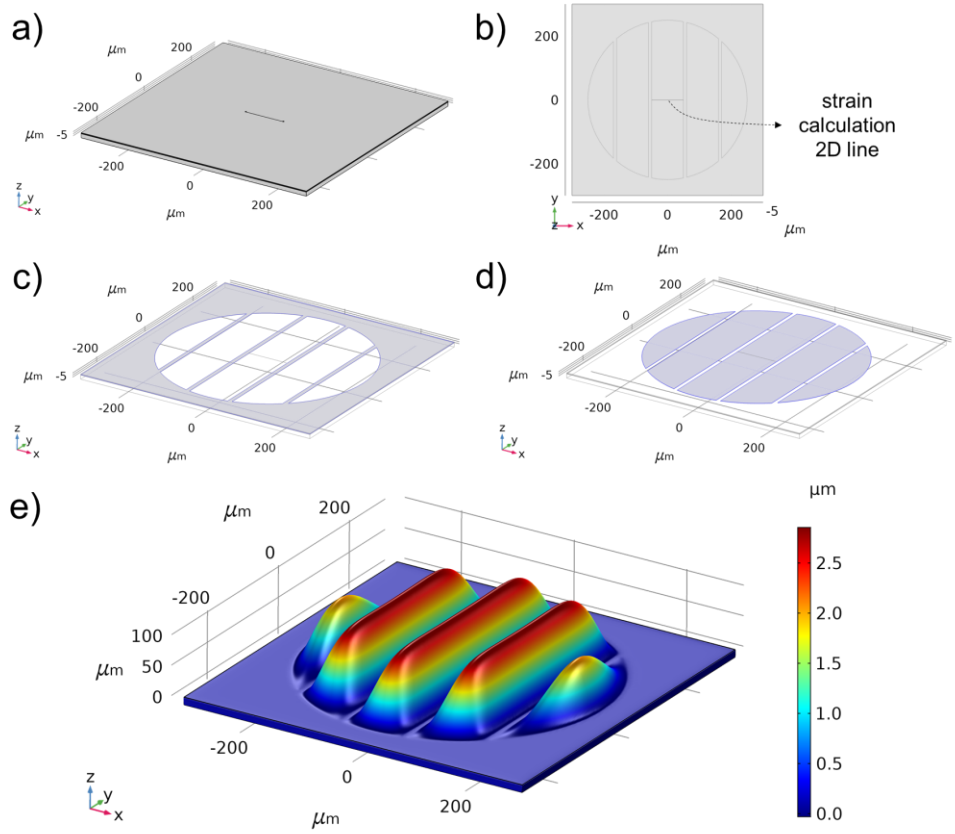

Figure A3. 3D finite-element-analysis buckling simulation. **(**a) 3D modeling structure with the gold gridline spacing of 100 μm. The circle diameter is 0.5mm. The size of the structure is 500×500 μm^2. The displacement of the boundary at the substrate is constrained to zero. The solid line at the center is for simulating structural deformations such as principal strains, principal stresses, and total displacements. (b) The top view of the modeling structure. (c) The gold gridline is chosen to apply uniaxial compression force in the *z*-direction. (d) The air cavities are defined between the gold gridlines. The air is treated as an ideal gas. Then, the internal pressures are applied to the boundaries inside the areas. (e) Buckling simulation result. The color legend indicates the vertical displacement. The experimental result is shown in Fig. A5.

Note 4. Gaussian fitting and strain calculations

The Gaussian function is provided by Eq. (2.2) in Chapter 2. The buckling height (h_b) is zero at the end of the beam structure. Thus, solutions when the height is zero give the min-max x_0 of:

$$\pm x_0 = \pm w \times \sqrt{-2ln\left(-{}^{h_0}/_{A}\right)} \tag{A3}$$

where $x_c = 0$ and $h_b = 0$ (h_0 is a constant to define the zero height from the Eq. A3). The strained lengths (l_s) are given by:

$$l_s = \int_{-x_0}^{+x_0} \sqrt{1+\left({}^{dh}/_{dx}\right)^2}\, dx = \int_{-x_0}^{+x_0} \sqrt{1+\frac{A^2x^2}{w^4}e^{\left(-\frac{x^2}{w^2}\right)}}\, dx \text{ where } {}^{dh}/_{dx} = -A\frac{x}{w^2}\times e^{\left(\frac{-x^2}{2w^2}\right)} \tag{A4}$$

The strain is calculated by the ratio of the strained (L_s) to the initial length ($L_i = 2x_0$). The initial lengths are assumed by 20.32, 28.97, 48.37, 68.51, 97.13, and 146.65 μm for the grid spacing = 20, 30, 50, 70, 100, and 150 μm, respectively. The calculated strain is a sensitive function of

measurement accuracy. For instance, assume that $\Delta L = L_s - L_i = 0.2$ μm (where $L_i = 100$ μm), which results in the strain, $\varepsilon = 0.2\%$. For measurement errors ≤ 4 nm, an accuracy of 99.998% is required to predict the strain to the second decimal place. The required accuracy increases as the L_i is reduced.

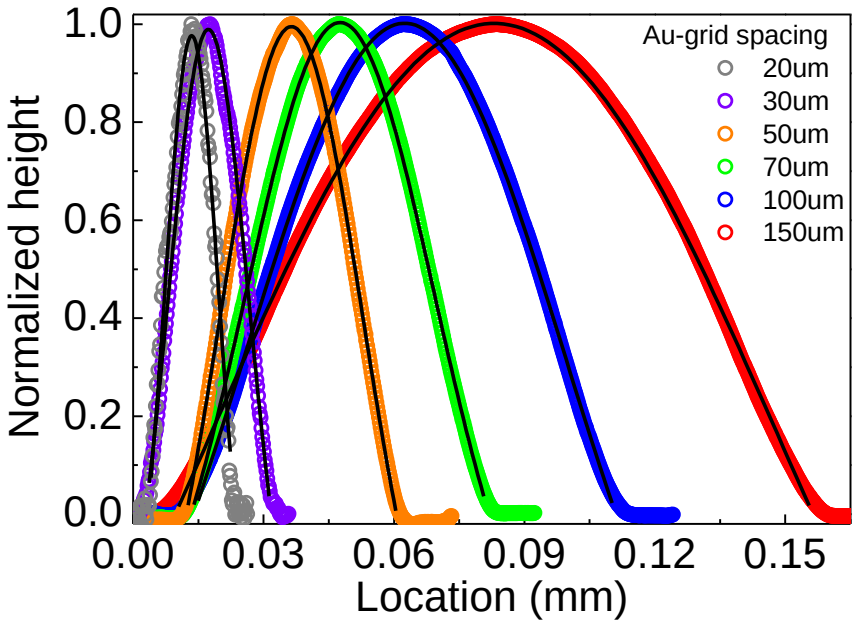

Figure A4. Gaussian profile of the buckled metamaterial. Gaussian fitting to the normalized profiles for different Au-grid spacings are shown by the solid lines. The colored dot plots indicate the experimental data.

Note 5. Scalability of buckled metamaterials

The scalability of the buckled metamaterials is demonstrated by varying the Au-gridline spacings. The buckled morphologies were scanned by stylus profilometry.

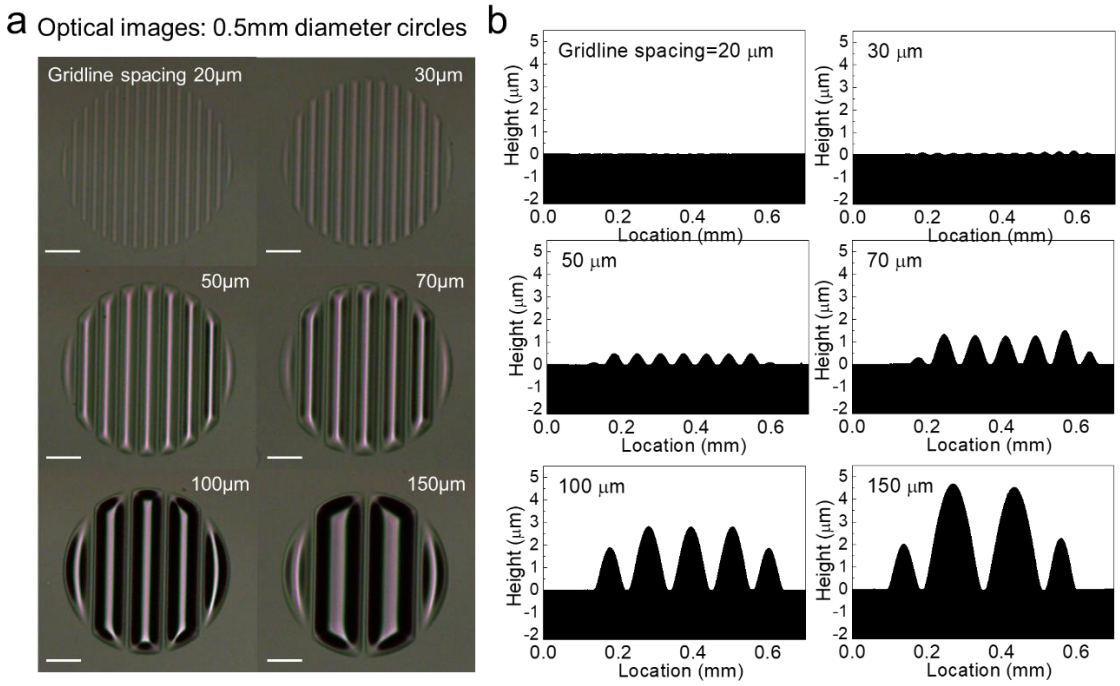

Figure A5. Buckling and profilometry measurements on 0.5 mm diameter circles. (a) Optical microscope images of buckled metamaterials. Scale bars, 100 μm. (b) Profilometry measurements of the surfaces in (a).

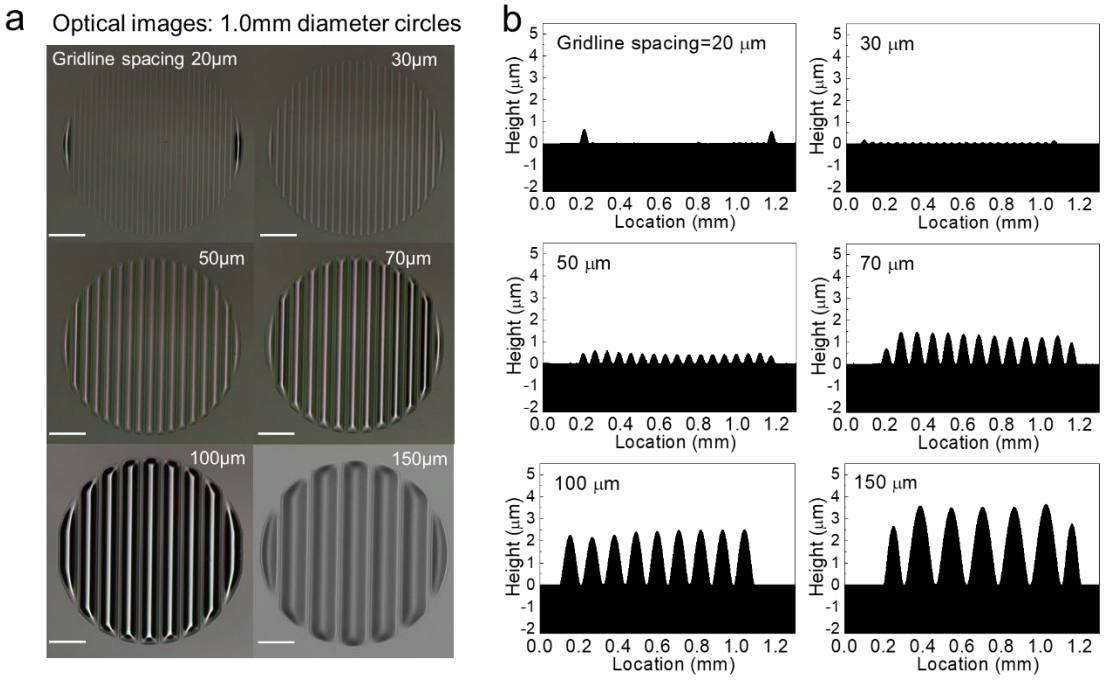

Figure A6. Buckling observation and profilometry measurement of 1.0 mm diameter circles. (a) Optical microscope images observations of buckled metamaterials. Scale bars, 200 μm. (b) Profilometry measurements of the surfaces in (a).

Note 6. Thickness dependent buckled morphology

The scalability of the buckled metamaterials is demonstrated by varying the epilayer thicknesses. The Au-gridline spacing is 100 μm. The buckled morphologies were scanned by stylus profilometry.

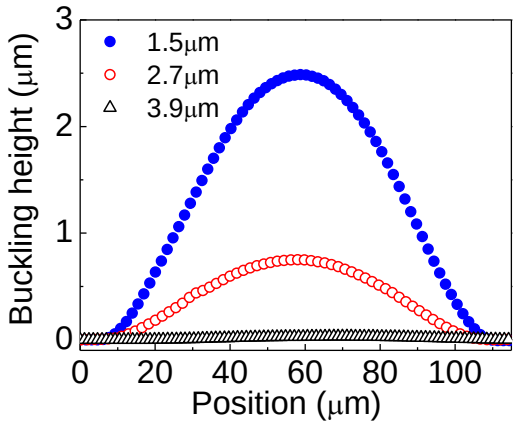

Figure A7. Profilometry measurements of buckled epilayers with different thicknesses.

.

Note 7. Buckling modes

Buckling modes using Euler-Bernoulli beam theory given at moment equilibrium are:

$$\sum_x M = M(x) + P\omega = 0 \tag{A5}$$

where $M(x)$ is the bending moment in the beam, P is the loading force, and ω is the finite deflection. From the curvature deflection relationship, Eq. (2.1) leads to:

$$E_t I_t \frac{\partial^2 \omega}{\partial x^2} + P\omega = 0 \tag{A6}$$

where E_t is the elastic modulus of the thin film and I_t is the centroidal moment of inertia for the cross-sectional region of the beam structure. The eigenvalue ($\omega = e^{\lambda x}$) determines a solution of Eq. (A6), with eigenfunctions for the buckling mode:

$$n\pi = \sqrt{\frac{P_{cr}}{E_t I_t}} \times l_t \tag{A7}$$

where the l_t is the Au-grid spacing (W_g), and n determines the mode.

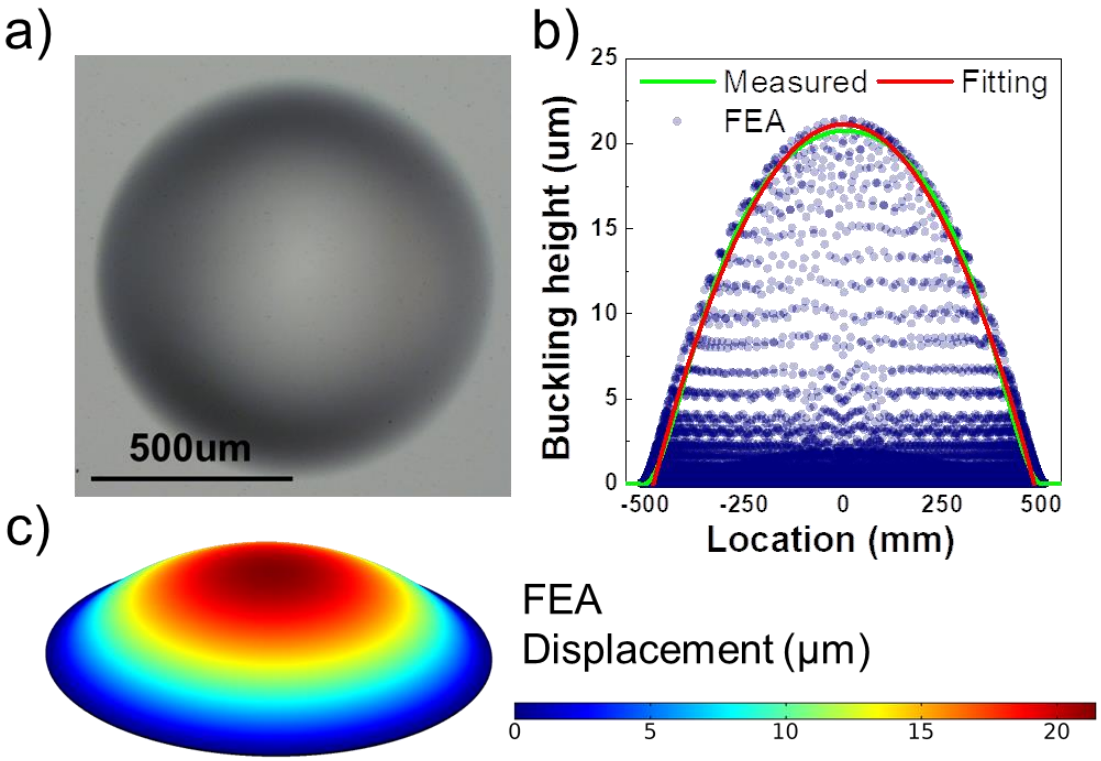

Figure A8. (a) Optical observation of a dome-like III-V buckling generation in a circle without metal grid patterns. (b) Shape measured by profilometry (green-solid-line), Gaussian fit (red-solid-line), and the simulation result (violet-circle-dot). The simulation includes the displacement data for the 3D modeling structure (InGaAs, air-spacing, and Au). (c) The FEA result at the bottom shows the post-buckling prediction.

Table A1. Gaussian fitting parameters using the profilometry measurements in Fig. A4.

W_g (μm)	Full width at half maximum	h_0	A	x_c	W
20	0.0145	-0.34	1.3096	0.0135	0.0061
30	0.0220	-0.43	1.4178	0.0173	0.0094
50	0.0385	-0.50	1.4943	0.0364	0.0163
70	0.0511	-0.41	1.4096	0.0476	0.0217
100	0.0870	-0.73	1.7331	0.0625	0.0370
150	0.1567	-1.20	2.2019	0.0830	0.0666

Table A2. Parameter extraction using Euler's buckling formula and the measured profiles for different Au gridline spacings. W_g = Au gridline spacing (beam length), W_{eff} = Effective beam length, λ = Wavelength of modes, P_{cr} = Critical load, and σ_{cr} = Critical stress.

Buckling mode (n)	III-V thickness (μm)	W_g (μm)	W_{eff} (μm)	λ (μm)	P_{cr} (N)	σ_{cr} (Pa)
1	3.9	100	69.0	138.1	0.485	122.3M
1	2.7	100	64.6	129.2	0.166	62.6M
1	1.5	20	12.4	24.8	0.806	0.54G
		30	19.0	38.0	0.343	0.23G
		50	32.4	64.8	0.118	78.8M
		70	42.9	85.8	0.067	44.9M
		100	70.6	141.1	0.025	16.6M
		150	124.2	248.4	0.008	5.36M
2	0.7	100	34.4	68.8	0.050	67.6M

A2. Air-Bridge TPV Cell Surface Temperature under Radiative Heat Transfer

Calculation of Heat Conduction from Hot-Emitter to Photovoltaic

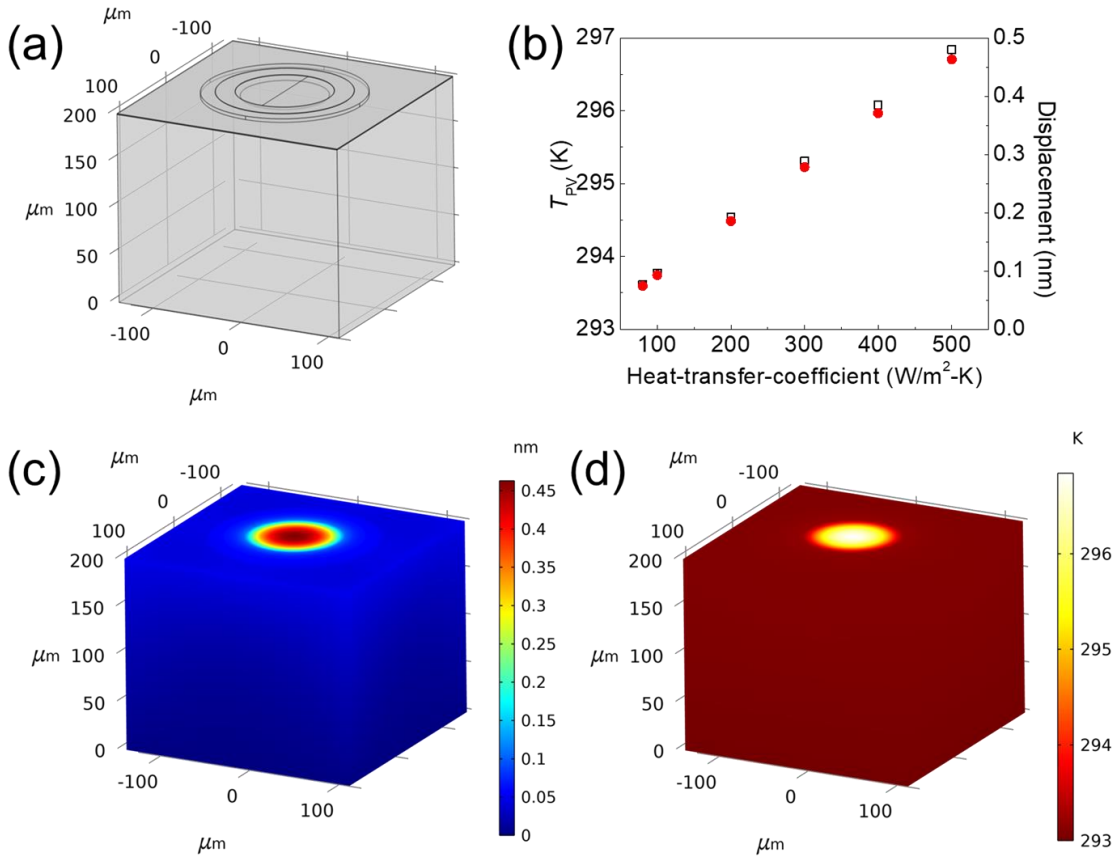

Figure A9. Analysis of the mechanical stability of the PV cell during the near-field-radiative-heat-transfer operation. (a) Finite-element-analysis (FEA) simulation structure. The solid line at the top is to extract the maximum PV surface temperature (T_{PV}) and the displacement during the simulation. (b) Plot of the extracted T_{PV} and the displacement as a function of the heat-transfer-coefficient (HTC). (c) Total displacement at the HTC = 500 W/m^2-K. (d) Temperature distribution of the PV cell at the HTC = 500 W/m^2-K.

Near-field-radiative-heat-transfer (NFRHT) operation is performed in vacuum (~10^{-6} Torr), where the radiative heat transfer (Q_{RHT}) to the photovoltaic (PV) cell is estimated as 2 mW at 1270 K with the nanogap of 100 nm. Due to uncertainty of additional heat emission from the silicon emitter including extended-long-beams (see Fig. 3.10(a)), we vary the total radiative heat from 2 to 5 mW. In this range, the heat-transfer-coefficient (HTC) is 80 ~ 450 W/m^2-K. Figure S9 (a) shows the FEA simulation structure. First, the displacement of the bottom boundary of the Si substrate is fixed for the simulation. The bottom boundary is set to the constant temperature of 300 K. The spacing of the air cavity, indicated by blue-color in Fig. A9(a), is filled by air with the pressure of 1 Torr (Bonding chamber pressure ~1 Torr). The Au plastic deformation is embodied by applying the 70 N force in z-axis to the Au layer [65]. The heat is applied on the top surface of the PV cell, then the rise of temperature, ΔT_{PV}, is calculated for the different HTC. As shown in Fig. A9(b), the ΔT_{PV} is only a few degrees, not affecting the structural deformation of the PV membrane on the air cavity.

A3. Numerical Method for Air-Bridge TPV Cell using a TCAD simulator

The TCAD method in this work uses the Monte Carlo (MC) technique, which is a stochastic method to solve complex device physics and mathematical problems [194]. The MC method simulates particle motions during a time, which is determined by random scattering events occurred by impurities, phonon, strained lattice, and two charged particles (coulomb scattering). In a given meshed simulation structure, the MC method computes the particle motions forced by electric-field and calculate the free-flight time until the motion is terminated by scattering mechanism. The boundary conditions are the charge conservation within the structure. Finally, the TCAD simulation solves nonequilibrium particle dynamics in a device modeling structure.

The air-bridge InGaAs TPV simulations were performed using Synopsys Sentaurus (Version S-2021.06), which simulates the charge-carrier distribution and transport by solving the charge continuity, Poisson, and drift-diffusion equations. In the simulation module (Sentaurus Device), the SRH model was included to account for non-radiative recombination. Also, the TMM solver calculates light propagation under blackbody spectrum. The Drude model reflects the FCA effect during the light propagation. We used the Sentaurus default material database (DB) for the $In_{0.53}Ga_{0.47}As$, InP, and metals. However, the physics parameters (such as radiative and nonradiative recombination coefficients, doping concentration, and charge recombination velocity). In the DB, the material air is not built-in and therefore its material properties were added manually. Table S3 shows the constants to create the DB for air. In Chapter 5, the calculation of the detailed balance limit was performed by setting the mobility as very high enough (10^{10} cm^2/Vs), which neglects the resistance of semiconductors. The metal contact resistance is also set to very low (10^{-20} Ω-cm); zero resistance is not realistic in the TCAD simulation because the numerical method cannot calculate Gauss's law and Poisson's equation, which is used to estimate a current-

density based on an electric-field and charge continuity in a volume. Finally, the radiative limit diode performance is enabled by excluding the function associated with non-radiative recombination. The TCAD calculates the microscopic random electron motions owing to thermal agitation (the temperature set to 293K for the simulation), resulting in the fluctuation of free charges and the electron density between the depletion edge at the p-n junction and the metal contact. Therefore, in Chapter 5, Figure 5.2 shows the thermal diffusion current which creates the difference between the TCAD models and the numerical fittings using the diode equation of Eq. 5.4.

Figure A11 (b) shows the mesh structure used for the TCAD simulation. The diode structure does not include a very low-doped semiconductor such as undoped materials, meaning that the voltage applied between the cathode and the anode is mostly dropped through the p-n and the hetero-material junctions. Therefore, the complicated mesh dimension is confined to the junctions. To avoid an unnecessary long simulation running time, the mesh in the semiconductor bulks was set relatively less dense.

Table A3. Parameters for the material properties of air at 293 K.

Permittivity constant, ε	1
Refractive index	1
Complex refractive index (n, k)	1, 0
Resistivity (ohm-cm)	10^{13}

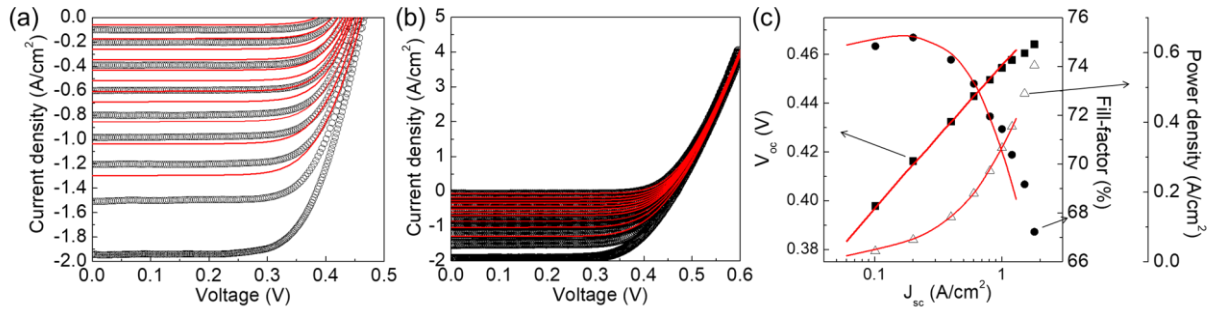

Figure A10. (a) *J-V* curves with the y-axis is zoomed in at the voltage range = 0.0–0.5 V. The black circles represent the experiment data from our previous work [1]. (b) *J-V* curves at voltages ranging from 0.0 to 0.6 V, with the y-axis is zoomed out from (a). The red-solid-lines are the TCAD modeling data. (c) V_{oc}, *FF*, and P_{out} parameters of as a function of J_{sc}.

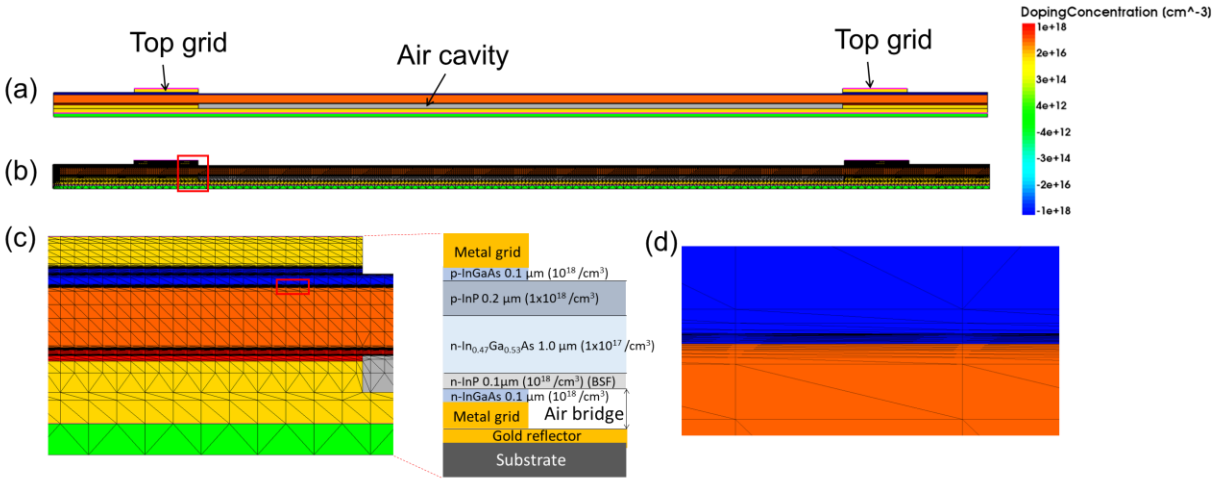

Figure A11. (a) TCAD model structure for the literature [1]. The color legend is the doping concentration. (b) Mesh structure. (c) The extended region marked by the red box in (b). The schematic indicates the photodiode structure with materials and doping types. (d) Mesh structure marked by the red box in (c). The p-n junction has the lowest mesh dimension where the electric field and the band structure bending are the most sensitive to the applied voltage.

A4. Drude Model for Free Carrier Absorption

A blackbody emission is a broad range spectrum, which is determined by Planck's law:

$$B\ (\lambda,T) = \frac{2hc^2}{\lambda^5}\frac{1}{e^{\left(\frac{hc}{\lambda k_b T}\right)}-1} \tag{A8}$$

where h = 6.62×10^{-34} J/Hz, c = 3×10^{8} m/sec, and k_b = 1.38×10^{-23} J/K. In semiconductors, free carriers (by doping or carrier injection) absorb photon energy, resulting in intra-band transition between energy states. The frequency response by the absorption is transient but becomes steady-state. Therefore, the Drude model – it means a model for electron scattering – can be used to find the free carrier absorption (FCA) coefficient. Using a damped second order system for the frequency response [195], the motion of a free particle in the electromagnetic (EM) wave is described by the second order differential equation [196]:

$$m^*\frac{d^2x}{dt^2}+\zeta\frac{dx}{dt} = qE_0e^{i\omega t} = \text{Force} \tag{A9}$$

where m^* is the particle mass, ζ is the damping ratio, and E_0 is the electric field. The two terms at the left-hand side mean the acceleration and frictional forces, respectively. In semiconductors, the scattering time is complicated and not a constant. To simplify this. The Drude model assumes the scattering time is a constant. By the boundary condition at ω = 0, the Eq. A9 turns into:

$$\zeta\frac{dx}{dt} = qE_0 \rightarrow \frac{dx}{dt} = \text{Velocity} = \frac{qE_0}{\zeta} = \mu E_0. \tag{A10}$$

Therefore, $\zeta = \frac{q}{\mu} = \frac{m^*}{\tau}$ where τ is the scattering time. Under an electric field, a charged particle has the displacement and the Eq. A9 is reinterpreted by

$$x_0 = \frac{qE_0}{\left(-m^*\omega^2+i\frac{m^*}{\tau}\omega\right)}, \tag{A11}$$

where $x = x_0 \cdot e^{i\omega t}$. A polar vector is defined by $\vec{P} = \varepsilon_0\chi_e\vec{E}$ where χ_e is electric susceptibility [197]. From Maxwell's equations (the Poisson's equation), the total charge density is defined by the

divergence of an electrical field. Therefore, at a given N_{free} (free carrier concentration), the induced polarization follows by:

$$P = q \cdot N_{free} \cdot x(t) = \frac{q^2 \cdot N_{free} \cdot E_0 e^{i\omega t}}{\left(-m^* \omega^2 + i\frac{m^*}{\tau}\omega\right)}. \tag{A12}$$

From the Poisson's equation, the electric field vector is $\vec{\nabla} \cdot \vec{E} = \frac{\rho}{\varepsilon_0} = \frac{\rho_f + \rho_b}{\varepsilon_0} = \frac{1}{\varepsilon_0}\left(\rho_f - \vec{\nabla} \cdot \vec{P}\right)$, where ρ_f and ρ_b mean the free and bound charges, respectively – imagine the Gauss's law by a closed surface –, and $\vec{P}$ is the polarization vector. Therefore, the displacement vector is

$$(\vec{D}) = \varepsilon \vec{E} = \varepsilon_0 \vec{E} + \vec{P}, \tag{A13}$$

which is determined by the free charges (ρ_f). From the Eq. A12 and Eq. A13, the complex dielectric constant can be expressed by:

$$\frac{\varepsilon}{\varepsilon_0} = 1 + \frac{q^2 \cdot N_{free}}{\varepsilon_0 m^* \omega\left(-\omega + \frac{i}{\tau}\right)} = 1 - \frac{q^2 \cdot N_{free}}{\varepsilon_0 m^* \omega\left(\omega^2 + \frac{1}{\tau^2}\right)}\left(\omega + \frac{i}{\tau}\right). \tag{A14}$$

Here the imaginary part is related to the FCA where the plasma frequency, $\omega_p = q\sqrt{\frac{N_{free}}{\varepsilon_0 m^*}}$ – from a quasi-neutral state with a frequency, a charged particle tends to become neutral. [198]. Therefore, the imaginary part in the Eq. A14 is reinterpreted by:

$$\text{Imag}\left(\frac{\varepsilon}{\varepsilon_0}\right) = \frac{\omega_p^2}{\omega\left(\omega^2 + \frac{1}{\tau^2}\right)}\frac{1}{\tau}, \tag{A15}$$

where ω is the optical wavelength and the τ is the scattering time. The absorption coefficient is expressed using the Beer-Lambert law:

$$\alpha = \frac{4\pi k}{\lambda} = \frac{2\pi}{n\lambda}\varepsilon_0 \frac{\omega_p^2}{\omega\left(\omega^2 + \frac{1}{\tau^2}\right)}\frac{1}{\tau} = \frac{2\pi}{n\left(2\pi\frac{c}{\omega}\right)}\varepsilon_0 \frac{\omega_p^2}{\omega\left(\omega^2 + \frac{1}{\tau^2}\right)}\frac{1}{\tau} = \frac{1}{nc}\varepsilon_0 \frac{\omega_p^2}{\left(\omega^2 + \frac{1}{\tau^2}\right)}\frac{1}{\tau} = \frac{1}{nc}\varepsilon_0 \frac{q^2\frac{N_{free}}{\varepsilon_0 m^*}}{\left(\omega^2 + \frac{1}{\tau^2}\right)}\frac{q}{\mu m^*}$$

$$= \frac{q^3 N_{free}}{nc\mu\left(m^*\right)^2 \times \left(\omega^2 + \frac{1}{\tau^2}\right)} \tag{A16}$$

where $2nk = \mathrm{Imag}(\varepsilon)$. The n and k are the refractive indexes for real and imaginary parts, respectively. With the assumption that the optical frequencies are much smaller than the scattering frequency (10^{12} Hz), the FCA coefficient is expressed by:

$$\alpha = \mathrm{C}\frac{N_{free}\lambda^2}{\mu}. \tag{A17}$$

Therefore, the FCA is linearly determined by the number of free charges and the scattering frequency. In Chapter 5, the ideal limit of the energy conversion efficiency of a TPV cell assumes no FCA effect and an infinite semiconductor mobility. This is consistent with the Eq. A17 because an infinite mobility results in negligible FCA effect. During the derivation, we assumed the scattering time as a constant. However, the scattering time varies as a function of carrier concentration and temperature. Therefore, the square of the lambda in the equation is empirically determined by λ^{γ}, resulting in the Eq. (5.13). The origin of the derivation is insighted from the textbook [196]. Also, in the Eq. A16, we assumed that the scattering frequency (ω_s) is much shorter than the optical frequency (ω_{op}). However, in long infrared wavelengths (> 5 μm), the optical frequency becomes relatively smaller ($\omega_{op} < 5\times10^{13}$ Hz), meaning that the scattering frequency cannot be negligible anymore.

A5. Energy Band Structures for an Air-Bridge InGaAs Photodiode

Single-junction InGaAs cell

Figure A12 shows the energy band structures for the air-bridge InGaAs photodiode structure in Fig. 5.1. At the equilibrium state, *'A'* indicates the intrinsic high electric field junction between the n-type semiconductors of the InGaAs and InP, which accelerates electrons from the InGaAs to the InP. The thickness of the InP layer is only less than 100 nm (Note: The momentum of free electrons is not constant or everlasting owing to scattering mechanisms. Any charged particle loses an energy during the motion. Due to the energy barrier indicated by '*B*', a relatively thick heavy-doped n-InP will cause the rise of the R_s.). The '*C*' forms the back surface field (BSF) as an energy blocking layer for holes, suppressing not only the minority carrier (hole) flow to the surface closer to the anode but also the recombination at the hetero interface. In Fig. A12 (c), the open-circuit voltage (V_{OC}) is dropped through the p-n junction, resulting in the zero net current with the flat quasi-fermi levels.

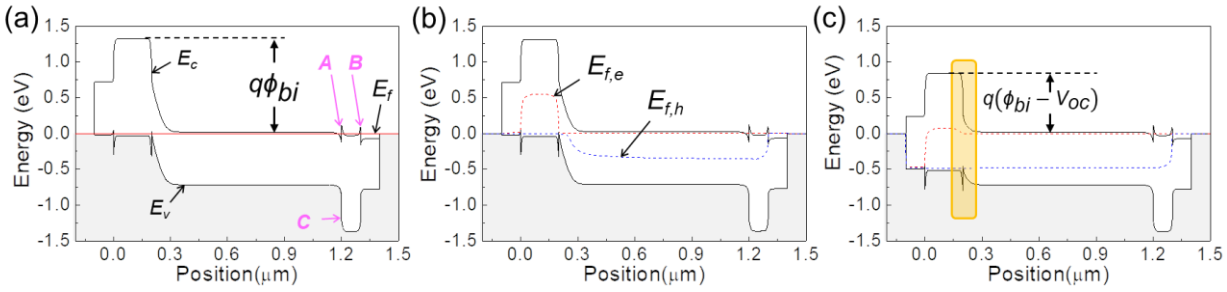

Figure A12. Energy band structures for an air-bridge InGaAs TPV device. (a) Equilibrium under dark, (b) Quasi fermi level ($E_{f,e}$ and $E_{f,h}$) splits under heat emission with zero bias, and (c) $E_{f,e}$ and $E_{f,h}$ splits under the same heat emission with V_{oc} bias.

A6. Simulation results of the New InGaAs Photodiode

In Chapter 3, the new InGaAs/InP photodiode is introduced. Before conducting experimental demonstrations, we used the TCAD to validate the device performance. Figure A13(a) compares the *J-V* simulation results between the previous [1] and the new structures. The TCAD used the same model in Chapter 5. It shows no significant difference as the two structures have the same InGaAs absorber, deciding J_{ph}, and the same p-type InP window, mainly contributing R_s. Figure A13(b) shows the comparison of the absorption spectrum through the InP/InGaAs/InP sandwiched layers, as illustrated by the inset. The absorption in the energy range between 0.74 eV and 3 eV shows 65.7 % and 65.9 % for the old and the new, respectively, meaning that the two structures have similar spectral responses and the only 0.2% difference comes from the bottom 2 μm InP layer. Figure A13(c) is the calculated lifetime as a function of carrier concentrations. The coefficients for radiative and auger recombination were borrowed from the literature, which assumed that the SRH lifetime is 47 μs [175]. Therefore, the radiative recombination coefficient and the carrier concentration are the main factors to decide the charge lifetime and the diffusion length. As the InGaAs absorber thickness approaches or becomes larger than the diffusion length, the J_{sc} is reduced or the *IQE* is reduced: 96.0, 92.7, and 89.9% for 1, 1.5, and 2 μm InGaAs, respectively.

Figure A14 (a) is the schematic of the new InGaAs photodiode structure. In Chapter 3, Figure 3.3 (b) shows the resistance of InP buffer layers via doping concentrations. Figure A14 (b) shows the comparison of *J-V* under illumination with different doping concentrations in the n-InP buffer layer. Under a relatively low illumination power, the ohmic loss is significant for *FF* and the doping level does not affect to the *J-V* parameters in Table A5. Figure 3.3 (c) is the extended *J-V* graphs, showing that the R_s is increased by decreasing the doping level. Carrier concentrations

higher than 10^{15} /cm^3 do not affect the R_s because the resistance of the n-InP buffer layer is much smaller than the total R_s. However, carrier concentrations lower than 10^{15} /cm^3 start to increase the R_s, meaning that ohmic loss by the R_s can cause a drop of PCE under a relatively high illumination power. We note that a minimum doping concentration in n-type InGaAs by the solid-source MBE system is around 1×10^{16} /cm^3 to 5×10^{16} /cm^3. The TCAD material database used the same set-up for the experiment model introduced in Chapter 5. The R_s of the model shows a relatively large due to practical factors such as epilayer quality and metal resistance. This can be reduced to be less than 7 mΩ-cm^2, as shown in Fig. 3.6 (a) in Chapter 3.

Figure A15 indicates the TCAD *J-V* graphs between two different metal contact resistances (R_c). The 2×10^{-5} Ω-cm^2 is from the experiment model in Chapter 5. The R_c is assumed to be negligible with $R_c = 2\times10^{-10}$ Ω-cm^2. The V_{oc} and J_{sc} do not show a significant difference between them. The *FF* and R_s with the lower R_c are remarkably enhanced. Thus, decreasing R_c is critical for suppressing the PCE drop caused by ohmic loss. The *FF* and R_s are improved by reducing the W_{air} (air-cavity width) to 50 μm, which design can optimize the TPV PCE as described in Chapter 5.

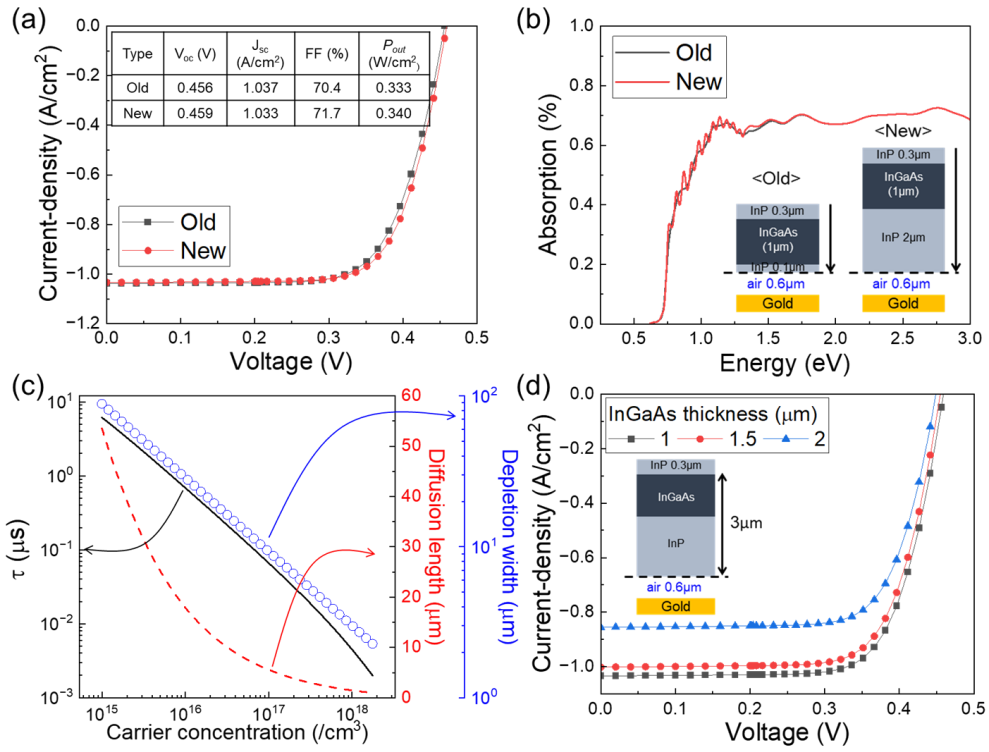

Figure A13. (a) TCAD simulation results for the *J-V* comparison between the old and the new air-bridge InGaAs TPV cells. The blackbody spectrum is 1500K with an arbitrary power intensity. (b) Simulated absorption spectrum comparison between the two structures described by the inset. (c) Calculated charge lifetimes, diffusion lengths, and depletion widths at the p-n junction via the carrier concentration. (d) TCAD simulation results for the *J-V* comparison by changing the InGaAs absorber thicknesses.

Table A4. Parameters for the TCAD *J-V* graphs in Fig. A13(d).

InGaAs thickness (μm)	J_{sc} (A/cm^2)	V_{oc} (V)	*FF* (%)	*IQE* (%)
1	1.033	0.459	71.75	96.0
1.5	1.001	0.455	71.79	92.7
2	0.855	0.449	72.56	89.9

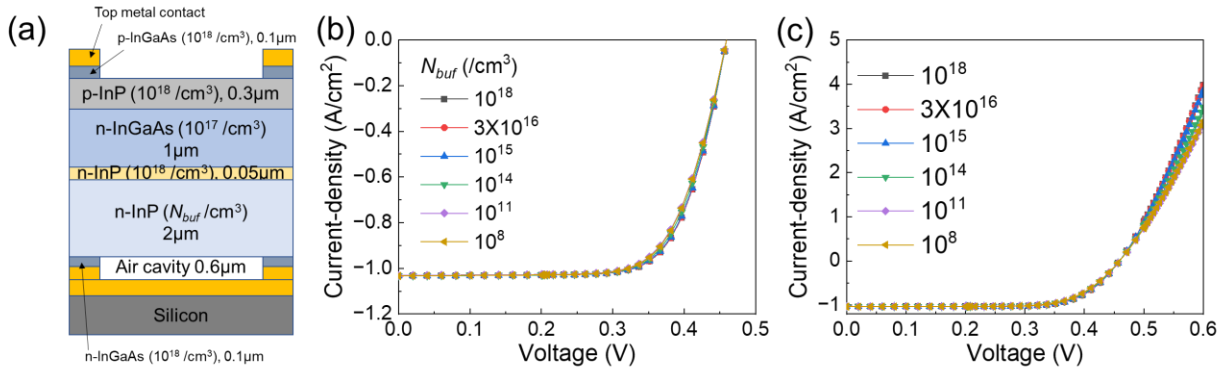

Figure A14. (a) Air-bridge InGaAs TPV structure with a 2-μm-thick n-InP layer. The N_{buf} means the carrier concentration of the layer. (b) and (c) TCAD *J-V* simulation for the under illumination (1500K blackbody source with an arbitrary power) with different N_{buf} levels.

Table A5. Parameters for the TCAD *J-V* graphs in Fig. A14.

n-InP 2 μm doping concentration (/cm^3)	J_{sc} (A/cm^2)	V_{oc} (V)	*FF* (%)	R_s (mΩ-cm^2)
10^{18}	1.03	0.46	71.78	28.52
3×10^{16}	1.03	0.46	71.75	28.58
10^{15}	1.03	0.46	71.62	29.55
10^{14}	1.03	0.46	71.10	33.50
10^{11}	1.03	0.46	70.48	37.92
10^{8}	1.03	0.46	70.55	37.41

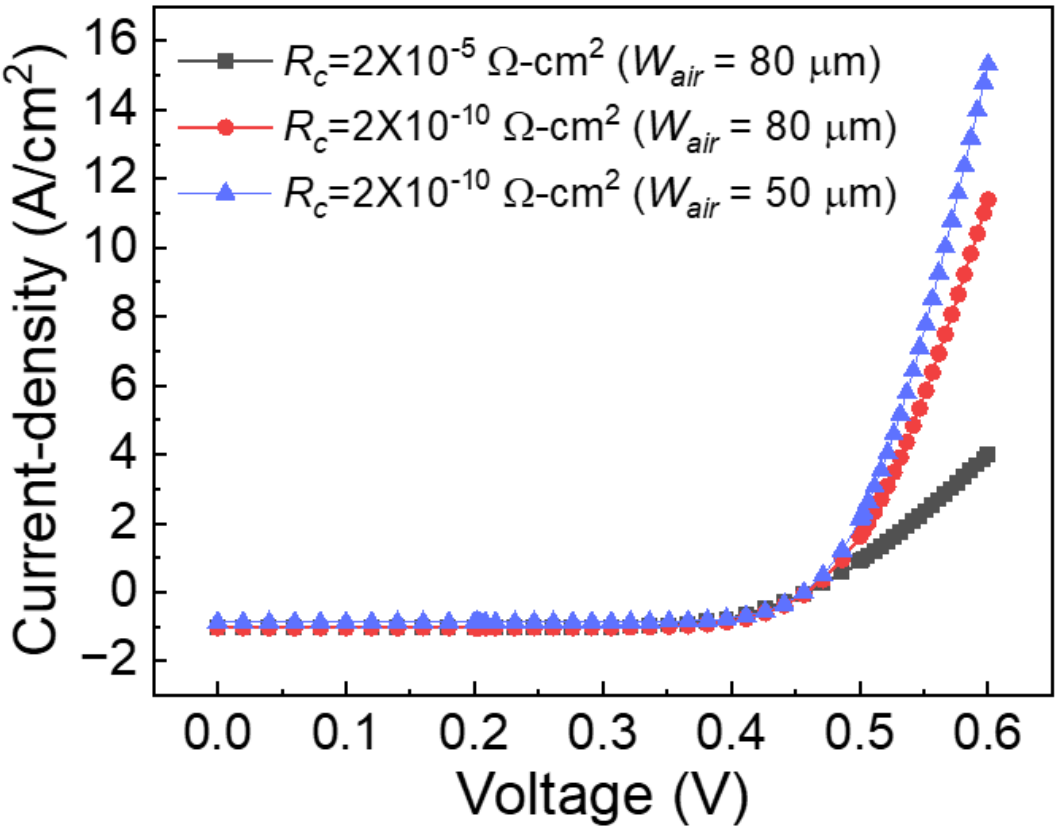

Figure A15. TCAD *J-V* simulation for the InGaAs AB-TPV cell the under illumination (1500K blackbody source with an arbitrary power). The *J-V* parameters are in Table A6.

Table A6. Parameters for the TCAD *J-V* graphs in Fig. A15. W_{air} is the air-cavity spacing between Au grids.

W_{air} (μm)	R_c (Ω-cm^2)	J_{sc} (A/cm^2)	V_{oc} (V)	*FF* (%)	R_s (mΩ-cm^2)
80	2×10^{-5}	1.03	0.46	71.75	28.6
80	2×10^{-10}	1.03	0.46	75.06	8.4
50	2×10^{-10}	0.88	0.46	77.43	6.2

A7. Buckled TPV Membranes Dataset with FEA Simulation and Reflectance

Figure A16 is the measured buckling of TPV samples with t_{TPV} = 1.4 μm and 3.4 μm. The upward or downward buckling can be controlled as a function of thin-film thicknesses, air-cavity spacings, and internal pressures in the cavity.

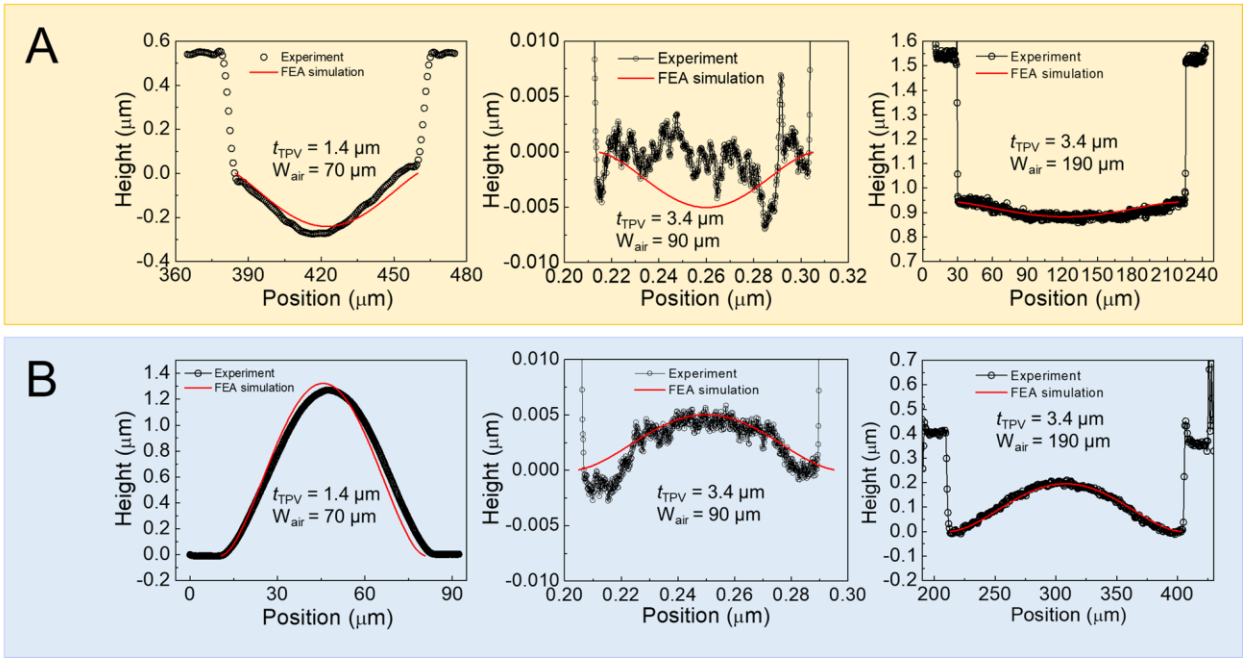

Figure A16. Buckled TPV Membranes. The buckled TPV membranes, showing the downward buckling (Panel A) and the upward buckling (Panel B) due to the reduced and the increased internal pressures inside the air cavities, respectively. The measurement tool has the resolution of 10nm.

Figure A17 shows the FTIR measurements for buckled TPV membranes, where the TPV membrane is 1.4-μm-thick InGaAs TPV epilayers. The absorption spectra have multiple cavity modes due to non-uniform cavity thicknesses, resulting in the broadening of the cavity oscillations at the out-of-band wavelengths. Therefore, a non-buckled TPV membrane is important to achieve uniform cavity oscillations.

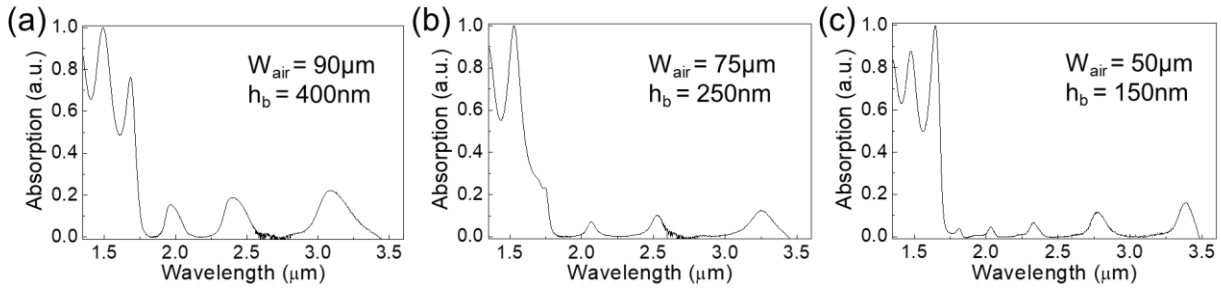

Figure A17. Fourier-transform infrared measurements with different buckled TPV membranes.

Bibliography

[1] D. Fan, T. Burger, S. McSherry, B. Lee, A. Lenert, and S. Forrest, Nature **586**, 237 (2020).

[2] T. Burger, D. Fan, K. Lee, S. Forrest, and A. Lenert, Acs Photonics **5**, 2748 (2018).

[3] G. Charache, D. DePoy, P. Baldasaro, B. Campbell, J. Benner, T. Coutts, and D. Ginley, Second Nrel Conference on Thermophotovoltaic Generation of Electricity, 339 (1996).

[4] S. Molesky and Z. Jacob, Physical Review B **91**, ARTN 205435 (2015).

[5] A. Lenert, D. Bierman, Y. Nam, W. Chan, I. Celanovic, M. Soljacic, and E. Wang, Nature Nanotechnology **9**, 126 (2014).

[6] Z. Zhou, Q. Chen, and P. Bermel, Energy Conversion and Management **97**, 63 (2015).

[7] L. Fraas, J. Avery, H. Huang, and R. Martinelli, Semiconductor Science and Technology **18**, S165, PII S0268-1242(03)59176-3 (2003).

[8] R. Bhatt, I. Kravchenko, and M. Gupta, Solar Energy **197**, 538 (2020).

[9] Z. Holman, S. De Wolf, and C. Ballif, Light-Science & Applications **2**, ARTN e106 (2013).

[10] U. Rau, U. Paetzold, and T. Kirchartz, Physical Review B **90**, ARTN 035211 (2014).

[11] W. R. Cline, *The economics of global warming* (Institute for International Economics, Washington, 1992).

[12] W. Nordhaus, Climatic Change **148**, 623 (2018).

[13] M. Mimikou and E. Baltas, Hydrological Sciences Journal-Journal Des Sciences Hydrologiques **42**, 661 (1997).

[14] J. Bae *et al.*, Energy & Environmental Science **15**, 123 (2022).

[15] A. Carroll and C. Somerville, Annual Review of Plant Biology **60**, 165 (2009).

[16] J. Keasling, H. Martin, T. Lee, A. Mukhopadhyay, S. Singer, and E. Sundstrom, Nature Reviews Microbiology **19**, 701 (2021).

[17] R. Luque, L. Herrero-Davila, J. Campelo, J. Clark, J. Hidalgo, D. Luna, J. Marinas, and A. Romero, Energy & Environmental Science **1**, 542 (2008).

[18] R. Chedid, F. Mrad, and M. Basma, IEEE Transactions on Energy Conversion **14**, 1597 (1999).

[19] R. Billinton and Y. Gao, IEEE Transactions on Energy Conversion **23**, 163 (2008).

[20] M. Cheng and Y. Zhu, Energy Conversion and Management **88**, 332 (2014).

[21] V. Yaramasu, B. Wu, P. Sen, S. Kouro, and M. Narimani, Proceedings of the IEEE **103**, 740 (2015).

[22] M. Bragard, N. Soltau, S. Thomas, and R. De Doncker, IEEE Transactions on Power Electronics **25**, 3049 (2010).

[23] D. Vatansever, R. Hadimani, T. Shah, and E. Siores, Smart Materials and Structures **20**, ARTN 055019 (2011).

[24] H. Zabed, J. Sahu, A. Suely, A. Boyce, and G. Faruq, Renewable & Sustainable Energy Reviews **71**, 475 (2017).

[25] D. Carson and C. Wronski, Applied Physics Letters **28**, 671 (1976).

[26] R. C. Knechtli, R. Y. Loo, and G. S. Kamath, IEEE Transactions on electron devices **31**, 577 (1984).

[27] N. Ekins-Daukes, K. Barnham, J. Connolly, J. Roberts, J. Clark, G. Hill, and M. Mazzer, Applied Physics Letters **75**, 4195 (1999).

[28] A. Shah, H. Schade, M. Vanecek, J. Meier, E. Vallat-Sauvain, N. Wyrsch, U. Kroll, C. Droz, and J. Bailat, Progress in Photovoltaics **12**, 113 (2004).

[29] S. Forrest, Mrs Bulletin **30**, 28 (2005).

[30] F. Yang, M. Shtein, and S. Forrest, Nature Materials **4**, 37 (2005).

[31] J. You *et al.*, Nature Communications **4**, ARTN 1446 (2013).

[32] K. Lee, J. Zimmerman, T. Hughes, and S. Forrest, Advanced Functional Materials **24**, 4284 (2014).

[33] A. Lamoureux, K. Lee, M. Shlian, S. Forrest, and M. Shtein, Nature Communications **6**, ARTN 8092 (2015).

[34] M. Hermle, F. Feldmann, M. Bivour, J. Goldschmidt, and S. Glunz, Applied Physics Reviews **7**, 021305 (2020).

[35] M. Green, E. Dunlop, J. Hohl-Ebinger, M. Yoshita, N. Kopidakis, and X. Hao, Progress in Photovoltaics **29**, 3 (2021).

[36] L. Kruitwagen, K. Story, J. Friedrich, L. Byers, S. Skillman, and C. Hepburn, Nature **598**, 604 (2021).

[37] P. Majewski, W. Al-shammari, M. Dudley, J. Jit, S. Lee, K. Myoung-Kug, and K. Sung-Jim, Energy Policy **149**, ARTN 112062 (2021).

[38] S. Mekhilef, R. Saidur, and A. Safari, Renewable & Sustainable Energy Reviews **15**, 1777 (2011).

[39] N. Kannan and D. Vakeesan, Renewable & Sustainable Energy Reviews **62**, 1092 (2016).

[40] S. Kusch-Brandt, Resources-Basel **8**, 139 (2019).

[41] P. Peumans, A. Yakimov, and S. Forrest, Journal of Applied Physics **93**, 3693 (2003).

[42] B. Rand, P. Peumans, and S. Forrest, Journal of Applied Physics **96**, 7519 (2004).

[43] Q. Burlingame, X. Huang, X. Liu, C. Jeong, C. Coburn, and S. Forrest, Nature **573**, 394 (2019).

[44] Z. Lian *et al.*, Journal of the American Chemical Society **141**, 2446 (2019).

[45] K. Wang, H. Hu, S. Lu, L. Guo, T. Zhang, Y. Han, A. Zhou, and T. He, Optical Materials Express **6**, 3977 (2016).

[46] E. Moon, D. Blaauw, and J. Phillips, IEEE Transactions on Electron Devices **64**, 2432 (2017).

[47] A. Motmaen, A. Rostami, and S. Matloub, Scientific Reports **10**, 9325 (2020).

[48] D. L. Chubb, (Elsevier, Amsterdam, Netherlands ; Boston ; Oxford, UK, 2007), p. 1 online resource (531 p.).

[49] T. Coutts, Renewable & Sustainable Energy Reviews **3**, 77 (1999).

[50] A. Fiorino, L. Zhu, D. Thompson, R. Mittapally, P. Reddy, and E. Meyhofer, Nature Nanotechnology **13**, 806 (2018).

[51] T. Burger, C. Sempere, B. Roy-Layinde, and A. Lenert, Joule **4**, 1660 (2020).

[52] M. Opher and R. Opher, Physical Review Letters **79**, 2628 (1997).

[53] L. Woolf, Solar Cells **19**, 19 (1986).

[54] A. LaPotin *et al.*, Nature **604**, 287 (2022).

[55] R. Mahorter, B. Wernsman, R. Thomas, and R. Siergiej, Semiconductor Science and Technology **18**, S232, PII S0268-1242(03)59385-3 (2003).

[56] T. P. Ginley and S. Law, Journal of Vacuum Science & Technology B, Nanotechnology and Microelectronics: Materials, Processing, Measurement, and Phenomena **34**, 02L105 (2016).

[57] M. S. Leite, R. L. Woo, J. N. Munday, W. D. Hong, S. Mesropian, D. C. Law, and H. A. Atwater, Applied Physics Letters **102**, 033901 (2013).

[58] K. Evans, R. Kaspi, J. Ehret, M. Skowronski, and C. Jones, Journal of Vacuum Science & Technology B: Microelectronics and Nanometer Structures Processing, Measurement, and Phenomena **13**, 1820 (1995).

[59] W. Strupinski, K. Kosiel, A. Jasik, R. Jakiela, A. Jelenski, E. Kollberg, L. Dillner, and M. Nawaz, in *13th International Conference on Microwaves, Radar and Wireless Communications. MIKON-2000. Conference Proceedings (IEEE Cat. No. 00EX428)* (IEEE, 2000), pp. 129.

[60] Y. Wang *et al.*, Nanoscale Research Letters **12**, 1 (2017).

[61] L. Chia and B. Feng, Journal of Power Sources **165**, 455 (2007).

[62] A. H. Epstein *et al.*, in *Proceedings of International Solid State Sensors and Actuators Conference (Transducers' 97)* (IEEE, 1997), pp. 753.

[63] E. Fontana, L. Battiston, R. Oliveira, C. Capeletto, and L. Luz, Energy **239**, 122184 (2022).

[64] W. Chan, P. Bermel, R. Pilawa-Podgurski, C. Marton, K. Jensen, J. Senkevich, J. Joannopoulos, M. Soljacic, and I. Celanovic, Proceedings of the National Academy of Sciences of the United States of America **110**, 5309 (2013).

[65] J. Lim, D. Fan, B. Lee, and S. Forrest, Physical Review Applied **16**, ARTN 064010 (2021).

[66] R. Mittapally, B. Lee, L. Zhu, A. Reihani, J. Lim, D. Fan, S. Forrest, P. Reddy, and E. Meyhofer, Nature Communications **12**, 4364, 4364 (2021).

[67] M. Laroche, R. Carminati, and J. Greffet, Journal of Applied Physics **100**, ARTN 063704 (2006).

[68] K. Park, S. Basu, W. King, and Z. Zhang, Journal of Quantitative Spectroscopy & Radiative Transfer **109**, 305 (2008).

[69] A. Narayanaswamy and G. Chen, Applied Physics Letters **82**, 3544 (2003).

[70] Y. Lou, X. Zhang, A. Huang, and Y. Wang, Solar Energy Materials and Solar Cells **172**, 124 (2017).

[71] N. Szabo, B. Sagol, U. Seidel, K. Schwarzburg, and T. Hannappel, Physica Status Solidi-Rapid Research Letters **2**, 254 (2008).

[72] M. Steiner, M. Wanlass, J. Carapella, A. Duda, J. Ward, T. Moriarty, and K. Emery, Progress in Photovoltaics **17**, 587 (2009).

[73] J. Hutchinson, M. Thouless, and E. Liniger, Acta Metallurgica Et Materialia **40**, 295 (1992).

[74] H. Ren *et al.*, Acs Nano **13**, 3106 (2019).

[75] Y. Shi, A. Bork, S. Schweiger, and J. Rupp, Nature Materials **14**, 721 (2015).

[76] J. Faou, G. Parry, S. Grachev, and E. Barthel, Physical Review Letters **108**, 116102, 116102 (2012).

[77] M. Thouless, Journal of the American Ceramic Society **76**, 2936 (1993).

[78] Y. Ni, S. Yu, H. Jiang, and L. He, Nature Communications **8**, 14138, 14138 (2017).

[79] A. Vanderheijden, Journal of the Mechanics and Physics of Solids **27**, 441 (1979).

[80] M. Schumann, T. Buckmann, N. Gruhler, M. Wegener, and W. Pernice, Light-Science & Applications **3**, e175 (2014).

[81] D. Yin, J. Feng, R. Ma, Y. Liu, Y. Zhang, X. Zhang, Y. Bi, Q. Chen, and H. Sun, Nature Communications **7**, 11573 (2016).

[82] C. Zhang, H. Deng, Y. Xie, J. Su, and J. Lin, Small **15**, 1904224, 1904224 (2019).

[83] P. Wang, F. Casadei, S. Shan, J. Weaver, and K. Bertoldi, Physical Review Letters **113**, 014301, 014301 (2014).

[84] J. Paulose, A. Meeussen, and V. Vitelli, Proceedings of the National Academy of Sciences of the United States of America **112**, 7639 (2015).

[85] E. Filipov, T. Tachi, and G. Paulino, Proceedings of the National Academy of Sciences of the United States of America **112**, 12321 (2015).

[86] V. Shalaev, Nature Photonics **1**, 41 (2007).

[87] T. Frenzel, M. Kadic, and M. Wegener, Science **358**, 1072 (2017).

[88] X. Ni, Z. Wong, M. Mrejen, Y. Wang, and X. Zhang, Science **349**, 1310 (2015).

[89] Z. Omair *et al.*, Proceedings of the National Academy of Sciences of the United States of America **116**, 15356 (2019).

[90] Y. Ling *et al.*, Acs Nano **12**, 12456 (2018).

[91] H. Fu *et al.*, Nature Materials **17**, 268 (2018).

[92] K. Bai *et al.*, Science Advances **6**, eabb7417, eabb7417 (2020).

[93] Y. Sun, W. Choi, H. Jiang, Y. Huang, and J. Rogers, Nature Nanotechnology **1**, 201 (2006).

[94] H. Zhao *et al.*, Proceedings of the National Academy of Sciences of the United States of America **116**, 13239 (2019).

[95] S. Xu *et al.*, Science **347**, 154 (2015).

[96] R. Jackman, S. Brittain, A. Adams, M. Prentiss, and G. Whitesides, Science **280**, 2089 (1998).

[97] D. Fan, B. Lee, C. Coburn, and S. Forrest, Proceedings of the National Academy of Sciences of the United States of America **116**, 3968 (2019).

[98] Q. Zhang, Y. Tang, M. Hajfathalian, C. Chen, K. Turner, D. Dikin, G. Lin, and J. Yin, Acs Applied Materials & Interfaces **9**, 44938 (2017).

[99] C. Yu, Z. Wang, H. Yu, and H. Jiang, Applied Physics Letters **95**, 141912, 141912 (2009).

[100] H. Jiang, D. Khang, J. Song, Y. Sun, Y. Huang, and J. Rogers, Proceedings of the National Academy of Sciences of the United States of America **104**, 15607 (2007).

[101] Y. Sun, V. Kumar, I. Adesida, and J. Rogers, Advanced Materials **18**, 2857 (2006).

[102] A. Shevyrin *et al.*, Applied Physics Letters **101**, 241916, 241916 (2012).

[103] H. Jiang, Y. Sun, J. Rogers, and Y. Huang, Applied Physics Letters **90**, 133119, 133119 (2007).

[104] T. Jiang, R. Huang, and Y. Zhu, Advanced Functional Materials **24**, 396 (2014).

[105] H. Hattab *et al.*, Nano Letters **12**, 678 (2012).

[106] W. Lee, J. Kang, K. Chen, C. Engel, W. Jung, D. Rhee, M. Hersam, and T. Odom, Nano Letters **16**, 7121 (2016).

[107] A. Azcatl *et al.*, Nano Letters **16**, 5437 (2016).

[108] S. Kim, D. Kim, J. Lim, S. Cho, S. Kim, and H. Jung, Acs Applied Materials & Interfaces **8**, 13512 (2016).

[109] H. Ren, L. Zhang, and G. Xiang, Applied Physics Letters **116**, 012401 (2020).

[110] Y. Zhang, F. Wang, Y. Ma, and X. Feng, International Journal of Solids and Structures **161**, 55 (2019).

[111] O. A. Bauchau and J. I. Craig, *Structural analysis : with applications to aerospace structures* (Springer, Dordrecht ; New York, 2009), Solid mechanics and its applications ,, 163.

[112] A. Sears and R. Batra, Physical Review B **73**, 085410, 085410 (2006).

[113] D. Fan, K. Lee, and S. Forres, Acs Photonics **3**, 670 (2016).

[114] G. Wang and X. Feng, Applied Physics Letters **94**, 141913, 141913 (2009).

[115] H. Yap, R. Lakes, and R. Carpick, Nano Letters **7**, 1149 (2007).

[116] G. Patriarche and E. Le Bourhis, Journal of Materials Science Letters **20**, 43 (2001).

[117] S. Mannsfeld, B. Tee, R. Stoltenberg, C. Chen, S. Barman, B. Muir, A. Sokolov, C. Reese, and Z. Bao, Nature Materials **9**, 859 (2010).

[118] Y. Zang, F. Zhang, D. Huang, X. Gao, C. Di, and D. Zhu, Nature Communications **6**, 6269, 6269 (2015).

[119] F. Martins, C. Felgueiras, M. Smitkova, and N. Caetano, Energies **12**, 964 (2019).

[120] S. Basu, Y. Chen, and Z. Zhang, International Journal of Energy Research **31**, 689 (2007).

[121] S. Cha, B. Koo, S. Seo, and D. Lee, Journal of Materials Chemistry **20**, 659 (2010).

[122] T. Kim *et al.*, Nature Communications **6**, ARTN 8547 (2015).

[123] A. H. Epstein, Turbo Expo: Power for Land, Sea, and Air **36878**, 669 (2003).

[124] M. Ishikawa, M. Terauchi, T. Komori, and J. Yasuraoka, Mitsubishi Heavy Industries, Ltd. Technical Review **45**, 15 (2008).

[125] D. Hahn, O. Jaschinski, H. Wehmann, A. Schlachetzki, and M. Ortenberg, Journal of Electronic Materials **24**, 1357 (1995).

[126] J. Katahara and H. Hillhouse, Journal of Applied Physics **116**, ARTN 173504 (2014).

[127] S. Perkowitz, Journal of Physics and Chemistry of Solids **32**, 2267 (1971).

[128] I. T. Sorokina and K. L. Vodopyanov, (Springer Berlin Heidelberg : Imprint: Springer, Berlin, Heidelberg, 2003), pp. 1 online resource (XVI.

[129] W. Walukiewicz, J. Lagowski, L. Jastrzebski, P. Rava, M. Lichtensteiger, C. Gatos, and H. Gatos, Journal of Applied Physics **51**, 2659 (1980).

[130] M. Sotoodeh, A. Khalid, and A. Rezazadeh, Journal of Applied Physics **87**, 2890 (2000).

[131] J. Lin, S. Yu, and S. Mohney, Journal of Applied Physics **114**, ARTN 044504 (2013).

[132] D. Ivey and P. Jian, Journal of Materials Science-Materials in Electronics **6**, 219 (1995).

[133] P. Postigo, M. Dotor, P. Huertas, D. Golmayo, and F. Briones, Journal of Applied Physics **77**, 402 (1995).

[134] H. Wang *et al.*, Materials Science in Semiconductor Processing **112**, ARTN 105012 (2020).

[135] S. Yoon and H. Zheng, Materials Chemistry and Physics **56**, 249 (1998).

[136] D. Vorselen, E. Kooreman, G. Wuite, and W. Roos, Scientific Reports **6**, ARTN 36972 (2016).

[137] W. Pan, P. Wang, X. Wu, K. Wang, J. Cui, L. Yue, L. Zhang, Q. Gong, and S. Wang, Journal of Alloys and Compounds **656**, 777 (2016).

[138] C. Cheng, W. Weng, H. Lin, J. Chiu, H. Jhao, Y. Liao, C. Yu, and H. Chen, Rsc Advances **8**, 26341 (2018).

[139] D. Chan and J. Phang, IEEE Transactions on Electron Devices **34**, 286 (1987).

[140] E. Moon, D. Blaauw, and J. Phillips, IEEE Transactions on Electron Devices **64**, 4554 (2017).

[141] M. Hudait, Y. Lin, S. Goss, P. Smith, S. Bradley, L. Brillson, S. Johnston, R. Ahrenkiel, and S. Ringel, Applied Physics Letters **87**, ARTN 032106 (2005).

[142] P. Smith, S. Goss, M. Gao, M. Hudait, Y. Lin, S. Ringel, and L. Brillson, Journal of Vacuum Science & Technology B **23**, 1832 (2005).

[143] M. Kohler *et al.*, Nature Energy **6**, 529 (2021).

[144] A. Scheuermann, J. Lawrence, K. Kemp, T. Ito, A. Walsh, C. Chidsey, P. Hurley, and P. McIntyre, Nature Materials **15**, 99 (2016).

[145] A. Belghachi and S. Khelifi, Solar Energy Materials and Solar Cells **90**, 1 (2006).

[146] A. Yamaguchi, H. Asamizu, T. Okada, Y. Iguchi, T. Saitoh, Y. Koide, and M. Murakami, Journal of Vacuum Science & Technology B **18**, 1957 (2000).

[147] V. Keramidas, H. Temkin, R. Mccoy, and W. Bonner, Journal of the Electrochemical Society **126**, C332 (1979).

[148] R. Hamm, M. Panish, R. Nottenburg, Y. Chen, and D. Humphrey, Applied Physics Letters **54**, 2586 (1989).

[149] Y. Miyazaki, Y. Hanamaki, H. Tada, K. Takagi, M. Takemi, T. Aoyagi, Y. Mihashi, and Y. Mitsui, Journal of Applied Physics **93**, 3823 (2003).

[150] X. Sun, T. Silverman, Z. Zhou, M. Khan, P. Bermel, and M. Alam, IEEE Journal of Photovoltaics **7**, 566 (2017).

[151] T. Coutts, Solar Energy Materials and Solar Cells **66**, 443 (2001).

[152] J. Song, J. Han, M. Choi, and B. Lee, Solar Energy Materials and Solar Cells **238**, ARTN 111556 (2022).

[153] S. Molesky, C. Dewalt, and Z. Jacob, Optics Express **21**, A96 (2013).

[154] C. Shemelya, D. DeMeo, N. Latham, X. Wu, C. Bingham, W. Padilla, and T. Vandervelde, Applied Physics Letters **104**, ARTN 201113 (2014).

[155] J. Song, M. Choi, M. Lim, J. Lee, and B. Lee, Solar Energy Materials and Solar Cells **236**, ARTN 111522 (2022).

[156] H. Yang, R. Liu, L. Wang, Y. Lu, T. Li, G. Li, Y. Zhang, and B. Zhang, Chinese Physics B **22**, ARTN 108402 (2013).

[157] K. Schulte, R. France, D. Friedman, A. LaPotin, A. Henry, and M. Steiner, Journal of Applied Physics **128**, ARTN 143103 (2020).

[158] F. Meillaud, A. Shah, C. Droz, E. Vallat-Sauvain, and C. Miazza, Solar Energy Materials and Solar Cells **90**, 2952 (2006).

[159] Z. Yu, M. Leilaeioun, and Z. Holman, Nature Energy **1**, ARTN 16137 (2016).

[160] M. Baba, K. Makita, H. Mizuno, H. Takato, T. Sugaya, and N. Yamada, Japanese Journal of Applied Physics **56**, ARTN 122302 (2017).

[161] S. Essig *et al.*, Nature Energy **2**, ARTN 17144 (2017).

[162] M. Steiner, R. France, J. Buencuerpo, J. Geisz, M. Nielsen, A. Pusch, W. Olavarria, M. Young, and N. Ekins-Daukes, Advanced Energy Materials **11**, ARTN 2002874 (2021).

[163] R. Cariou *et al.*, Nature Energy **3**, 326 (2018).

[164] S. Essig *et al.*, IEEE Journal of Photovoltaics **6**, 1012 (2016).

[165] C. Flotgen *et al.*, Semiconductor Wafer Bonding 13: Science, Technology, and Applications **64**, 103 (2014).

[166] M. Yamaguchi, K. Lee, K. Araki, and N. Kojima, Journal of Physics D-Applied Physics **51**, ARTN 133002 (2018).

[167] K. Tanabe, A. Morral, H. Atwater, D. Aiken, and M. Wanlass, Applied Physics Letters **89**, ARTN 102106 (2006).

[168] M. Levinshtein, *Handbook series on semiconductor parameters* (World Scientific, 1997), Vol. 1.

[169] R. Knechtli, R. Loo, and G. Kamath, Ieee Transactions on Electron Devices **31**, 577 (1984).

[170] B. Lee, R. Lentz, T. Burger, B. Roy-Layinde, J. Lim, R. Zhu, D. Fan, A. Lenert, and S. Forrest, ACS Energy Letters, 2388, 7 (2022).

[171] P. Baldasaro, J. Raynolds, G. Charache, D. DePoy, C. Ballinger, T. Donovan, and J. Borrego, Journal of Applied Physics **89**, 3319 (2001).

[172] B. Roy-Layinde, T. Burger, D. Fan, B. Lee, S. McSherry, S. Forrest, and A. Lenert, Solar Energy Materials and Solar Cells **236**, 111523 (2022).

[173] Y. Zhao and S. He, Microelectronic Engineering **98**, 19 (2012).

[174] A. Kirk, *Solar photovoltaic cells : photons to electricity* (Academic Press, London, [England], 2015).

[175] R. K. Ahrenkiel, R. Ellingson, S. Johnston, and M. Wanlass, Applied Physics Letters **72**, 3470 (1998).

[176] W. Metzger, M. Wanlass, R. Ellingson, R. Ahrenkiel, and J. Carapella, Applied Physics Letters **79**, 3272 (2001).

[177] D. L. Scharfetter and H. K. Gummel, IEEE Transactions on Electron Devices **ED16**, 64 (1969).

[178] J. G. Fossum and D. S. Lee, Solid-State Electronics **25**, 741 (1982).

[179] T. Asar, S. Ozcelik, and E. Ozbay, Journal of Applied Physics **115**, 104502 (2014).

[180] C. H. Henry, Journal of Applied Physics **51**, 4494 (1980).

[181] G. Quinchard *et al.*, Applied Optics **61**, 4079 (2022).

[182] I. T. Sorokina and K. L. Vodopyanov, (Springer Berlin Heidelberg : Imprint: Springer, Berlin, Heidelberg, 2003), p. 561 online resource (XVI).

[183] S. Baker-Finch, K. McIntosh, D. Yan, K. Fong, and T. Kho, Journal of Applied Physics **116**, 063106 (2014).

[184] C. Amy, H. Seyf, M. Steiner, D. Friedman, and A. Henry, Energy & Environmental Science **12**, 334 (2019).

[185] R. M. Swanson, in *1980 International Electron Devices Meeting* (IEEE, 1980), pp. 186.

[186] B. Wernsman *et al.*, Ieee Transactions on Electron Devices **51**, 512 (2004).

[187] L. Fraas, J. Samaras, H. Huang, L. Minkin, J. Avery, W. Daniels, and S. Hui, in *Proceedings of 17th European PV Solar Energy Conference, Munich, Germany*2001).

[188] J. Fernandez, F. Dimroth, E. Oliva, M. Hermle, A. Bett, C. Algora, and C. V, Thermophotovoltaic Generation of Electricity **890**, 190 (2007).

[189] R. R. Siergiej, S. Sinharoy, T. Valko, R. J. Wehrer, B. Wernsman, S. D. Link, R. W. Schultz, and R. L. Messham, in *AIP Conference Proceedings* (American Institute of Physics, 2004), pp. 480.

[190] R. Siergiej *et al.*, in *AIP Conference Proceedings* (American Institute of Physics, 2003), pp. 414.

[191] D. Woolf *et al.*, Optica **5**, 213 (2018).

[192] Z. Yu, K. Fisher, B. Wheelwright, R. Angel, and Z. Holman, IEEE Journal of Photovoltaics **5**, 1791 (2015).

[193] D. Bobela, L. Gedvilas, M. Woodhouse, K. Horowitz, and P. Basore, Progress in Photovoltaics **25**, 41 (2017).

[194] G. F. Furtado, V. V. de Almeida Camargo, D. Vasileska, and G. I. Wirth, Journal of Integrated Circuits and Systems **16**, 1 (2021).

[195] W. Bolton, *Control systems* (Newnes, 2002).

[196] R. K. Ahrenkiel and S. P. Ahrenkiel, *Theory and Methods of Photovoltaic Material Characterization: Optical and Electrical Measurement Techniques* (World Scientific, 2019), Vol. 13.

[197] J. Lim, B. Oh, W. Lee, K. Lee, H. Na, B. Kim, D. Seo, J. Han, and J. Hwang, Applied Physics Letters **95**, ARTN 123503 (2009).

[198] G. Branch and T. Mihran, IRE Transactions on Electron Devices **2**, 3 (1955).